RICE UNIVERSITY

A Resistor Network Model for the Determination of Electrical and Thermal Properties of Nanocomposites

by

Clayton Higginson, 2nd Lt USAF

A THESIS SUBMITTED
IN PARTIAL FULFILLMENT OF THE
REQUIREMENTS FOR THE DEGREE

Master of Science

APPROVED, THESIS COMMITTEE

Dr. Pol D. Spanos, Chair
Lewis B. Ryon Chair Professor in
Mechanical Engineering

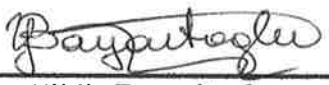

Dr. Yildiz Bayazitoglu
Harry S. Cameron Chair Professor in
Mechanical Engineering

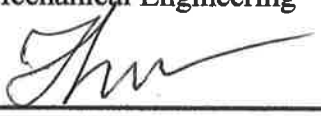

Dr. Ilinca Stanciulescu
Assistant Professor of Civil Engineering

HOUSTON, TEXAS
April 2017

The views expressed in this article are those of the author and do not reflect the official policy or position of the United States Air Force, Department of Defense, or the U.S. Government.

Abstract

A Resistor Network Model for the Determination of Electrical and Thermal Properties of Nanocomposites

by

Clayton Higginson

Superior electrical, thermal, and mechanical properties of carbon nanotubes have made them popular candidates for use as fillers in polymer nanocomposites. This thesis presents a numerical model developed to determine the electrical and heat transport properties of these materials via percolation theory. Realistic nanocomposite representative volume elements are generated in three-dimensional space according to user-defined input parameters. A spanning network algorithm is used to search for connections between nanotubes. Interconnected nanotubes are then converted into equivalent resistor networks. The resistor network is then examined using finite element analysis through Kirchoff's current law for electrical transport, and Fourier's law for thermal transport. Monte Carlo simulations eliminate statistical variation at each volume fraction of nanotube filler. Several boundary treatment methods are examined to determine which is the most computationally efficient. The model is validated through comparison to experimental data reported in the literature. The presented model is unique in that it can predict both the electrical and thermal conductivity of carbon nanotube based polymer nanocomposites.

Acknowledgments

I have many people I would like to thank for their contributions and support during my time at Rice University. First, I would like express my gratitude for my advisor, Dr. Pol Spanos. He helped get me into Rice in the first place and has provided invaluable guidance throughout my time here. I am honored to join his “squadron” of Air Force officers.

I would also like to thank Dr. Yildiz Bayazitoglu and Dr. Ilinca Stanciulescu for dedicating their time to serving on my thesis committee. I must recognize the previous work done by Bradley Ward, Jacob Decklever, Paul Elsbernd, Trevor Koenck, and Dr. Milton Esteva for their influence on my research. My work would certainly not have been possible without the foundation laid by them. Further, I would like to thank Dr. Eleazar Marquez for his mentorship and friendship during my time here. He was able to provide guidance in several areas, not the least of which was the state of the Cowboys football team.

Most deserving of acknowledgement is my family. I am so lucky to have met my fiancé, Brittany, during my time in Houston and cannot wait to spend the rest of my life with her. Further, a heartfelt thank you to my parents for all the support and love you have given me through my life to date. I would never have had these opportunities if it were not for you.

Contents

List of Figures

List of Tables

Chapter 1

Introduction

1.1 Motivation

Ever since their discovery in 1991, carbon nanotubes (CNTs) have been researched extensively due to their remarkable mechanical, thermal, and electrical properties [1]. CNTs are molecular-thick cylinders of carbon atoms. CNTs can be classified as either single-walled nanotubes (SWNTs) or multi-walled nanotubes (MWNTs). The elastic moduli of SWNTs are on the order of 1 TPa, while having fracture strains of 10-30% [2–5]. This indicates that SWNTs have elastic moduli that are three times those of carbon fibers and five times that of steel, at one-sixth of the weight [6]. The thermal conductivity has been reported to be in the range of 3,000 – 6,000 W/mK at room temperature, approximately three times the thermal conductivity of diamond and four magnitudes higher than most polymers [7], [8]. The electrical conductivity of SWNTs is also excellent, on the order of 10^4-10^7 S/m [9], [10]. They have also been reported to be able to sustain current densities above 10^9 A/cm at high voltages for extended periods without suffering any damage [11]. This gives CNTs a current capacity that is three magnitudes higher than that of copper wire and two magnitudes higher than that of typical superconductors [12], [13].

The extremely small size of CNTs makes it difficult to fully utilize their outstanding properties. To alleviate this, CNTs can be combined with polymers to create polymer nanocomposites [14]. A nanocomposite is a heterogeneous combination of two or more materials where one of the constituents has dimensions on the nanoscale. The result is a material that exploits the properties of the individual constituents. The aforementioned excellent properties of CNTs make them great candidates for use in composite mixtures [6]. CNT-filled nanocomposites have been studied for use in a variety of applications, such as structural reinforcement, thermal management, and electrical conduction. Specific applications include stretchable electronics, field-emission devices, solar cells, health-monitoring sensors, and lightning-strike protection for aircraft structures [15]–[21]. The addition of a small volume fraction of nanotubes to an insulating polymer can create a conductive material due to the extremely high aspect ratio and high electrical and thermal conductivities of CNTs. These materials have received considerable attention for use in the electronics, automotive, and aerospace industries to dissipate heat and prevent the buildup of static charge [22]. While good results have been achieved with improving the electrical properties of CNT based polymer nanocomposites, the improvement of their heat transport properties has been much less substantial [23].

The potential of nanocomposite materials has motivated extensive research in the area, both experimental and simulation-based. There is a large variation of reported electrical and thermal transport properties of nanocomposite materials [23], [24]. There is a need for accurate models which can predict the electrical and thermal properties of CNT/polymer nanocomposites. The sheer number of parameters inherent to the problem,

including CNT size, chirality, volume fraction and several others make accurate analytical and numerical modeling of the problem necessary to circumvent the need for costly experiments. That is the motivation for the model presented in this thesis.

1.2 Percolation and Conduction

Carbon nanotubes are composed of molecular thick sheets of carbon, also known as graphene, rolled into cylinders [25]. As mentioned previously, they can consist of a single layer as SWNTs or contain multiple layers to form MWNTs. There are also multiple different geometrical structures that SWNTs can form, as depicted in Figure 2. Depending on the geometric structure of the nanotubes, they can be classified as either metallic or semiconducting [26].

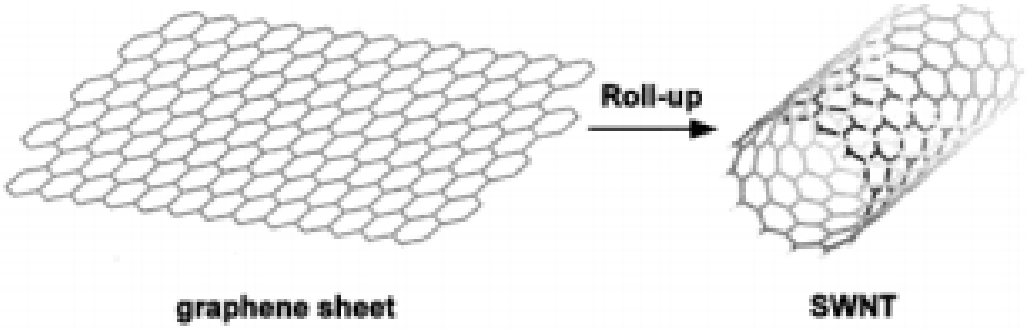

Figure 1. SWNTs consist of a single sheet of rolled-up graphene, from Odom et al. [27].

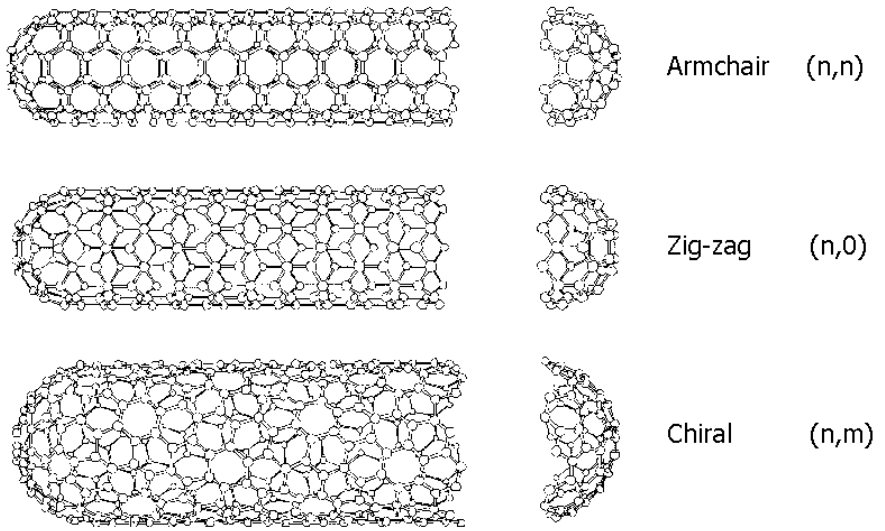

Figure 2. Various SWNT geometric structures [28].

The formation of a spanning network of nanotubes is the driving factor for electrical conductance in nanocomposites. Due to the structure of CNTs, they can be considered as one-dimensional conductors with low resistance along the length of the nanotube and high out-of-plane resistance [29]. A connected network of CNTs must form so that electricity can effectively be conducted through the material. The formation of this network is known as percolation. If the CNTs are not well dispersed or there are not enough nanotubes present to form a connected network then percolation will not occur. The volume fraction of CNTs where a nanocomposite transitions from an insulator into a conductor due to percolation is known as the percolation threshold [30]. The extremely high aspect ratio of CNTs allows them to create percolated nanocomposites at low volume fractions of CNT fillers [31]. Few CNTs in a percolated network will actually carry current. The conducting path which composes the path of least resistance will carry

the majority of the current. This is known as the backbone of the nanocomposite [32]. Identification of this backbone is one of the outputs of the proposed model.

There is a significant difference between the electrical conductivity of CNTs and that of the polymer matrix they are dispersed within. The electrical conductivity of polymers has been reported in the range of 10^{-16} – 10^{-12} S/m, approximately 20 orders of magnitude lower than that of CNTs which are on the order of 10^{4} – 10^{7} S/m [33]. Due to this large disparity, the polymer matrix is considered an insulating material and all current is assumed to be carried through CNTs within the matrix. The behavior is characterized by a large jump in conductivity once percolation occurs, followed by a steady increase in conductivity as the volume fraction of CNT filler increases as shown in the experimental data by Kim et al. [30].

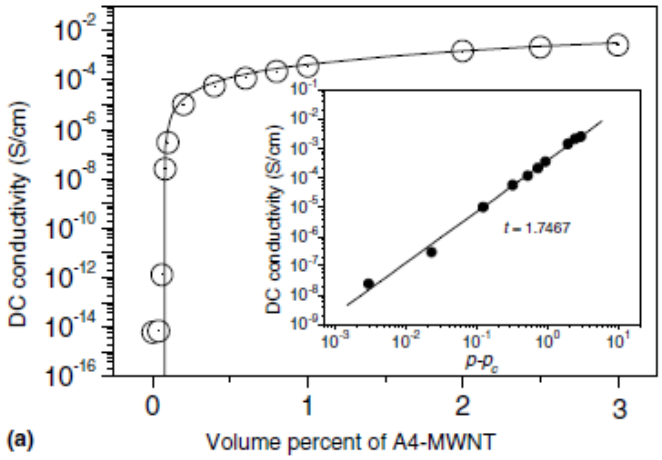

Figure 3. Experimental data of nanocomposite electrical conductivity increasing as volume fraction of MWNTs increases, from Kim et al. [30].

The increase in thermal conductivity from the addition of CNTs is much more disappointing in comparison to the electrical case [22], [23]. The thermal conductivity of polymers is typically around 0.3 W/mK, only 3-4 magnitudes lower than that of SWNTs

which have been reported at 6000 W/mK [8]. Since the ratio of conductivities is relatively small between the two materials, percolation behavior is much less evident as shown in the experimental data from Hong and Tai [23] in Figure 4.

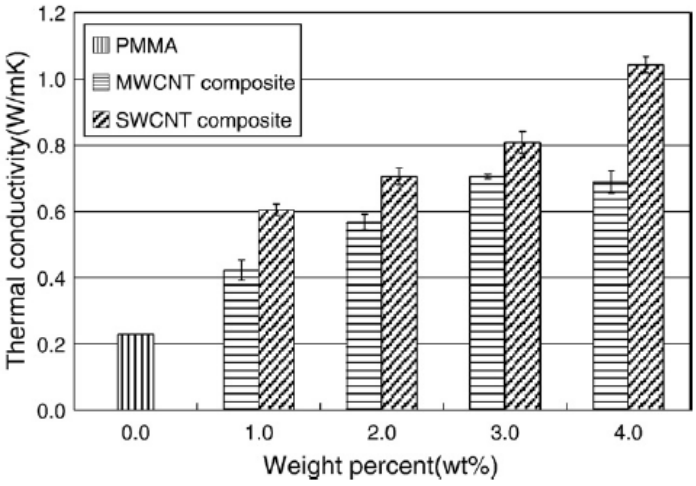

Figure 4. Experimental data of nanocomposite thermal conductivity increasing as volume fraction of both SWNTs and MWNTs increase, from Hong and Tai [23].

Instead of the conductivity jumping ten orders of magnitude as in Figure 3, there is only a modest increase in thermal conductivity as more nanotubes are added to the composite. It is a matter of debate to whether or not thermal transport in nanocomposites can be described through percolation theory [34], [35]. However, efforts to describe the thermal conductivity using effective-medium methods have been found to be inadequate [36]. The existence of a high interfacial resistance between CNTs and the polymer matrix limits heat transfer between the two, effectively creating an insulating boundary between nanotubes and the polymer matrix [37]. Therefore, it can be argued that percolation theory is perfectly suited for modeling thermal transport since any increase in the thermal properties would necessarily have to come through a connected CNT network.

1.3 Previous Models

Percolation and conduction in composite materials has been studied for several decades, with the focus mainly on electrical properties. In 1971, Last and Thouless [38] used a hole-punching experiment with electrically conductive paper to show that conductivity and percolation probability are described by different mechanisms due to the formation of dead ends and constrictions in the network. Kirkpatrick [39], [40] followed this up by developing a power law for percolation theory and using resistor networks in conjunction with Kirchoff's current law (KCL) to calculate the conductivity of composite materials, findings that have influenced the field ever since. Pike and Seager [41] studied percolation in random two-dimensional (2D) stick models using Monte Carlo simulations. Balberg et al. [42] extended this to study percolation in randomly oriented three-dimensional (3D) sticks using an excluded volume approach. It was reported here that larger aspect ratio fillers correspond to a lower percolation threshold. These findings were verified and expanded on in Celzard et al. [43].

Some models have used homogenization and micromechanics to model CNT based nanocomposites. Deng and Zheng [33] used micromechanics equations to predict the electrical conductivity and percolation threshold for wavy CNTs. McLachlan et al. [44] developed complex power-law equations fit to experimental data. Seidel and Lagoudas [45] created a micromechanics model based on composite cylinders and used Mori-Tanaka homogenization methods to calculate the properties of SWNT and MWNT composites. These models use analytical methods to derive their results, but it has been shown that numerical methods may be best suited for capturing the stochastic nature of composite conductivity [46], [47].

Several numerical models have been created in attempts to accurately represent the electrical behavior of nanocomposites. Li and Chou [32], [48]–[50] and Li et al. [51], [52] have reported many findings for 2D representative volume element (RVE) nanocomposite models that have taken into account factors such as waviness, electron tunneling, and alignment. An RVE model attempts to calculate the macroscopic properties of a material by calculating the properties of a sufficiently large representation of the material. Behnam and Ural [53] used KCL and Monte Carlo simulations to calculate the properties of stacked 2D layers of CNT nanocomposites and tested the effects of CNT alignment and CNT-CNT contact resistance. These models have produced great findings on the effect of changing CNT parameters on nanocomposite conductivity, but have been restricted to 2D film material characterization.

Three-dimensional (3D) RVE models have been developed that more closely represent the true nanocomposite geometry. Dalmas et al. [54] used 3D RVEs of wavy, randomly oriented nanotubes. Ma and Gao [55] used their model to investigate the relation between aspect ratio and curliness on percolation threshold. Hu et al. [56] utilized a 3D model with soft-core CNTs that included periodic boundary conditions. The use of 3D models requires a much higher computation time due to the increased amounts of CNTs that must be modeled [56]. RVE dimensions need to be kept large enough so that an accurate estimation of conductivity can be obtained; if they are too small then conductivity tends to be over-predicted. However, increasing the RVE size increases the computation time since larger networks will have to be evaluated and computation time has been found to be proportional to the number of contacts cubed [57]. Several authors have attempted to address these issues. Bao et al. [58] proposed a model which used

periodic boundaries, allows for current to flow through insulating boundaries, and requires that current can only flow through CNTs that are present at both conducting boundaries. The authors claimed that by making these modifications, a much smaller cubic RVE volume could be used and still achieve accurate results, reducing the required computation time. Fang et al. [59] produced a model which did not feature periodic boundary conditions and instead created a model that requires the computation of several RVEs that are algebraically combined to calculate the effective conductivity. This formulation can also be used with smaller RVE volumes and in turn has a lower computation cost.

All the models listed focus only on the electrical properties of nanocomposites, even though it has been shown that percolation theory can also be used to describe thermal transport in these materials [34], [60]–[62]. Each differs in how they treat details such as CNT geometry, contact resistance, fiber resistance, and morphology. Certain models have incorporated waviness into their nanotubes while others consider them as straight rods. Others only account for contact resistance between nanotubes and neglect the resistance of the actual nanotubes or vice-versa. The models that do account for contact resistance often do so in different manners. The large discrepancy in modeling efforts calls for an adaptable model where various input parameters can be changed to effectively model the desired nanocomposite material.

Rice University has been at the forefront of nanomaterials research since the discovery of buckminsterfullerene in 1985. Over the past decade this has extended into simulation-based nanocomposite modeling as well as molecular dynamics modeling [63]–[72]. The current modeling efforts are inspired by the works in [73], [74] where the

embedded fiber finite element model (EFFEM) was developed which predicted the elastic and thermal properties of CNT nanocomposites using 2D RVEs. This method was further elaborated on to include the effects of non-linearity and to account for piezoelectric properties [75], [76]. Bradley Ward [77] modified the model so that the electrical properties of CNT nanocomposites by creating a spanning-network algorithm and using a resistor network model to solve for the electrical conductivity. However, this model utilized a 2D RVE with an assigned thickness which has been shown to be insufficient for characterizing nanocomposite materials [56]. The purpose of this work is to expand on this model and create a 3D percolation model that is capable of calculating both the electrical and thermal properties of CNT nanocomposites. Methods described in the literature will be used to lower the overall computation cost incurred by using 3D RVEs. This will yield a comprehensive model that will push the boundaries on predictive CNT/polymer nanocomposite electrical and thermal property modeling.

1.4 Outline

This thesis presents a 3D model aimed at providing accurate, computationally efficient estimates of nanocomposite electrical and thermal conductivity. To this aim, Chapter 2 details the process of creating both 2D and 3D RVEs of CNT nanocomposites. The CNT length distribution is presented in this chapter as well as how the parameters of waviness and diameter are handled. Both periodic boundary conditions and non-periodic boundary conditions will be used in this work. Finally, the spanning-network algorithm developed in [77] is modified for use in three dimensions.

Chapter 3 describes the resistor network model that takes the spanning network from Chapter 2 and converts it into a finite element problem using KCL for the electrical case and Fourier's law for the thermal case. The values for electrical and thermal contact resistances used in the model are discussed. Solving the finite element equations gives the voltage and temperature at every degree of freedom in the network for the electrical and thermal cases respectively. Post-processing is necessary to determine the overall conductance and conductivity.

Chapter 4 lists various methods of treating the RVE boundaries so that accurate results can be obtained. If transport through the boundaries is not considered, then the dimensions must be made large enough so that accurate results are obtained. If they are directly accounted for, then smaller RVE dimension sizes can be used to reduce computation time. The Monte Carlo simulation process for generating multiple RVEs at each volume fraction of filler is also explained.

Chapter 5 gives the numerical results, starting with a comparison of the 2D and 3D models. The various boundary methods are compared to determine which one delivers the best combination of accuracy and low computation cost. Results from the electrical and thermal modeling are compared against experimental data. A power law relation is fit to the data so that the conductivity can be found at any volume fraction above the percolation threshold. Chapter 6 consists of concluding remarks drawn based on the conducted research.

Chapter 2

The Representative Volume Element

2.1 Synopsis

The first two steps of the model considered are generating the RVE geometry, and determining if a spanning CNT network exists through the RVE. A Weibull distribution is used to determine the length and maximum waviness of each CNT. Both 2D and 3D RVEs are generated. Initially, the RVE consists of only the insulating polymer matrix. CNT fibers are then randomly added to the RVE until the desired volume fraction of fillers is reached. There are two different methods for handling fibers that cross RVE boundaries, through the use of periodic boundary conditions and non-periodic boundary conditions. After all the CNTs have been added, extra nodes are created within each CNT for use in the spanning network algorithm. This algorithm starts with CNTs at the top of the RVE, corresponding to the +Y boundary for 2D RVEs and +Z face for 3D RVEs, and searches for additional connections until no new connections are made. Percolation occurs if the network extends from the top of the RVE to the bottom, corresponding to the –Y and –Z face for 2D and 3D RVEs respectively.

2.2 CNT Parameters

First, the parameters for CNT generation must be determined. The parameters that are of most concern in this model are length, waviness, and diameter. The initial location and orientation of each CNT are isotropic and random. Previous models [73], [74] provide the basis for the stochastic generation of CNTs into the polymer matrix.

The length of individual CNTs varies over a wide range and is dependent on manufacturing methods as well as chemical functionalization that may be applied. It has been reported that CNT lengths tend to follow a Weibull distribution [78]. The probability density function (PDF) and cumulative density function (CDF) of a Weibull distribution are described by the equations

$$f(x;\lambda,k) = \begin{cases} \frac{k}{\lambda}\left(\frac{x}{\lambda}\right)^{k-1} e^{-\left(\frac{x}{\lambda}\right)^{k}} & x \geq 0 \\ 0 & x < 0 \end{cases}, \quad \textbf{(1)}$$

$$F(x;\lambda,k) = 1 - e^{-\left(\frac{x}{\lambda}\right)^{k}}, \quad \textbf{(2)}$$

where λ and k are the scale and shape parameters, respectively; x is a realization from the corresponding Weibull distribution. Solving for x in the CDF yields

$$x = \lambda[-ln(1-u)]^{\frac{1}{k}}, \quad \textbf{(3)}$$

where u is a uniform random variable. The inverse transform method can now be used to generate uniform random variables and transform them into realizations from the Weibull distribution. The scale and shape parameters differ based on CNT type. For SWNTs, the distribution can be well described with $\lambda = 5.6 \times 10^{-7}$, and $k = 2.4$ [78]. A histogram

of 10,000 realizations of this distribution is shown in Figure 5. The average CNT length from this distribution is approximately 5 x 10^{-7} m or 500 nm.

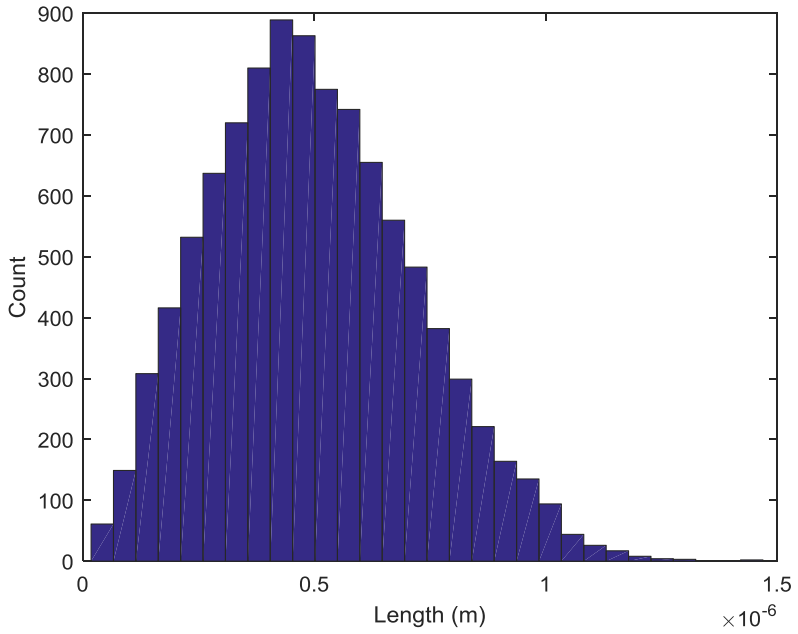

Figure 5. Histogram of 10,000 realizations of CNT length Weibull distribution.

The next parameter to determine is the nanotube waviness. Due to their low bending stiffness, matrix-embedded CNTs are curved rather than straight. Observation of these fibers shows that longer fibers tend to be wavier than shorter ones [74]. This waviness is accounted for by breaking each CNT into a series of 10 line segments and varying the angle between each segment. The maximum angle of variation for each CNT is determined by the following equation

$$\theta_{max} = \frac{\pi}{2000\ nm} \times CNT\ length, \qquad \textbf{(4)}$$

where θ_{max} is the maximum angle of variation in radians. This relation is used so that the average maximum angle of deviation equals $\pi/4$ radians. From Equation (4) it can be

seen that longer CNTs will tend to be wavier. The distribution of θ_{max} as a result of the previously defined Weibull length distribution is shown in Figure 6. This is also a Weibull distribution because it is simply the length distribution multiplied by a constant.

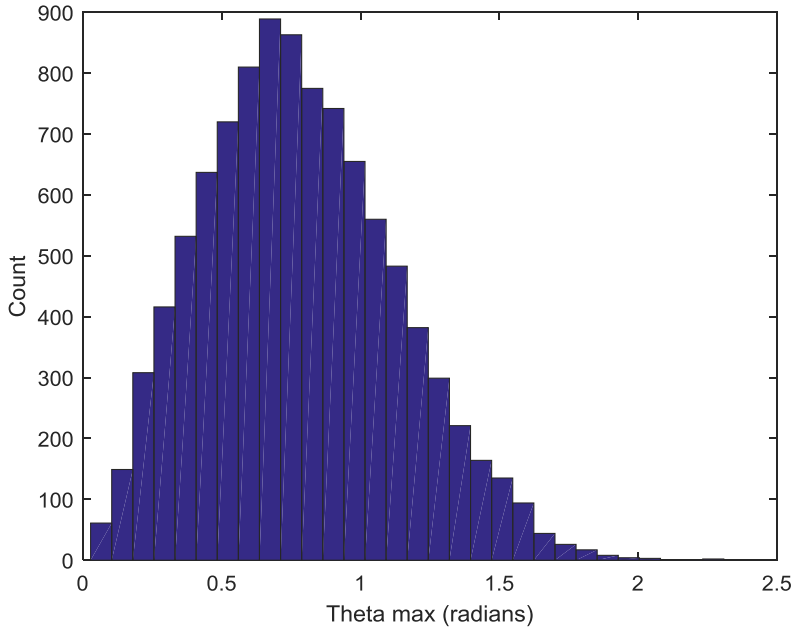

Figure 6. Histogram of 10,000 realizations of CNT maximum angle of variance Weibull distribution.

The final parameter to determine is CNT diameter. Previous models developed at Rice University [73], [75]–[77] have used a lognormal distribution for CNT diameter based on experimental data from Ziegler et al. [79]. However, in the interest of computational efficiency the diameter will be set to a constant value of 5 nm in the present work, well within the range of reported SWNT diameters [78], [80]. This gives each CNT an average aspect ratio of 100 which corresponds well with other nanocomposite models [47], [56].

2.3 Geometry Generation

The next step is to generate individual CNT fibers within the RVE. The method of fiber generation for both 2D and 3D RVEs will be discussed here. As stated earlier, each CNT is composed of 10 connected line segments. Though CNTs tend to agglomerate in nanocomposite materials, advances in functionalization have created acceptable levels of distribution and dispersion [81], [82]. Therefore, this model will assume perfect distribution and dispersion so that the starting point of each CNT is a uniform random variable within the RVE boundaries.

2D RVEs consist of a square within the X-Y plane with an assigned thickness, much like a plane stress problem. The first node (x_0, y_0) is randomly generated within the RVE. The second node is also randomly generated but adjusted to be exactly a distance l, the segment length, away from the first node. This results in random placement and initial orientation. The positions of the following nodes are determined recursively from the expression

$$\begin{bmatrix} x_i \\ y_i \end{bmatrix} = \begin{bmatrix} x_{i-1} \\ y_{i-1} \end{bmatrix} + \begin{bmatrix} \cos\varphi & -\sin\varphi \\ \sin\varphi & \cos\varphi \end{bmatrix} \begin{bmatrix} l\cos\theta \\ l\sin\theta \end{bmatrix}, \quad \textbf{(5)}$$

where φ represents the inclination of the previous segment with respect to the global coordinate system in the X-Y plane and θ is the angle between the current and previous segment. To determine θ, a random variable is chosen from the uniform distribution

$$\theta = \theta_{max} \times u - \frac{\theta_{max}}{2}. \quad \textbf{(6)}$$

This is repeated until all ten segments of the CNT have been generated, at which point a new CNT is created until the desired volume fraction of CNTs has been reached. The

CNTs are modeled as soft-core cylinders, meaning they are generated independently and allowed to penetrate through each other. Previous models have shown that when using high-aspect ratio fillers the soft-core assumption can be used with minimal error [36].

3D RVEs are created in the same manner except that there is a more complex expression since CNTs occupy space in three dimensions. Once again, the first node (x_0, y_0, z_0) is randomly generated from within the RVE dimensions. The following nodes are recursively generated as follows

$$\begin{bmatrix} x_i \\ y_i \\ z_i \end{bmatrix} = \begin{bmatrix} x_{i-1} \\ y_{i-1} \\ z_{i-1} \end{bmatrix} + l \begin{bmatrix} \cos\Theta_{i-1} \\ \sin\Theta_{i-1}\cos\Phi_{i-1} \\ \sin\Theta_{i-1}\sin\Phi_{i-1} \end{bmatrix}, \quad \textbf{(7)}$$

where Θ and Φ are the respective polar and azimuthal angles in the global coordinate system. The angles for the first segment are randomly generated through

$$\cos\Theta_0 = 2 \times u - 1, \quad \text{and} \quad \Phi_0 = 2\pi \times u, \quad \textbf{(8)}$$

where u again is a uniform random variable. For the following global azimuthal and polar angles, the local angles must first be found. These angles are found by

$$\cos\theta_i = \cos\theta_{max} + u \times (1 - \cos\theta_{max}), \quad \text{and} \quad \varphi_i = 2\pi \times u, \quad \textbf{(9)}$$

where θ and φ are the local polar and azimuthal angles. These can be transferred to the global coordinate system by two successive rotations along the Z- and X-axes, such that

$$R_z(\Theta_{i-1}) = \begin{bmatrix} \cos\Theta_{i-1} & -\sin\Theta_{i-1} & 0 \\ \sin\Theta_{i-1} & \cos\Theta_{i-1} & 0 \\ 0 & 0 & 1 \end{bmatrix}, \quad \textbf{(10)}$$

$$R_x(\Theta_{i-1}) = \begin{bmatrix} 1 & 0 & 0 \\ 0 & \cos\Phi_{i-1} & -\sin\Phi_{i-1} \\ 0 & \sin\Phi_{i-1} & \cos\Phi_{i-1} \end{bmatrix},$$

and the transformation from local to global coordinates is,

$$\begin{bmatrix} \cos\Theta_i \\ \sin\Theta_i \cos\Phi_i \\ \sin\Theta_i \sin\Phi_i \end{bmatrix} = R_x(\Theta_{i-1}) R_z(\Theta_{i-1}) \begin{bmatrix} \cos\theta_i \\ \sin\theta_i \cos\varphi_i \\ \sin\theta_i \sin\varphi_i \end{bmatrix}, \quad \textbf{(11)}$$

which can be applied in Equation (7) to find the location of the next node. As in the 2D case, each CNT is generated independently as a soft-core cylinder and allowed to interpenetrate through other generated CNTs.

There are two different ways to handle the case where a generated node lies outside of the 2D or 3D RVE boundaries, through the use of periodic or non-periodic boundary conditions. Periodic boundary conditions take the CNT segment located outside the boundary and relocate it to the opposite boundary. This is also known as the "cut-and-relocate" approach [59]. Periodic boundary conditions ensure geometric continuity by creating a realistic amount of CNTs at each of the boundaries [57]. This is depicted in Figure 7 for the 2D case.

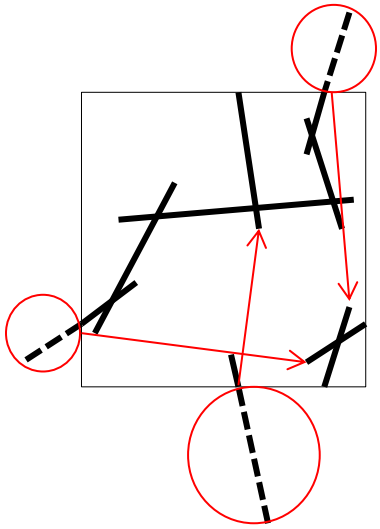

Figure 7. Depiction of periodic boundary conditions in a 2D RVE. CNT segments that extend outside the RVE boundaries are relocated to the opposite boundary, maintaining their other coordinate values. For simplicity, only straight CNTs have been shown.

Periodic boundary conditions have been used extensively in the literature [47], [56]–[58], [77]. However, it has been claimed that the cut-and-relocate approach creates unnecessary bias on the amount and location of CNTs located at the boundaries [59]. A simple solution is suggested here to generate RVEs with non-periodic boundary conditions. This method generates CNTs in a larger area or volume extending past the boundaries of the 2D or 3D RVE. After all CNTs have been generated, the desired RVE dimensions are "cut" from the total generated area or volume. Fibers that cross the RVE boundaries are partitioned but not relocated to the opposite side. A depiction of this for the 2D case is shown in Figure 8.

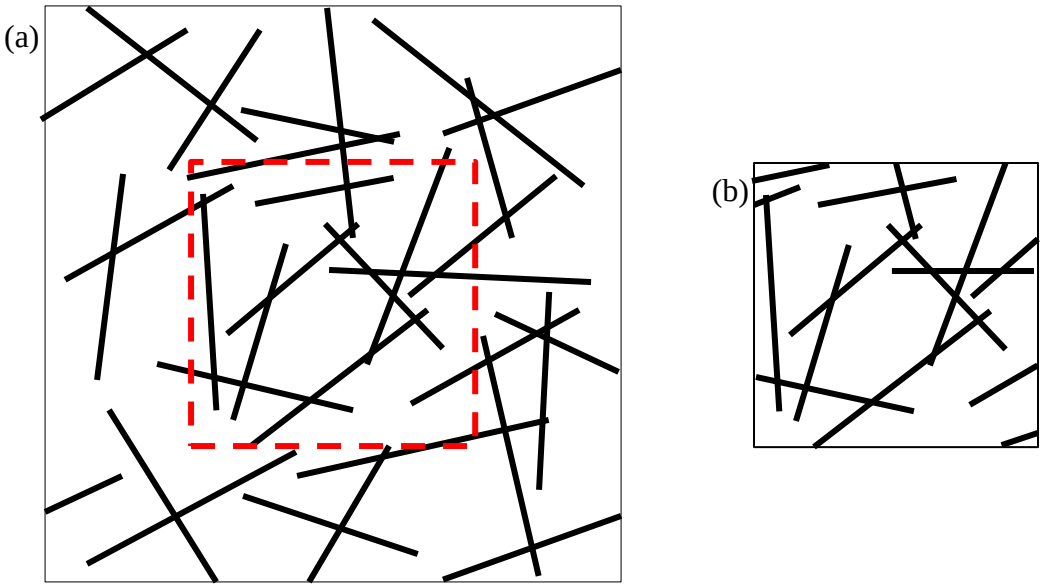

Figure 8. Depiction of non-periodic boundary conditions in a 2D RVE. (a) CNTs are generated in a large area surrounding red border of the desired RVE. (b) The desired RVE is cut out and fibers lying across its boundary are partitioned.

This method still ensures a realistic amount of CNTs are located at each boundary but it does not generate bias in in the way that periodic boundary conditions do. One thing to note about this method is that since CNTs are stochastically generated within a larger area, the volume fraction of CNTs within the cut-out RVE may be more or less than the specified volume fraction. This actually corresponds well to a real-world nanocomposite where CNT distribution may vary throughout the material.

The final geometrical parameter to take into account is the actual size of the RVE used. The larger the dimensions of the RVE, the more accurate the results will be since it creates a more realistic depiction of the macroscopic material. Typically, having too small of an RVE will result in overestimating the conductance [56]. Larger RVE sizes incur larger computation times as it has been shown that computation time is proportional

to the number of contacts cubed [57]. This is a minor issue for 2D RVEs which have on the order of 10^2 contacts, but becomes quite problematic for 3D RVEs which can have on the order of 10^5 contacts. The square 2D RVE models of Li et al. [51], Li and Chou [50], and Jack et al. [57] had RVE dimensions of at least ten times the average CNT length. Hu et al. [56] created cubic 3D RVEs with dimensions of five times the CNT length. The dimension of the RVE necessary to obtain accurate results using different solution methods will be determined in Chapter 5.

2.4 Spanning Network Algorithm

The next step after generating the RVE geometry is to determine whether there is a spanning CNT network across the microstructure. The spanning network algorithm determines whether the structure has percolated [77]. This is by far the most computationally expensive portion of the model. Only one direction will be checked for percolation, the Y-direction for 2D RVEs and Z-direction for 3D RVEs. This will be referred to as the conducting direction. The other directions, the X-direction for 2D RVEs and X- and Y-directions for 3D RVEs, will be referred to as the non-conducting directions. The conducting direction corresponds to the vertical direction when viewed from the output figures, as can be seen in Figures 9 and 10.

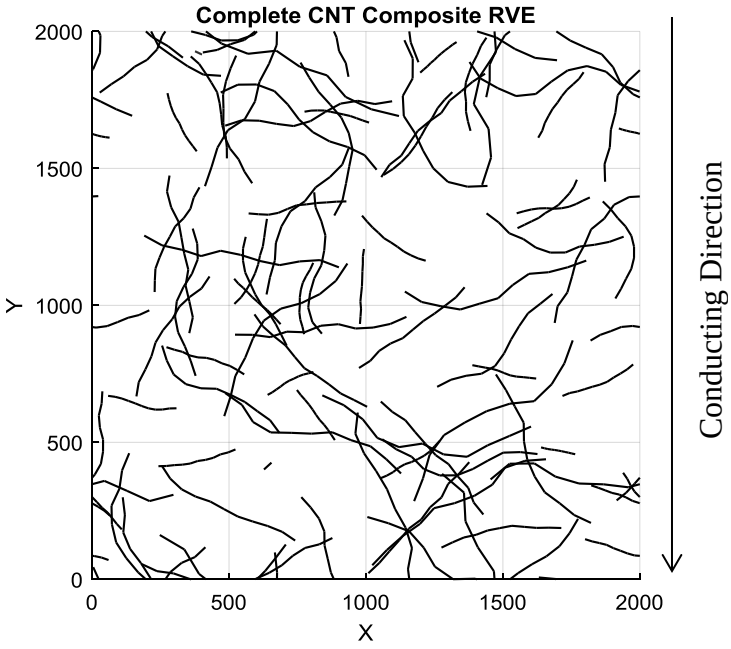

Figure 9. Generated 2D RVE with periodic boundary conditions, 2% volume fraction of CNT fillers.

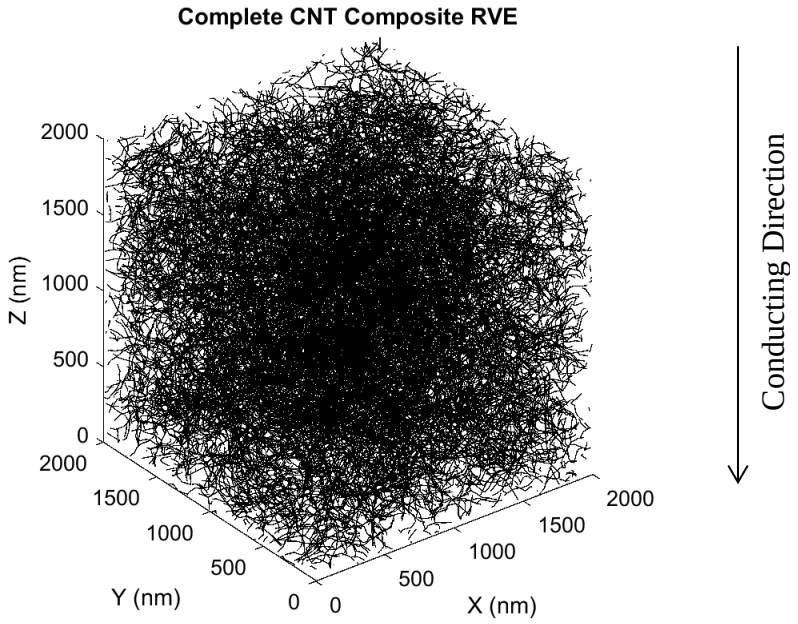

Figure 10. Generated 3D RVE with periodic boundary conditions, 0.6% volume fraction of CNT fillers.

A complete spanning network across the RVE allows for the transport of electricity and heat through CNTs in the network. For this model, the contact between CNTs and the polymer matrix is considered perfectly insulating so without percolation there is no electrical or thermal transport via CNTs.

The first step in the algorithm is to establish the bonding criterion. Bonding criterion determines whether any pair of points is connected. If multiple bonds belong to the same chain, they form a connected network. Pike and Seager [41] studied two categories of bond criteria: overlapping figure and inclusive figure. Overlapping figure specifies that two sites are connected if their individual searching regions intersect. Inclusive figure states that two sites are connected if each site falls within the searching region of the other. Examples of this are shown in Figure 11. Keep in mind that searching regions are present for each point on the inclusive figure side even though only one is shown.

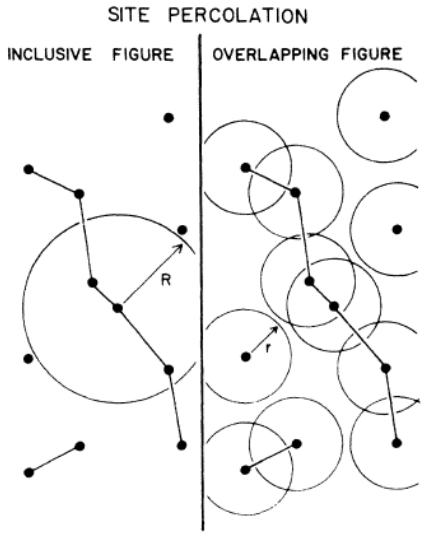

Figure 11. Examples of both inclusive figure and overlapping figure bonding criterion, from Pike and Seager [41].

The inclusive figure method was found to be more accurate and well-suited for random site percolation problems. Therefore, this method is implemented in the present work. The nodes within each CNT in the network will be checked against other CNT fibers to determine whether or not a connection exists between them. Shenogin et al. [29] used their molecular dynamics model to show that that even one molecule of polymer between two CNTs was effectively insulating, so only CNTs which are directly touching or interpenetrating will be considered to be in contact. It has been determined that square searching regions yielded very similar results in comparison to circular regions, so square searching regions of 5 nm x 5 nm will be used here for each 2D RVE node and cubic searching regions of 5 nm x 5nm x 5nm will be used for 3D RVE nodes based on the chosen CNT diameter of 5 nm [41]. If the node of another CNT is within this range, a connection is made between the two fibers.

Additional nodes must be added to each segment to be used as searching points. Initially, there are only nodes at the endpoint of each segment. Extra nodes must be added at regular intervals along the fiber so that connections can be made along the entire length of the fiber. The number of new nodes to be added can be found through the inequality

$$n \geq \frac{l_{seg}}{D} - 1, \tag{12}$$

where n is the number of new segments to add, l_{seg} is the length of the current segment, and D is the CNT diameter. Adding these nodes along the length of the fiber ensures that no gaps exist and all possible connections are established.

To expedite the searching process, the RVE is divided into a regular grid of searching bins. These bins are rectangular for 2D RVEs and rectangular prisms for 3D

RVEs. The bins that each CNT resides in are recorded in an effort to accelerate the searching process. The checker fiber will only check for connections with fibers that also reside in that bin. This prevents the need for searching for connections with fibers on the other side of the RVE that will clearly not form connections with the checker fiber. This greatly reduces the computational cost of the program. The fibers are sorted by checking the location of each of its nodes. A CNT can be located in more than one bin if it transverses bin boundaries. Previous modeling efforts have shown that 10 bin divisions along each dimension has been found to provide a good balance between decreasing computation time and ensuring that no connections are missed [77]. This results in a total of 100 total bins in 2D RVEs and 1,000 bins in 3D RVEs.

With the processes of determining the searching region, creating extra nodes, and sorting fibers into bins complete, the spanning network algorithm can be utilized to search for a connected network of CNTs. Fibers touching the top boundary of the RVE are automatically added to the network initially. These fibers are checked one at a time against other fibers in each of their bins. If contact is established, the contacted fiber number is recorded. After each of these fibers has been checked, a new iteration begins and fibers that were found in the previous iteration are checked for connections. This continues until no new fibers are added to the network. If at least one fiber in the network touches the bottom boundary, then percolation has been achieved. Figures 12 and 13 show the progression of the spanning network algorithm for 2D and 3D RVEs respectively. For reference, these are the same RVEs that were generated for Figures 9 and 10.

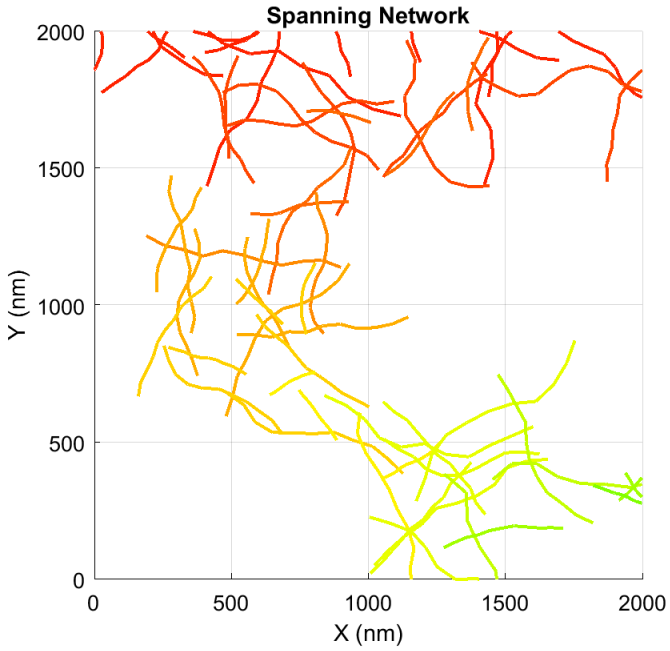

Figure 12. 2D RVE connected network. Dark red corresponds to CNTs first added to the network and lighter colors correspond to fibers added later. Percolation occurs in this RVE.

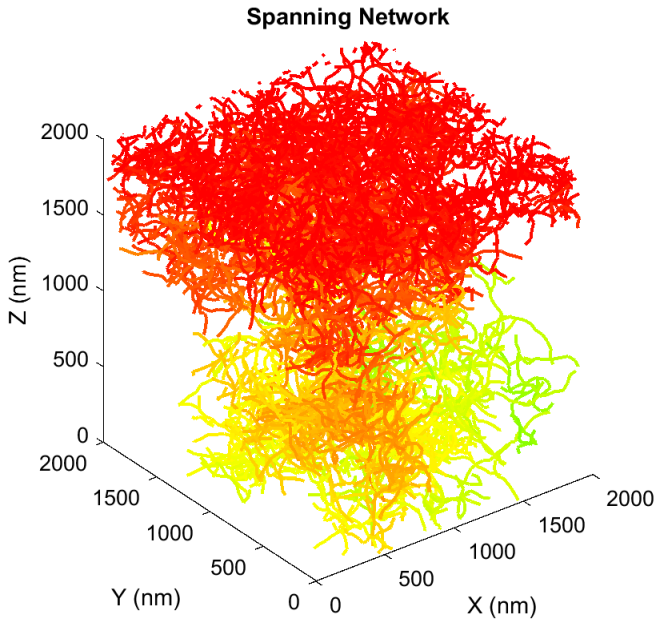

Figure 13. 3D RVE connected network. The same color scheme is used from Figure 12. Percolation also occurs in this RVE.

It is apparent from comparing Figure 12 to Figure 13 that the spanning network algorithm is much more computationally intensive for the 3D RVE because of the higher number of CNTs that must be checked. Numerical comparisons between the 2D and 3D models will be made in Chapter 5.

The final step in the current procedure is to eliminate duplicate connections that are made between two CNTs along the same checker fiber segment. The creation of additional nodes to be used as searching points often leads to multiple recorded contacts along the same segment. These are eliminated so that only a single contact is recorded between two corresponding segments. It is possible for two fibers to connect at different contact points due to their waviness, which creates a parallel resistor. The identification of a spanning CNT network sets the stage for conversion to a resistor network and the calculation of the effective electrical and thermal conductivities of the nanocomposite.

Chapter 3

The Resistor Network Model

3.1 Synopsis

If a spanning network of CNTs is found to exist using the methods in the previous chapter, then the next step is to convert the fibers into a resistor network and solve the system using finite element analysis (FEA) in conjunction with Kirchoff's current law (KCL) for electrical transport and Fourier's law for thermal transport. First, the values for the resistance at each fiber segment and contact point must be determined. The resistor network method [40] has proven to be effective for modeling electrical transport in random composite structures and will be utilized here as well. This can also be adapted for use in determining the heat transport properties. KCL is replaced by Fourier's law and a thermal resistor network is created to find the temperature at each point in the network. After all the voltages in the electrical case or temperatures in the thermal case have been determined, post-processing is done to find the effective electrical or thermal conductivity.

3.2 Modeling of Fiber and Contact Resistors

It is critical that the resistance of both CNT fibers and CNT-CNT contact points are included in the model. The conversion of CNT fibers to equivalent resistors will be considered first. It was shown in Chapter 2 that each fiber comprises of ten line segments. Each of these segments can be converted into a resistor with a contact resistance, R_{CNT}, found through the following equation

$$R_{CNT} = \frac{L}{\sigma A} = \frac{4L}{\sigma \pi d^2}, \quad \textbf{(13)}$$

where L is the segment length, d is the nanotube diameter, and σ is the intrinsic CNT conductivity, either electrical or thermal, of the CNT. Equation (13) can be used to calculate both the electrical and thermal resistance for each fiber. The diameter of each CNT is kept constant at 5 nm, so the randomly generated length solely accounts for the variation in the resistance of each fiber. Histograms of randomly generated fiber electrical and thermal resistances are shown in Figures 14 and 15. The Weibull distribution discussed in Chapter 2 is used to obtain the CNT lengths.

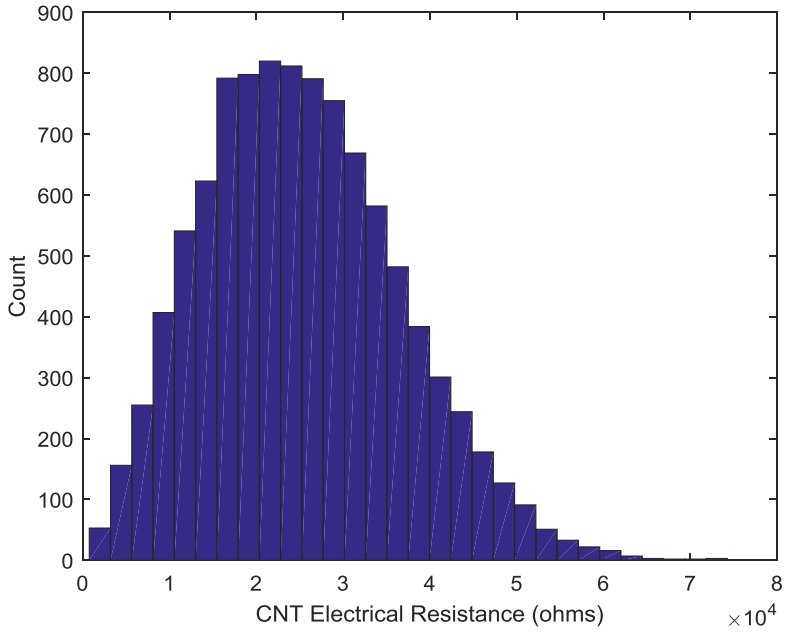

Figure 14. Histogram of 10,000 realizations of electrical R_{CNT}. $\sigma = 10^6$ S/m.

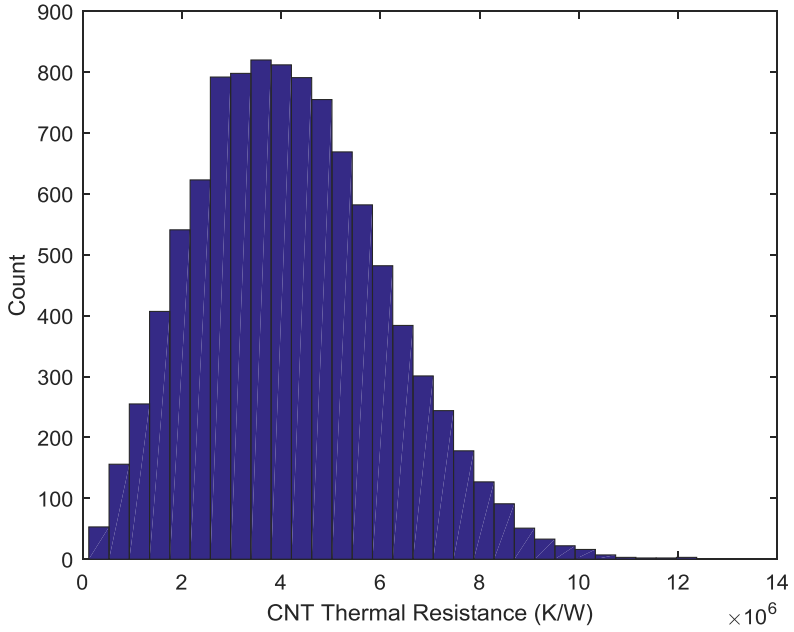

Figure 15. Histogram of 10,000 realizations of thermal R_{CNT}. $\sigma = 6000$ W/mK.

These resistances also follow a Weibull distribution since each length is multiplied and divided by constant values. The conversion of a CNT fiber into equivalent resistors can be better visualized in Figure 16.

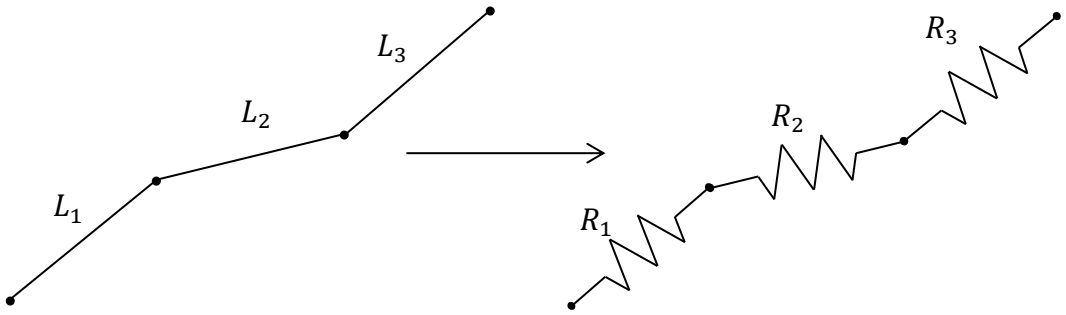

Figure 16. Conversion of a single CNT fiber into a connected series of resistors.

The next step is to model the resistance of CNT-CNT contact points, known as the contact resistance. Electrical contact resistance will be discussed first. Contact resistance has been identified as the largest contributor to the electrical resistance of polymer nanocomposites [29], [36], [57], [83]. However, various methods have been used to represent this resistance. Li and Chou [50] assumed that a layer of polymer separated each contact point in their 2D model and found that the tunneling resistance varied from 10^2 – 10^{16} kΩ. Some authors have used the Landauer-Buttiker [84] formula for calculating the contact resistance of both SWNTs and MWNTs [58], [59]. Models also differ on whether they allow electron tunneling, or the transmission of electrons between CNTs which have a polymer obstacle between them.

The model adopted here represents electrical contact resistance according to the work by Shenogin et al. [29]. This work used molecular dynamics which incorporated the

Landauer-Buttiker formula to solve for the electrical resistance between crossing SWNTs of different chiralities. A depiction of their model can be seen in Figure 17.

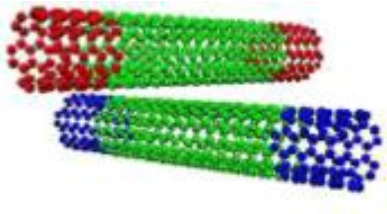

Figure 17. Molecular dynamics model used to calculate electron transport in the gap between two metallic SWNTs crossing at 90˚ with electron source (red) and electron drain (blue) from Shenogin et al. [29].

Note that only metallic nanotubes are used in characterizing the electrical contact resistance. It was found that the contact resistance between two crossing nanotubes gets lower as the distance between the fibers decreases. Since the nanotubes vibrate more as the temperature increases, the effective distance between them tends to decrease causing the contact resistance to decrease. It was also found that resistance increases as the SWNT diameter increases due to the changing charge density profile. The PDF for time-averaged junction conductance for a single contact is given as

$$P(S) = \frac{2T_0}{TS_0}\chi e^{-\chi-\frac{T_0}{T}\chi^2}, \quad \textbf{(14)}$$

where the dimensionless parameter χ is found by

$$\chi = ln\frac{S}{S_0}, \quad \textbf{(15)}$$

which quantifies the conductance at temperature T relative to the static conductance S_0 at 0 K, which is the inverse of the static resistance, R_0. The effective temperature parameter T_0 characterizes the sensitivity of contact conductance to variation of gap size and is given by

$$T_0 = \frac{G\xi^2}{2k_b}, \tag{16}$$

which combines the effective spring constant of the oscillator, G, the length parameter, ξ, and the Boltzmann constant, k_b. The conductance can then be inverted to finally find the contact resistance R_C

$$R_C = \frac{1}{S}. \tag{17}$$

The first step is to sample χ values from the distribution function given in Equation (14). This is done here using Von Neumann's method, where a uniform random variable is first sampled for the independent variable (χ) and then a uniform random variable is sampled for the dependent variable $(P(S) * S_0)$. If the sampled points are below the curve of the actual PDF, then the value for χ is accepted. Otherwise it is rejected and the process is repeated until the desired number of realizations has been sampled. The values found for χ are then used to solve for the conductance, S, through manipulation of Equation (15) which is then used to solve for the contact resistance, R_C, through Equation (17). Equation (14) gives the PDF of time-averaged conductance at a single resistor; however, by making the assumption of ergodicity, the system of fluctuating resistors can be replaced by an equivalent static network of resistors following the same distribution. In other words, the resistance of each contact will be a constant

sampled from the PDF described in Equation (14). The parameters for several different chiralities of SWCNTs are given in Table 1 which is taken from Shenogin et al [29]. Figure 18 shows the given distribution for χ at (10, 10) SWNT structure at 300 K. Figures 19 and 20 give 10,000 realizations from this distribution, and the resulting contact resistances.

CNT Chirality	**(6, 6)**	**(8, 8)**	**(10, 10)**	**(12, 12)**
G (kCal/mol/A^2)	37.82	50.06	61.69	73.8
ξ (A)	0.193	0.201	0.199	0.204
R_0 (MΩ)	5.25	8.20	12.38	18.20
T_0 (K)	354	509	615	773

Table 1. Values of parameters for crossing SWNTs in contact with one another.

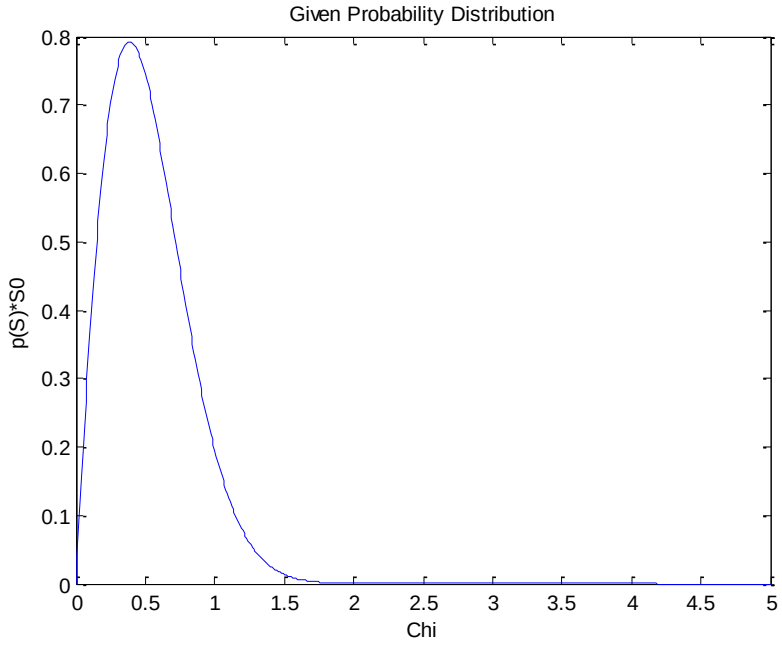

Figure 18. Given distribution of χ for T = 300 K, chirality (10,10).

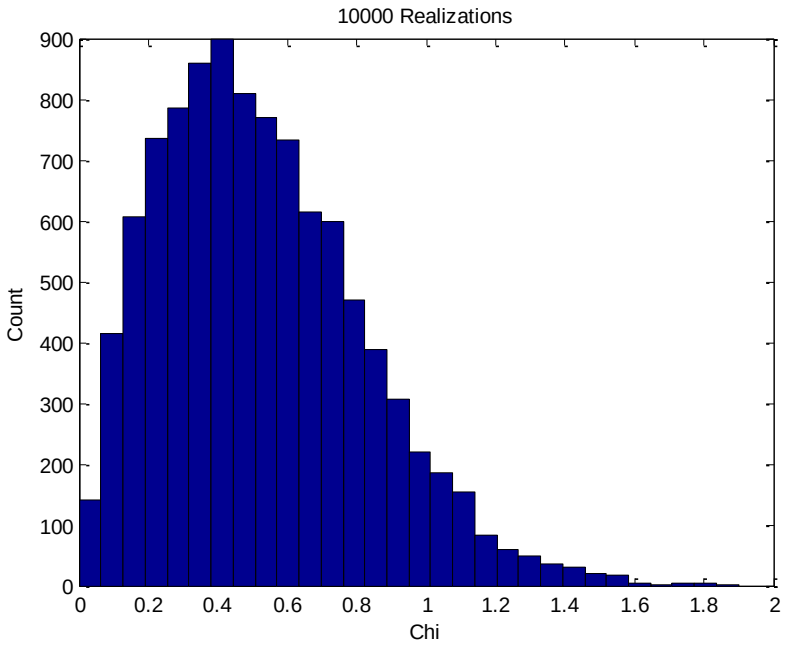

Figure 19. Histogram of 10,000 realizations of χ for T = 300 K, chirality (10,10).

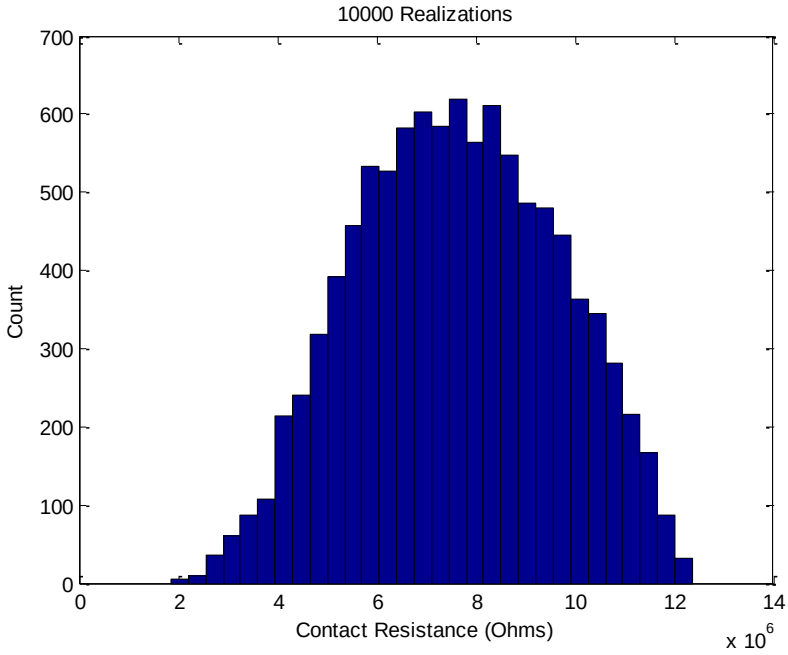

Figure 20. Histogram of 10,000 realizations of R_C for T = 300 K, chirality (10,10).

Comparison of Figure 14 to Figure 20 shows that the electrical contact resistance is much higher than that of the fiber resistance. Due to this, the path of least resistance that makes

up the conductive backbone of the nanocomposite will typically be the path that has the fewest number of contacts between CNTs. The effect of varying temperature and nanotube geometry on the overall nanocomposite electrical conductivity will be discussed in Chapter 5.

The value for thermal contact resistance to be used in the model must now be determined. Foygel et al. [36] used the results from experimental studies on thermal transport in MWNT systems suspended in oil [85] and found the thermal contact resistance to be on the order of $10^7 - 10^8$ K/W, close to the value of the resistance of the CNT fibers themselves. Hu and Cao [83] created a nonequilibrium molecular dynamics method to calculate the thermal resistance between crossed CNTs, similar to the method used by Shenogin et al. described previously. Their model is shown in Figure 21.

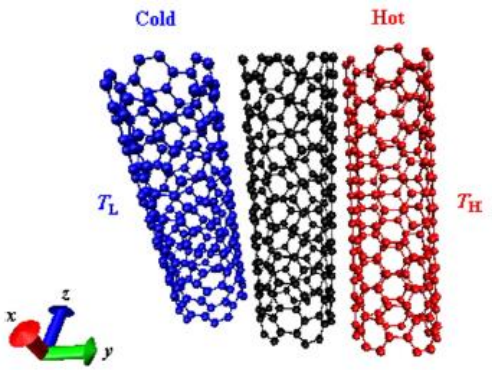

Figure 21. Molecular dynamics model used to calculate thermal transport three SWNTs with heat source (red) and cold drain (blue) from Hu and Cao [83].

Like the electrical model, the thermal model revealed that the thermal contact resistance decreased as the gap between the nanotubes decreased. The resistance was found to be on the order of $10^9 - 10^{11}$ K/W, significantly larger than the range given by experimental results. For the present work, the thermal contact resistance is set as a constant in the

range of values reported in the literature. The effect of thermal contact resistance on the overall thermal conductivity will also be discussed in Chapter 5.

Once both the fiber and contact resistance values have been established, all the segments and contacts in the spanning network can next be assigned a resistance using the methods listed above. The location of the contacts is determined from the searching component of the spanning network algorithm as described in Chapter 2. An example of the conversion of connected fibers to resistors is shown in Figure 22.

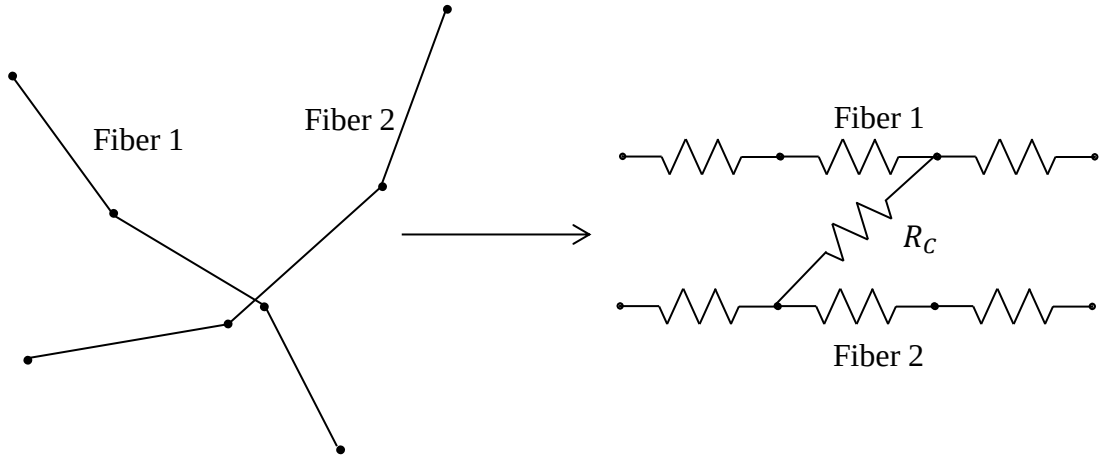

Figure 22. Conversion of connecting fibers to an equivalent resistor network.

3.3 Electrical FEA Techniques

Electrical transport in the nanocomposite will now be described through FEA in conjunction with KCL. The application of KCL to resistor networks is well established [40]. The foundational principal is conservation of electrical charge. It states that the sum of the currents flowing into a node is equal to the sum of the currents flowing out of the node. Furthermore, the current entering and exiting each resistor must be the same. This applies to each resistor in the model as well as the nanocomposite as a whole. The current

entering the top of the RVE must be equal and opposite to the current exiting the bottom since no charge is being built up within the RVE. FEA is used to solve for the voltage at each node in the spanning network, and then post-processing is conducted to calculate the current through each element. This is done so that the overall electrical conductance and conductivity of the RVE can be found.

Each component in the network, including fiber segments and contacts, is modeled as a one-dimensional linear resistor element. Suppose there are two nodes in contact, node *i* and node *j*. The current exiting node *i* and entering node *j* are equal in magnitude, but opposite in direction. Applying Ohm's law at each node gives the equations

$$I_i^e = \frac{1}{R^e}(V_i - V_j), \tag{18}$$

$$I_j^e = \frac{1}{R^e}(V_j - V_i). \tag{19}$$

Equations (18) and (19) can be converted to matrix form as

$$\begin{bmatrix} I_i^e \\ I_j^e \end{bmatrix} = \left[\boldsymbol{K_{ij}^e}\right] \begin{bmatrix} V_i \\ V_j \end{bmatrix}, \tag{20}$$

where

$$\left[\boldsymbol{K_{ij}^e}\right] = \frac{1}{R^e}\begin{bmatrix} 1 & -1 \\ -1 & 1 \end{bmatrix}. \tag{21}$$

This is the finite element formation for a single resistor element. There are cases where the node may receive contributions from more than two components. The total sum of currents at a node must always equal zero. The local elements are gathered to form the global system matrices which are of the form

$$\boldsymbol{I} = \boldsymbol{KV}, \tag{22}$$

where $\boldsymbol{I}$ is the vector of external input currents, $\boldsymbol{K}$ is the global coefficient matrix, and $\boldsymbol{V}$ is the vector of nodal voltages. There are no external input currents, so here $\boldsymbol{I}$ is simply a vector of zeros. The global coefficient matrix is assembled using all the local element matrices described in Equation (20). This is done using the connectivity information from the spanning network algorithm according to standard FEA procedures [86].

Once the global matrices have been assembled, essential boundary conditions must be applied to make the system non-singular. The applied boundary conditions are 100 V to nodes on the top edge and 0 V to nodes on the bottom edge. The non-conducting sides of the RVE are kept insulated. This can be visualized in Figure 23 for the 2D case. The 3D case is similar except that the 100 V boundary condition is applied to the entire +Z face and the 0 V condition is applied to the –Z face while the other faces are kept insulated.

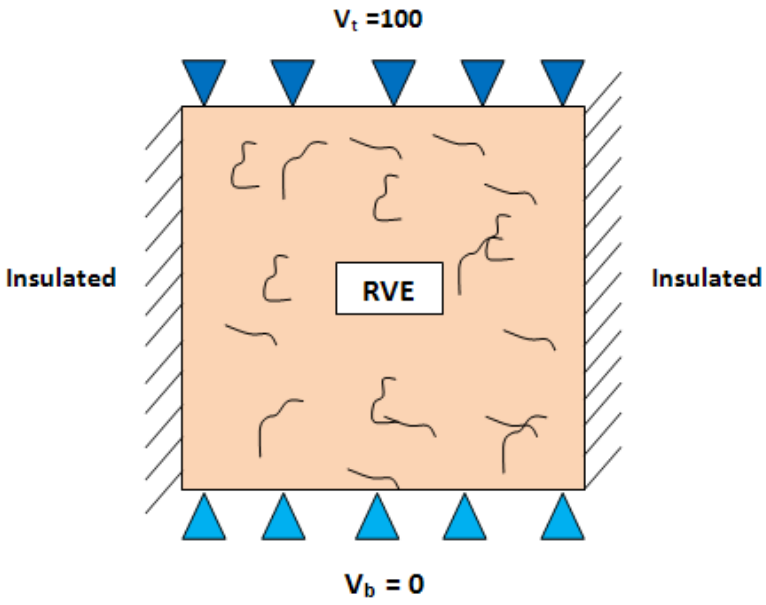

Figure 23. 2D RVE with applied boundary conditions. The top face is the source and the bottom face is the drain, causing current to flow from top-to-bottom, from Ward [77].

After the boundary conditions are applied the system becomes unique. The nature of the problem creates symmetric $\boldsymbol{K}$ matrices, so Cholesky factorization is used to efficiently and accurately calculate the voltage at each node, $\boldsymbol{V}$.

After $\boldsymbol{V}$ has been found, post-processing is necessary to calculate the current through each element. This yields two important results: the identification of the backbone, and the sum of currents through the top and bottom boundaries. The backbone is the portion of the CNT network where most of the current flows. Current will flow through the path of least resistance, so although there may be many percolating paths through the RVE, only a few CNTs will actually carry current. The current at each node can be calculated through solving Equation (18) at each fiber segment and contact point. The total current entering the nanocomposite is found by summing the currents at all resistors contacting the top of the RVE.

$$I_{total} = \sum_{j=1}^{n} I_j^e, \quad \textbf{(23)}$$

The principle of KCL states that the current entering and exiting an electrical component not building charge must equal zero, so the sum of the currents at the bottom boundary is equal and opposite to I_{total}.

The sum of the currents at the boundaries allows for the effective conductance, G_{eff}, to be determined through manipulation of Ohm's law in the following equation

$$G_{eff} = \frac{I_{total}}{(V_t - V_b)}, \quad \textbf{(24)}$$

where V_t and V_b are the applied voltage essential boundary conditions. The effective conductivity, σ_{eff}, is found by taking into account RVE dimension size, which differs for 2D and 3D RVEs

$$\sigma_{eff} = G_{eff} \frac{Length}{Area}, \quad \textbf{(25)}$$

$$\sigma_{eff} = G_{eff} \frac{L_y}{L_x * t} \quad \text{(2D RVEs), and} \quad \textbf{(26)}$$

$$\sigma_{eff} = G_{eff} \frac{L_z}{L_x * L_y} \quad \text{(3D RVEs),} \quad \textbf{(27)}$$

where L_x, L_y, and L_z, are the RVE dimension lengths and t is the 2D RVE thickness. The results from a 2D RVE electrical finite element solution are given next. 2D RVE figures are used for the sake of clarity in comparison to those of 3D RVEs. The same generated nanocomposite is shown in Figures 24 – 26.

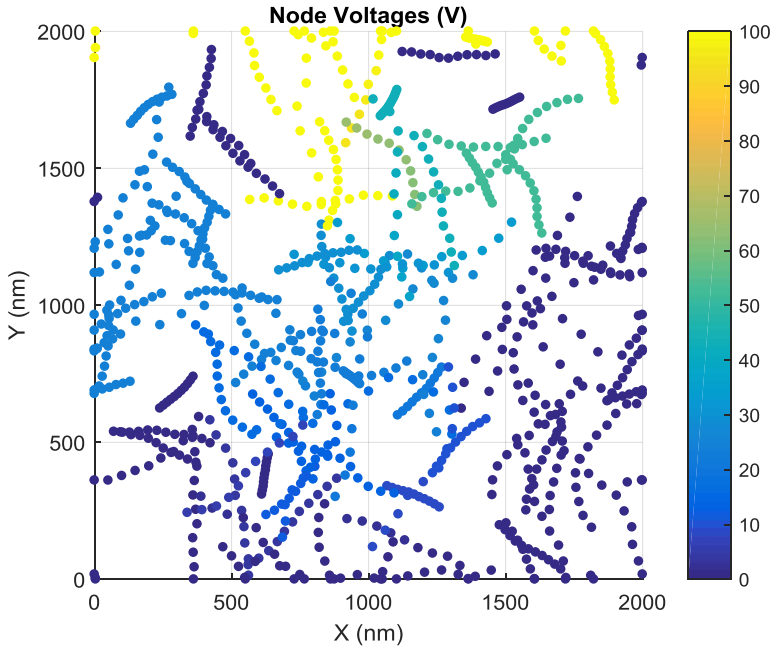

Figure 24. 2D RVE nodal voltages, volume fraction = 2% (Periodic Boundary Conditions).

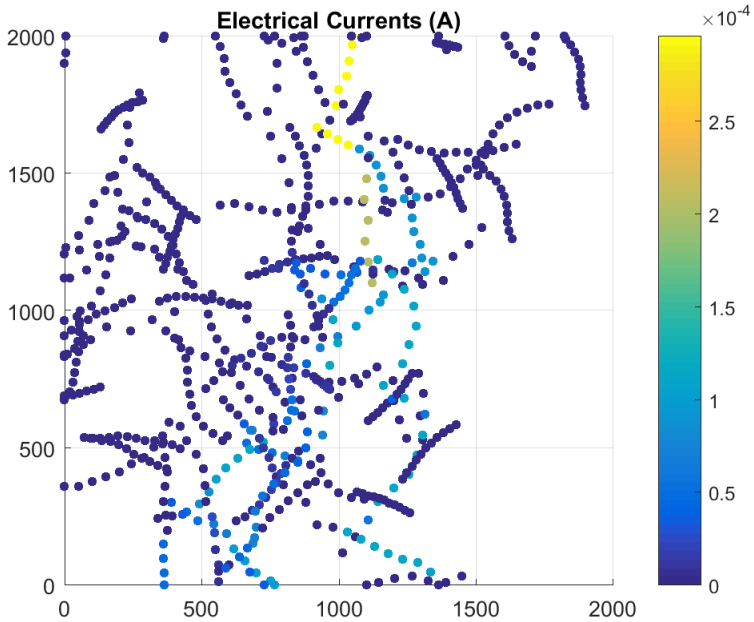

Figure 25. 2D RVE element currents, volume fraction = 2% (Periodic Boundary Conditions).

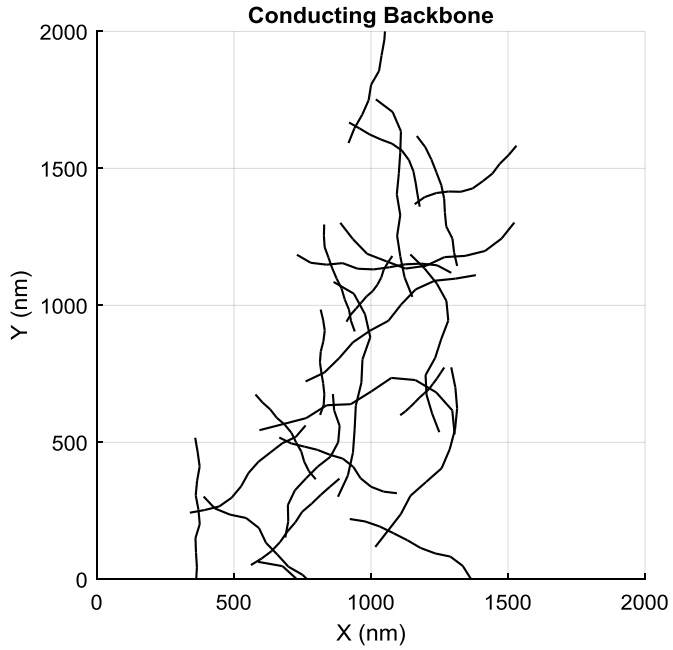

Figure 26. 2D RVE electrical backbone, volume fraction = 2% (Periodic Boundary Conditions).

3.4 Thermal FEA Techniques

Thermal transport in the RVE is handled in a similar manner as electrical transport, though there are some key differences. Fourier's law rather than KCL is applied to the resistor network. Fourier's law states that the time rate of heat transfer through a material is proportional to the negative gradient of the temperature. A steady-state system has the same amount of heat flowing in and out, analogous to KCL where the sum of currents at a node is equal to zero. This applies to each individual segment and contact resistor as well the RVE as a whole; the amount of heat coming in through the top boundary must be the same as the heat leaving through the bottom boundary. FEA is used to solve for the temperature at each node in the spanning network, and then post-processing is conducted to calculate the heat flux at each node. As in the electrical case,

this results in identification of the conducting backbone and overall thermal conductance of the RVE.

Each component is again modeled as a linear resistor, but now Fourier's law is applied to solve for the temperature at each node rather than the voltage. This is shown in the equations

$$Q_i^e = \frac{1}{R^e}(T_i - T_j), \tag{28}$$

$$Q_j^e = \frac{1}{R^e}(T_j - T_i). \tag{29}$$

which represent two nodes, node *i* and node *j*, in contact where Q denotes the heat flow, R represents the thermal resistance, and T denotes the temperature. These can be represented in matrix form as

$$\begin{bmatrix} Q_i^e \\ Q_j^e \end{bmatrix} = [\boldsymbol{K_{ij}^e}] \begin{bmatrix} T_i \\ T_j \end{bmatrix}, \tag{30}$$

where

$$[\boldsymbol{K_{ij}^e}] = \frac{1}{R^e}\begin{bmatrix} 1 & -1 \\ -1 & 1 \end{bmatrix}. \tag{31}$$

The thermal case differs from the electrical case in that the thermal conductance of the matrix can no longer be ignored because it significantly contributes to heat transport in the nanocomposite. For the electrical case, the ratio between the CNT and polymer conductivity is around 20 orders of magnitude. For the thermal case, this ratio is only about 4-5 orders of magnitude. Therefore, a resistor must be added in parallel to the CNT network that accounts for thermal transport through the polymer, as shown in Figure 27.

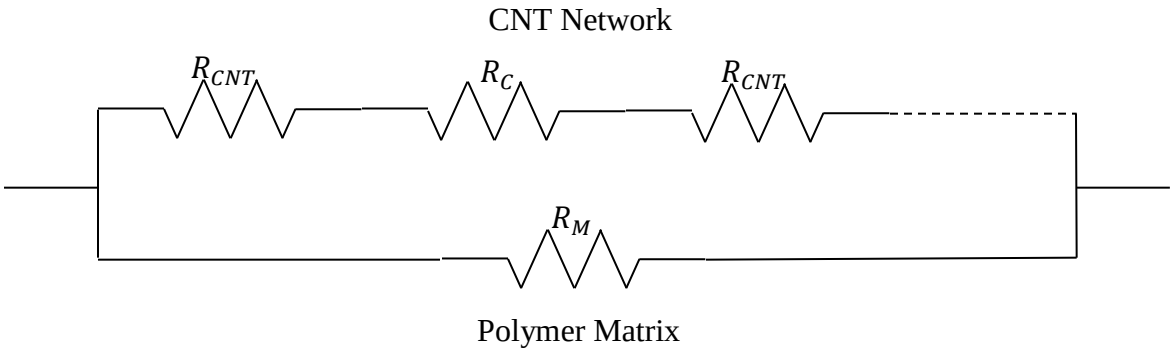

Figure 27. Addition of a parallel resistor representing the polymer matrix to the resistor network for the case of heat transport modeling in the RVE.

The resistance of the polymer matrix R_M is found through the following equation

$$R_M = \frac{L}{A(1-p)\sigma_M}, \quad \textbf{(32)}$$

where L is the length of the conducting direction, A is the cross-sectional area, p is the volume fraction of CNT fillers, and σ_M is the intrinsic polymer matrix conductivity. Equation (32) shows that the resistance of polymer increases as more CNTs are added because there is then less polymer material available to transport heat. A linear resistor can be created for the polymer matrix through Equation (31). Global matrices can now be assembled as was done for the electrical transport

$$\boldsymbol{Q} = \boldsymbol{KT}, \quad \textbf{(33)}$$

where $\boldsymbol{Q}$ is the vector of external heat flux, $\boldsymbol{K}$ is the global coefficient matrix, and $\boldsymbol{T}$ is the vector of nodal temperatures. Essential boundary conditions must be applied as before to make the system non-singular. This time a temperature of 100 K is applied to the top of the RVE and 0 K will be applied to the bottom with the non-conducting sides insulated.

This forces the heat to flow from top-to-bottom and can be visualized for the 2D case by examination of Figure 23 but replacing the voltage boundary conditions with the temperature. Cholesky factorization is again used to solve for $\boldsymbol{T}$ since $\boldsymbol{K}$ is symmetric.

The post-processing for thermal transport mirrors that of electrical transport exactly, except that this time attention is focused on summing the heat flux at the top of the RVE to determine its effective thermal conductance

$$Q_{total} = \sum_{j=1}^{n} Q_j^e, \tag{34}$$

$$G_{eff} = \frac{Q_{total}}{(T_t - T_b)}, \tag{35}$$

where T_t and T_b are the applied essential boundary conditions and Q_{total} is the sum of the heat flux of CNTs located at the top boundary. The effective thermal conductivity, σ_{eff}, is found in the same exact manner as the electrical case through use of Equations (25 - 27). The results from a thermal transport 2D RVE problem can be seen in Figures 28 – 30.

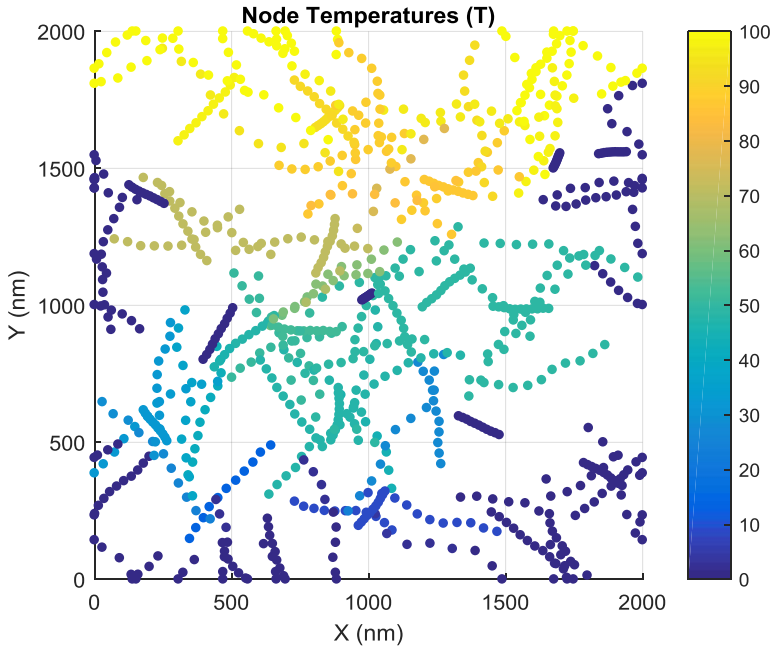

Figure 28. 2D RVE nodal temperatures, volume fraction = 2% (Periodic Boundary Conditions).

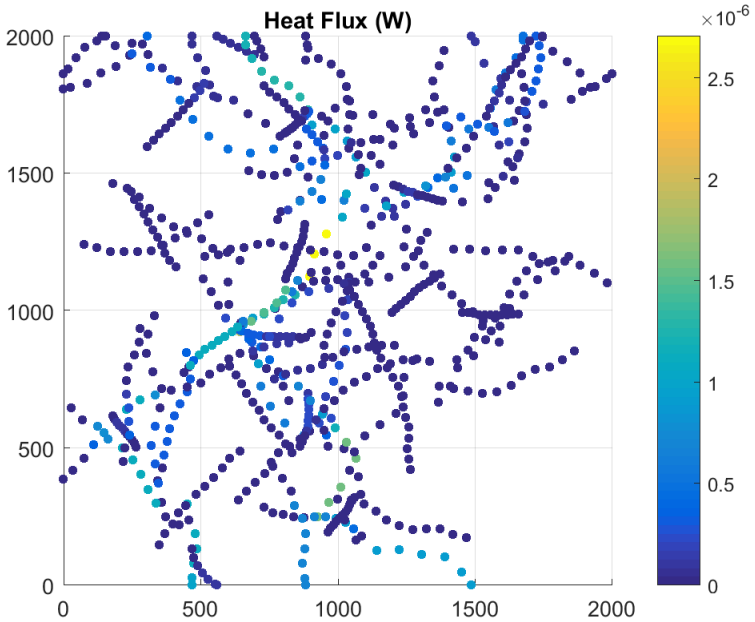

Figure 29. 2D RVE element heat flux, volume fraction = 2% (Periodic Boundary Conditions).

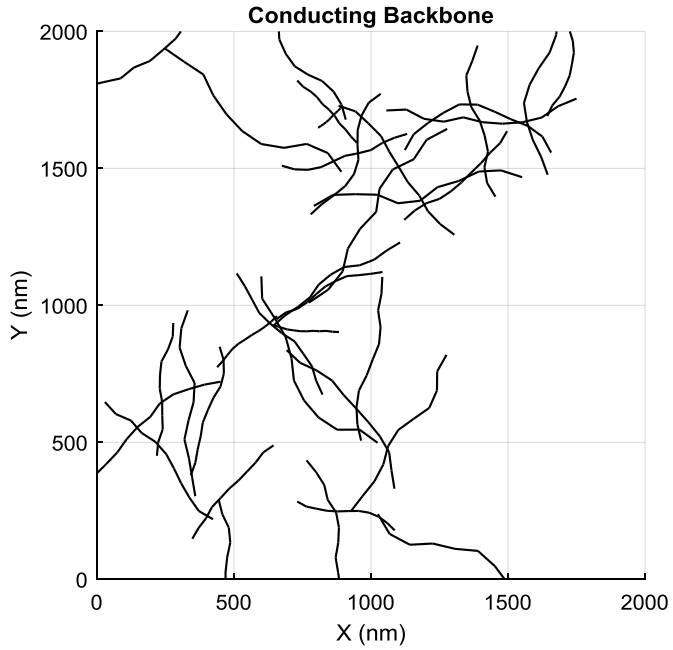

Figure 30. 2D RVE thermal backbone, volume fraction = 2% (Periodic Boundary Conditions).

Chapter 4

Simulation Methods

4.1 Synopsis

The computation time required to calculate the properties of a single RVE can range from a few seconds to hours depending on the volume fraction of CNT filler. Considering that Monte Carlo simulations require multiple simulations to derive an accurate overall average, short computation times are necessary for the model to be a useful resource. Described in this chapter are several methods to treat the boundaries of RVEs so that accurate results may be obtained while lowering the overall computation cost. As mentioned earlier in this thesis, increasing the size of the RVE dimensions improves the accuracy of the results, but also lengthens the computation time by increasing the number of CNTs and contact points. Each of the methods listed within this section has a different way of dealing with RVE dimension size and RVE boundaries. 2D and 3D models have been developed for each of the described methods.

4.2 Method 1 – Periodic Boundary Conditions

Method 1 is based on previous models developed at Rice University which used periodic boundary conditions to account for CNTs that cross RVE boundaries [77]. This creates a realistic amount of CNTs in contact with each boundary, though it adds bias to the location of these fibers. This method does not account for conductance through the non-conducting boundaries; therefore, large RVE dimensions must be used to obtain accurate results. All of the RVE figures presented thus far have been from the use of this method. A 3D RVE and its corresponding backbone generated from Method 1 are shown in Figure 31. Even though several thousand CNTs are generated, only a fraction of these carry a substantial amount of current or heat flow.

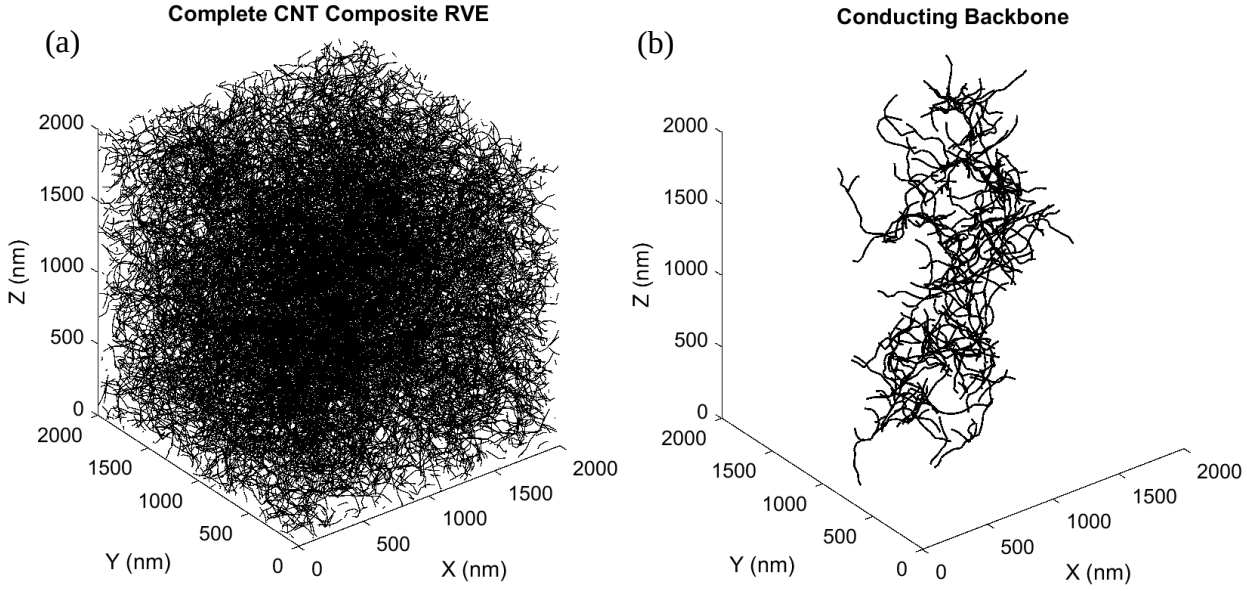

Figure 31. Method 1 3D RVE, volume fraction = 0.6%. (a) Total RVE geometry. (b) Conducting backbone of RVE.

4.3 Method 2 – Non-Periodic Boundary Conditions

Method 2 is a simple adjustment developed in this thesis to circumvent the use of periodic boundary conditions and the associated CNT location bias. Non-periodic boundary conditions are used as described in Chapter 2, where CNTs are generated in a larger area or volume extending outward from desired RVE boundaries. Fibers outside the desired RVE are then removed and modeling is conducted only on the remaining RVE. This is demonstrated in the 2D case in Figure 32. In this example, a margin equal to the RVE length is added in the positive and negative directions of each dimension. The used RVE is then cut from the middle of this generated geometry. A simplified version of this process is shown in Figure 8 for a 2D RVE.

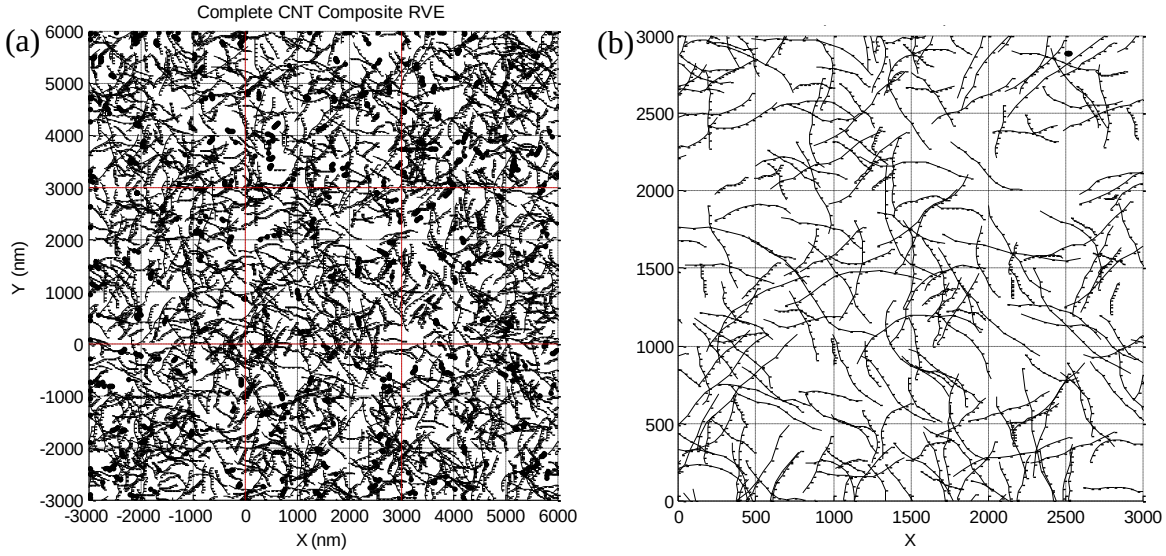

Figure 32. Method 2 2D RVE, volume fraction = 2%. (a) Total area of generated CNTs. (b) RVE cut out of the middle of the generated area.

This method creates a realistic RVE by maintaining accurate amounts of boundary crossings without generating bias in their locations. However, like Method 1, it does not

account for transport through the non-conducting boundaries and thus requires large RVE dimensions to yield accurate results.

4.4 Method 3 – Transport Across Periodic Boundaries

Method 3 is based on the work described in [47], [58]. In this method, current is allowed to transfer through fibers that are cut-and-relocated to the opposite boundary in the non-conducting direction through the use of periodic boundary conditions. Further, current can only flow through fibers located at the same non-conducting positions on the conducting boundaries. Alternatively stated, both the top and bottom portions of the fiber on the conducting boundary must be in the spanning network for them to be able to transport electricity and heat. This creates a plausible transport network when the RVEs are repeated to form a larger system. This can be better visualized through Figure 33. Observing Figure 33 (c), it is shown that current cannot flow through the fiber at the top-middle of the RVE because its cut-fiber on the bottom is not a part of the spanning network.

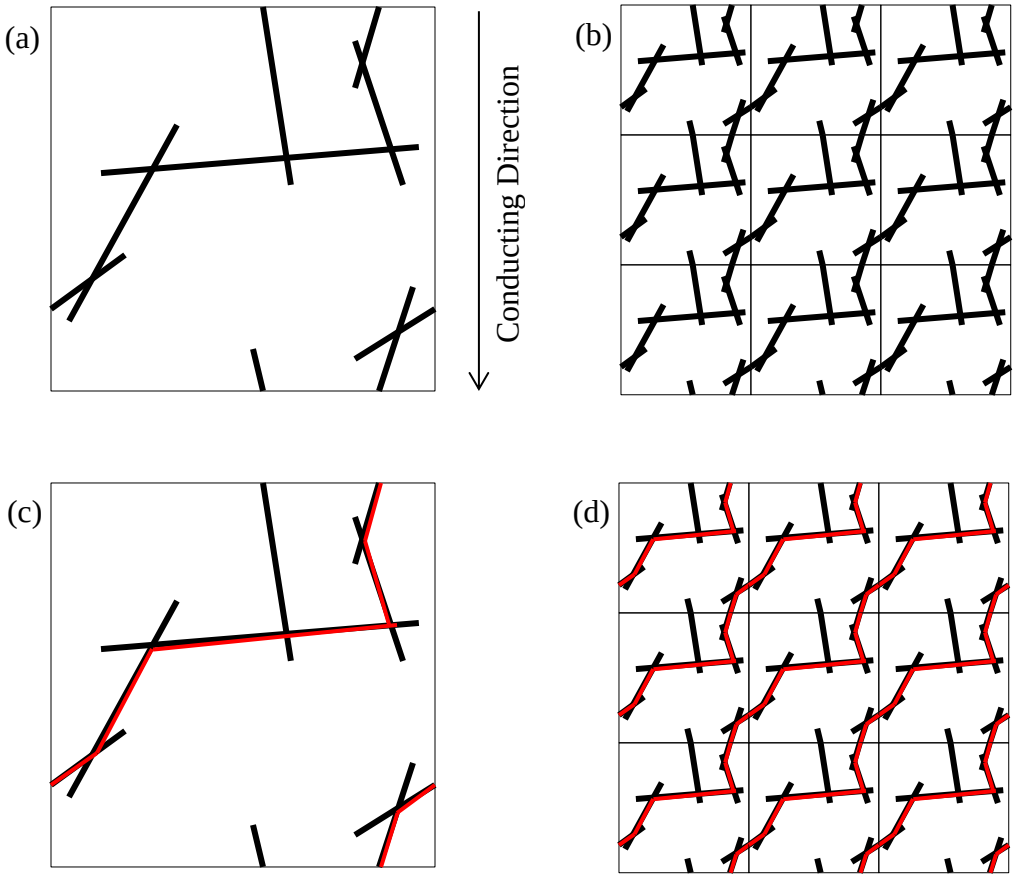

Figure 33. (a) 2D RVE with periodic boundary conditions, does not percolate using typical constraints. (b) Creation of a larger system through repeated use of RVE, shows that current flow should be possible if used in repeated system. (c) Spanning network constructed through Method 3, RVE is now percolated. (d) Visualization of current flow through larger repeated system.

Since this method accounts for transport through the non-conducting boundaries, the authors claimed that this method can be used with smaller RVE sizes and still yield accurate results. This will be verified in Chapter 5. Figure 34 shows a 2D RVE generated using Method 3, where the current is able to jump boundaries so that the conducting backbone jumps between the left and right boundaries.

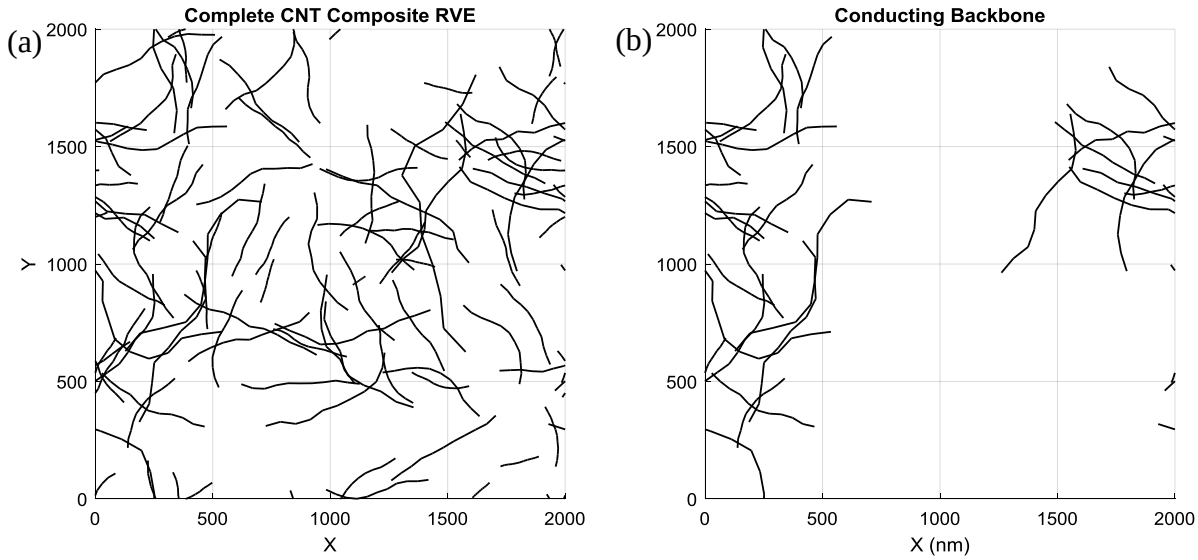

Figure 34. Method 3 2D RVE, volume fraction = 2%. (a) Generated RVE with periodic boundary conditions. (b) Conducting backbone where the current jumps the non-conducting boundaries.

4.5 Method 4 – Split RVEs

Method 4 is based on the findings referenced in [59] and addresses transport through the non-conducting boundaries, though it does this in a different manner than Method 3. Method 4 does not use periodic boundary conditions because of their inherent bias. Instead, CNTs are generated in a rectangular surface of dimension $2L_x \times L_y$ in the 2D case and a rectangular cuboid of dimension $2L_x \times L_y \times L_z$ in the 3D case using non-periodic boundary conditions. The rectangular RVE is then split into two separate RVEs so that a total of three RVEs are created. A simplified version of this is shown in Figure 35 and an actual output from the model is shown in Figures 36 and 37 for the 2D case.

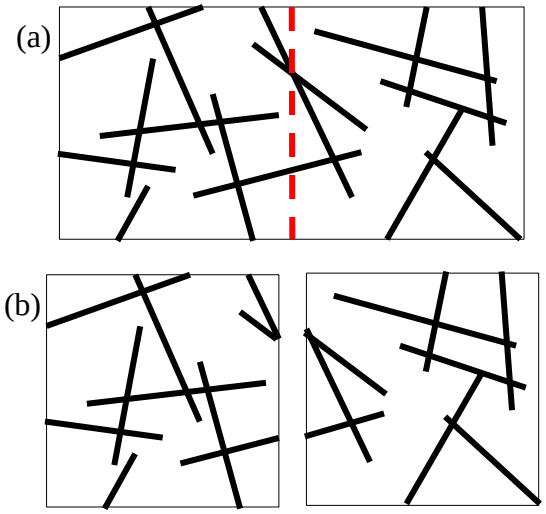

Figure 35. Simplified Method 4 representation. (a) Rectangular RVE with the size of a single non-conducting dimension doubled. (b) RVEs created from left and right half of rectangular RVE.

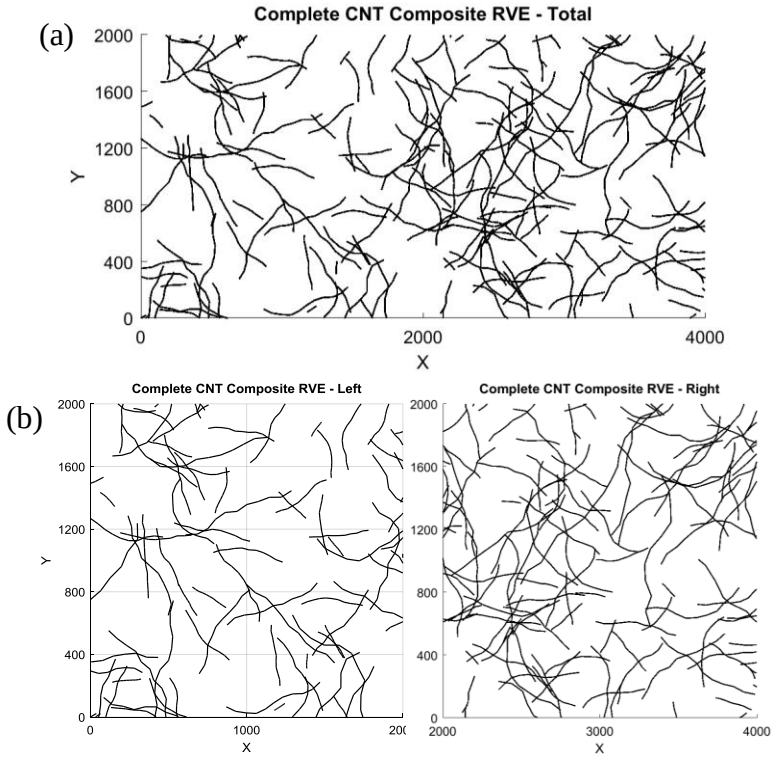

Figure 36. Method 4 2D RVE, volume fraction = 2%. (a) Generated rectangular RVE with non-periodic boundary conditions. (b) Creation of two additional RVEs from rectangular RVE.

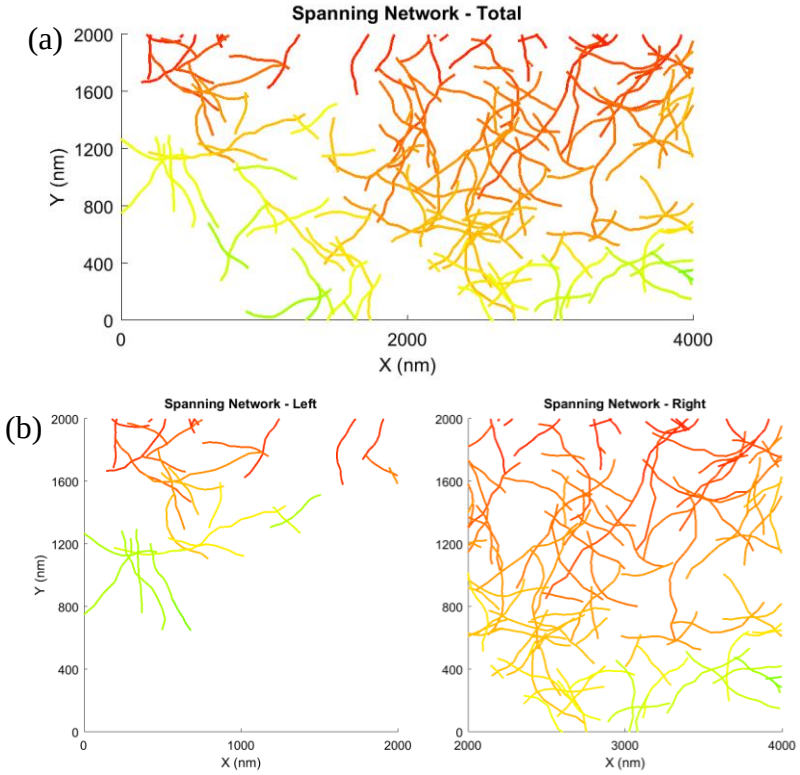

Figure 37. Method 4 2D RVE spanning network, volume fraction = 2%. (a) Spanning network of rectangular RVE. (b) Spanning network of left and right RVEs. It is apparent that severing the boundary cuts off many connections and does not allow the left side alone to become percolated.

The left, right, and rectangular RVE are all separately solved. The critical concept of this method is that additional transport through the boundary can be estimated by comparing the conductance of the rectangular RVE to that of the divided RVEs which can have networks severed by the splitting of the RVE. The average of the left and right RVE conductance is denoted as G_{RVE} and the conductance of the rectangular RVE is G_{Rect}. $G_{Boundary}$ is the contribution to the conductance from the non-conducting boundaries. The overall system can be represented by the equation

$$G_{Rect} = 2G_{RVE} + 2G_{Boundary}. \quad \textbf{(36)}$$

For 2D RVEs, the +X and –X sides contribute to the conductance of the RVE. For the 3D case, the +X, –X, +Y, and –Y faces all contribute to the conductance of the RVE. The adjusted conductance for the RVE, G_{Adj}, can then be found for the 2D case as

$$G_{Adj} = G_{RVE} + 2G_{Boundary} \quad \text{(2D RVE), and} \tag{37}$$

$$G_{Adj} = G_{Rect} - G_{RVE} \quad \text{(2D RVE),} \tag{38}$$

and for the 3D case as

$$G_{Adj} = G_{RVE} + 4G_{Boundary} \quad \text{(3D RVE), and} \tag{39}$$

$$G_{Adj} = 2G_{Rect} - 3G_{RVE} \quad \text{(3D RVE).} \tag{40}$$

The effective conductivity can then be found for both the 2D and 3D case as shown in Equations (25 – 27). The authors claimed that computation time for this model could be further decreased by using smaller RVE dimensions in the non-conducting dimensions and maintaining larger dimensions in the conducting dimension. This means that although three systems have to be solved in each simulation, the overall computation time is reduced because the size of each RVE is much smaller. This finding will be validated in Chapter 5.

4.6 Monte Carlo Simulations

Due to the stochastic nature of this problem, every generated RVE is unique. Two RVEs created with the same input parameters can have significantly different electrical or thermal transport properties. Therefore, it is necessary to use Monte Carlo simulations where many RVEs are generated for each set of input parameters and the results are averaged to obtain a representative value for that set of input parameters. The number of simulations necessary to obtain an accurate approximation will be discussed in Chapter 5 for the 2D and 3D cases.

Monte Carlo simulations, KCL, Fourier's law, and FEA have all been incorporated into the model. The numerical process is straightforward and relatively easy to implement. The challenge comes from the need to achieve accurate physical representation of the nanotubes as well as their electrical and thermal transport behavior. This is manifested in the input parameters, which include CNT geometry, RVE dimensions, CNT morphology, number of bins, number of RVEs, boundary conditions, matrix and CNT intrinsic conductivities, fiber resistances, contact resistances, and simulation method. The ability to vary these parameters to model any CNT/polymer nanocomposite desired is what gives the model its versatility and flexibility. The general procedure for performing the Monte Carlo simulations is shown in Figure 38.

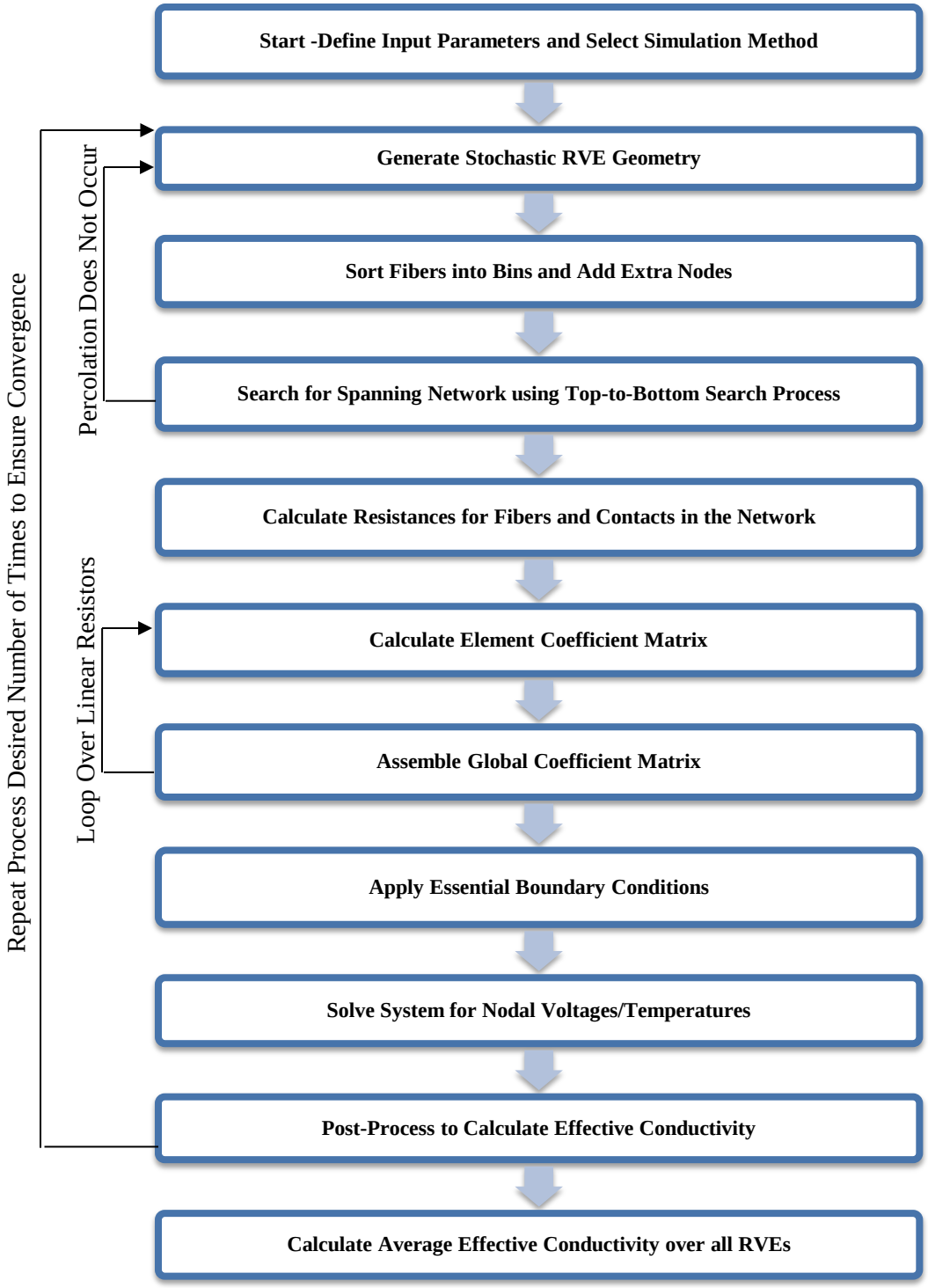

Figure 38. A block diagram of the Monte Carlo simulation process is depicted. RVEs that do not percolate are do not enter the resistor network portion of the model and the conductivity is found based on the properties of the matrix material alone.

Chapter 5

Numerical Results

5.1 Synopsis

The results of the proposed model are assessed in this chapter. First, a Monte Carlo convergence analysis is performed to determine how many simulations are necessary for both the 2D and 3D models and to compare their results. Then, the postulate that periodic boundary conditions result in bias is tested followed by an investigation on the effect of non-conducting dimension length for the split RVE method. Convergence features of all the methods listed in Chapter 4 with varying RVE dimensions are then presented. An optimal simulation method is chosen based on accuracy and computation cost. Finally, simulated results for electrical and thermal conductivity are compared to experimental data, and power laws are developed to calculate the effective conductivity at any volume fraction in the percolation region.

5.2 Model Convergence Analysis

The purpose of the convergence analysis is to verify that the number of RVEs being generated is sufficient and to ensure that the RVE dimension size is large enough for each method to obtain accurate results. Ideally, the four different methods described

in Chapter 4 will converge to similar values even though each uses different procedures to account for transport through RVE boundaries. All stochastic input parameters save location and initial orientation will be held constant for this analysis. Holding these parameters constant limits the variability due to stochastic parameters, giving greater insight to the inherent characteristics of each method. Only the electrical properties are considered here, since these are more notably enhanced due to the formation of spanning CNT networks. The parameters to be used in this analysis are listed in Table 2. An overview of the simulation methods from Chapter 4 is given in Table 3.

INPUTS		
CNT length	500	nm
CNT diameter	5	nm
CNT conductivity	1E+07	S/m
Matrix conductivity	1E-12	S/m
Contact resistance	1E+05	Ω
Number of RVEs	500(2D), 100(3D)	
RVE thickness (2D)	10	nm
Maximum waviness	0	radians
Applied potential (Top)	100	V
Applied potential (Bottom)	0	V

Table 2. Convergence analysis parameters. To gain better insight to the behavior of each model and limit variability due to inputs, stochastic parameters are held to constants.

SIMULATION METHODS	
Method 1	Periodic Boundary Conditions
Method 2	Non-Periodic Boundary Conditions
Method 3	Transport Across Periodic Boundaries
Method 4	Split RVEs

Table 3. Overview of simulation methods for generating RVEs.

A maximum waviness angle (θ_{max}) of zero means that every CNT will be generated as a straight rod rather than a collection of wavy line segments. One of the benefits of this model is that the percolation ratio, the ratio of RVEs that percolate over the total number of RVEs, is also found for each volume fraction. According to percolation theory [30], there is a critical volume fraction at which the percolation ratio spikes upward known as the percolation threshold. This corresponds to a spike in the effective electrical conductivity since more percolated RVEs results in a higher average conductivity.

First, the number of RVEs that must be generated for each volume fraction must be determined. Previous models developed at Rice University [73], [75]–[77] have used 500 RVEs for each data point; however, these were all for 2D nanocomposite models. This number must be scrutinized for 3D models used in the present work. The normalized average conductivity results are presented in Figure 39 for 2D and 3D models. The purpose of these graphs is to show how many RVEs are necessary for the average conductivity to converge. This is done using only Method 1 since the other methods are expected to have similar results when comparing their 2D and 3D models.

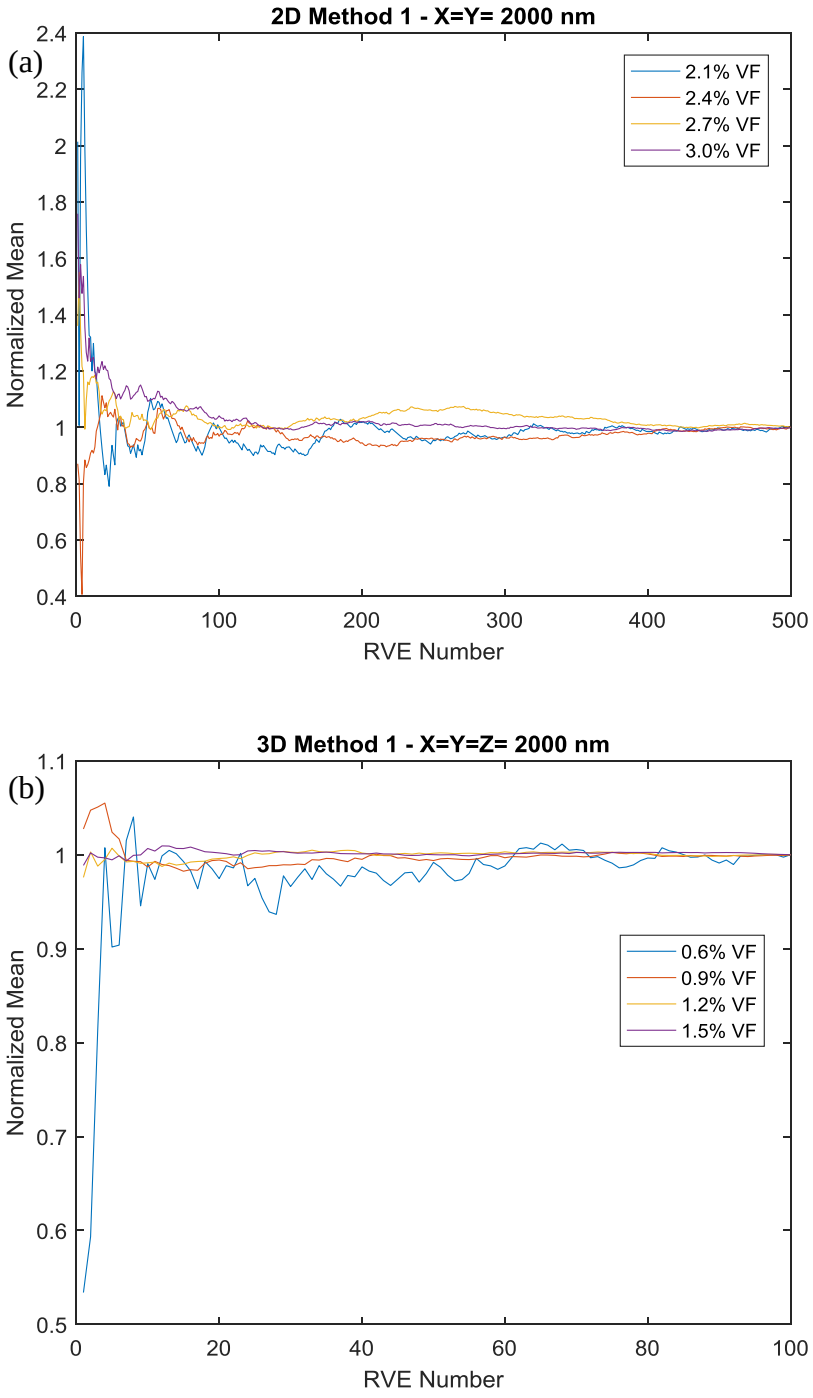

Figure 39. Normalized mean conductivity as the number of RVEs increases. (a) 2D model using 500 RVEs. (b) 3D model using 100 RVEs.

Figure 39 shows that the 3D model converges to the normalized mean much more rapidly than the 2D model even though fewer simulations are used. This is especially true for the higher volume fractions. This is due to the greater number of CNTs produced within the 3D model. A 3D RVE produced by Method 1 with $L_x = L_y = L_z = 4L$, where L is the average length of each CNT, produces over 20,000 CNTs at 2% volume fraction of filler. On the other hand, a 2D RVE with X- and Y-dimensions of the same size produces about 100 CNTs at this volume fraction. The high number of CNTs in the 3D model means that similar networks tend to form for each RVE with the same input parameters. The random placement and orientation of CNTs in the 2D model has a much higher impact on the overall results, leading to more variation between each RVE. In light of these results, the choice of 500 RVEs for the 2D model and 100 RVEs for the 3D model are deemed sufficient to obtain an accurate average value at each data point.

The next step is to compare the actual results obtained from use of the 2D and 3D models. Again, only Method 1 is tested here since it is the effect of the dimensionality and not the procedures of each method that is being compared. Figure 40 shows the comparison between percolation ratio, effective conductivity, and average run time per simulation.

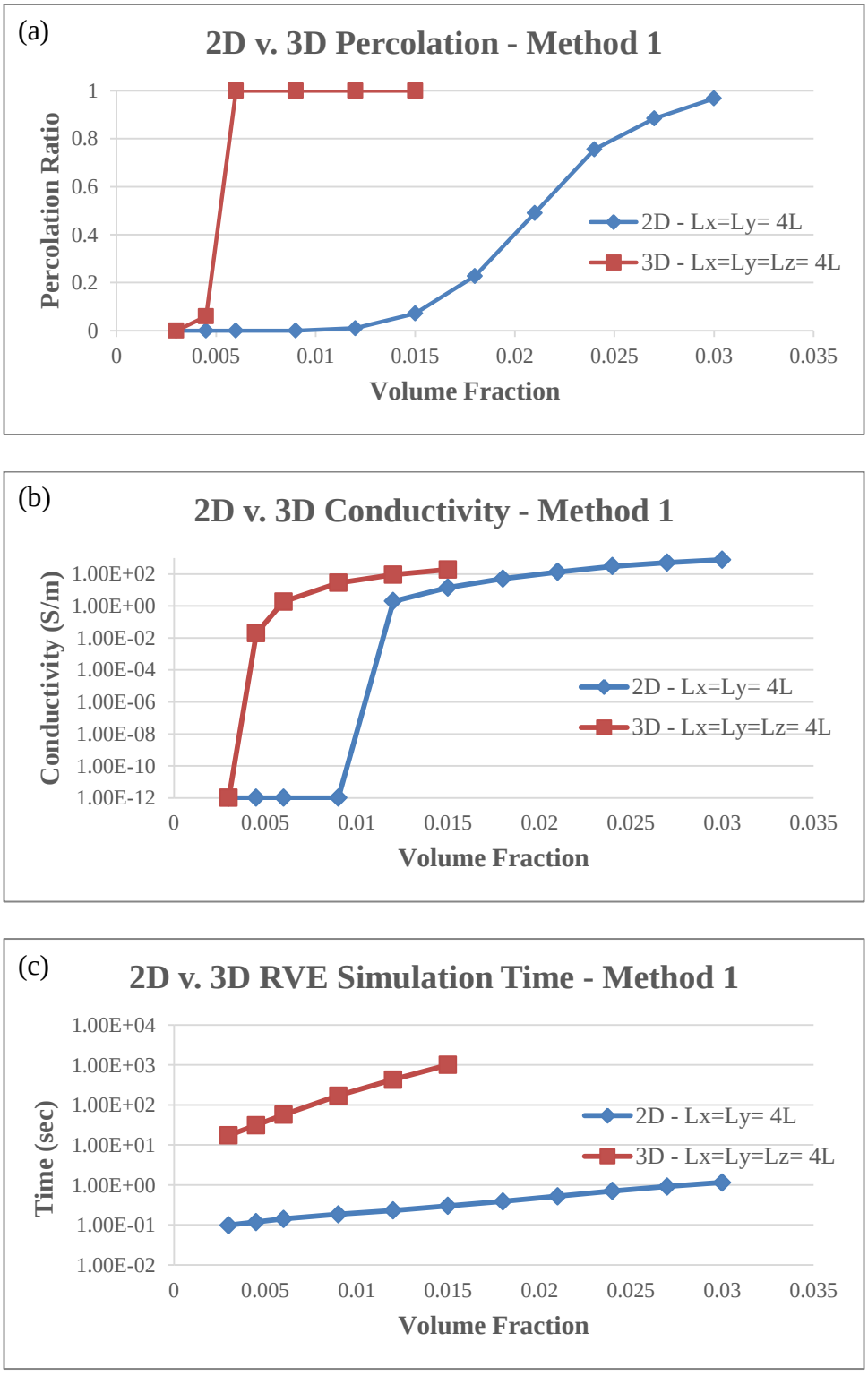

Figure 40. 2D and 3D Method 1 comparison. (a) Percolation ratio. (b) Effective electrical conductivity. (c) Average simulation time for each RVE. L corresponds to the length of each CNT.

It is clear from Figure 40 that there is a large discrepancy between the 2D and 3D models. The 3D RVEs have a sharp percolation threshold at around 0.5-0.6% volume fraction which corresponds to a significant increase in conductivity as the nanocomposite transfers from an insulator to a conductor. This is in good agreement with the study by Foygel et al. [36] which predicts a percolation threshold of 0.67% for rod fillers with an aspect ratio of 100. The 2D RVEs have a gradual increase in percolation ratio at much higher volume fractions; in fact, a 100% percent ratio is not even reached by 3% volume fraction. The conductivity of both models converges somewhat at higher volume fractions, but this is overshadowed by their stark differences at the lower volume fractions. The 3D model much more closely matches the reported percolation characteristics of CNT/polymer nanocomposites, such as a sharp increase in percolation ratio at a low volume fraction. Overall it represents a drastic improvement in nanocomposite modeling capability in comparison to the 2D model. The reason for this is that a more realistic representation is created when using 3D RVEs in comparison to 2D RVEs where all CNTs are restricted to a single plane with an arbitrary thickness.

Obviously, the 2D model does carry the advantage of shorter computation time. From observation of Figure 40 (c), it can be seen that there is an exponential increase in the computation time for the 3D models as the volume fraction increases. The situation is somewhat helped by the fact that fewer RVEs are generated for the 3D model, but the computation time can still grow to be unmanageable quickly.

It has been postulated that producing periodic boundary conditions using the cut-and-relocate method, as used in Method 1, leads to bias on the location of CNTs at boundaries and therefore over-predict the overall effective conductivity [59]. That claim

is tested here by using Method 2 as described in Chapter 4 to create RVEs with non-periodic boundary conditions. Figure 41 shows the comparison between the effective conductivity calculated for 3D RVEs generated using both methods. The parameters in Table 2 are used here to limit the effects of random parameters.

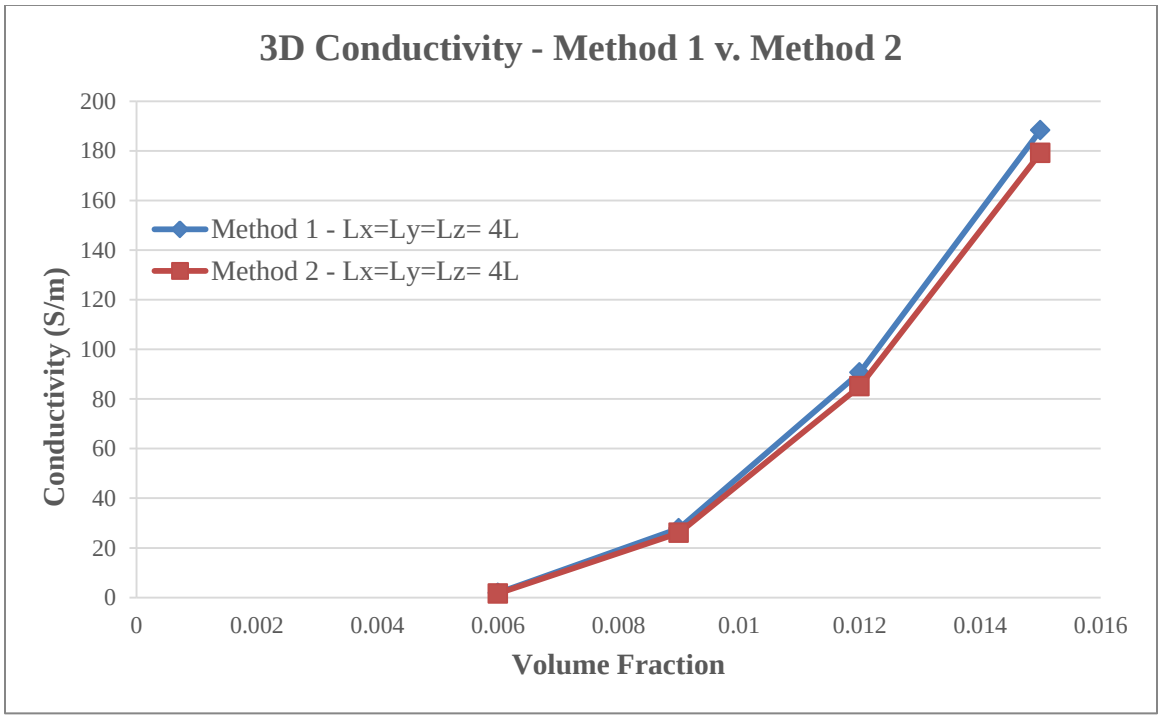

Figure 41. Method 1 and Method 2 effective conductivity comparison.

Figure 41 shows that the conductivity of RVEs created using Method 1 tend to be slightly higher than those of Method 2. This indicates that there is indeed some bias associated with the use of periodic boundary conditions, but that its effect is relatively minor. Therefore, the use of periodic boundary conditions is valid for use in both Method 1 and Method 3.

Before assessing the results for all the 3D model methods, the effect of varying the non-conducting dimension size for Method 4 will be tested using a 2D model. Fang et al. [59] claimed that increasing the distance between the electrodes, or the conducting dimension distance, improved the accuracy of the conductivity estimate while varying the non-conducting dimension had essentially no effect. In the interest of computation time this claim will be verified using 2D models. Though it has been shown that the 2D models do not model the nanocomposites as well as 3D models, they still are able to show the general response when varying parameters. Figure 42 shows the effect of varying the non-conducting dimension, L_x, while Figure 43 shows the effect of varying the conducting dimension L_y.

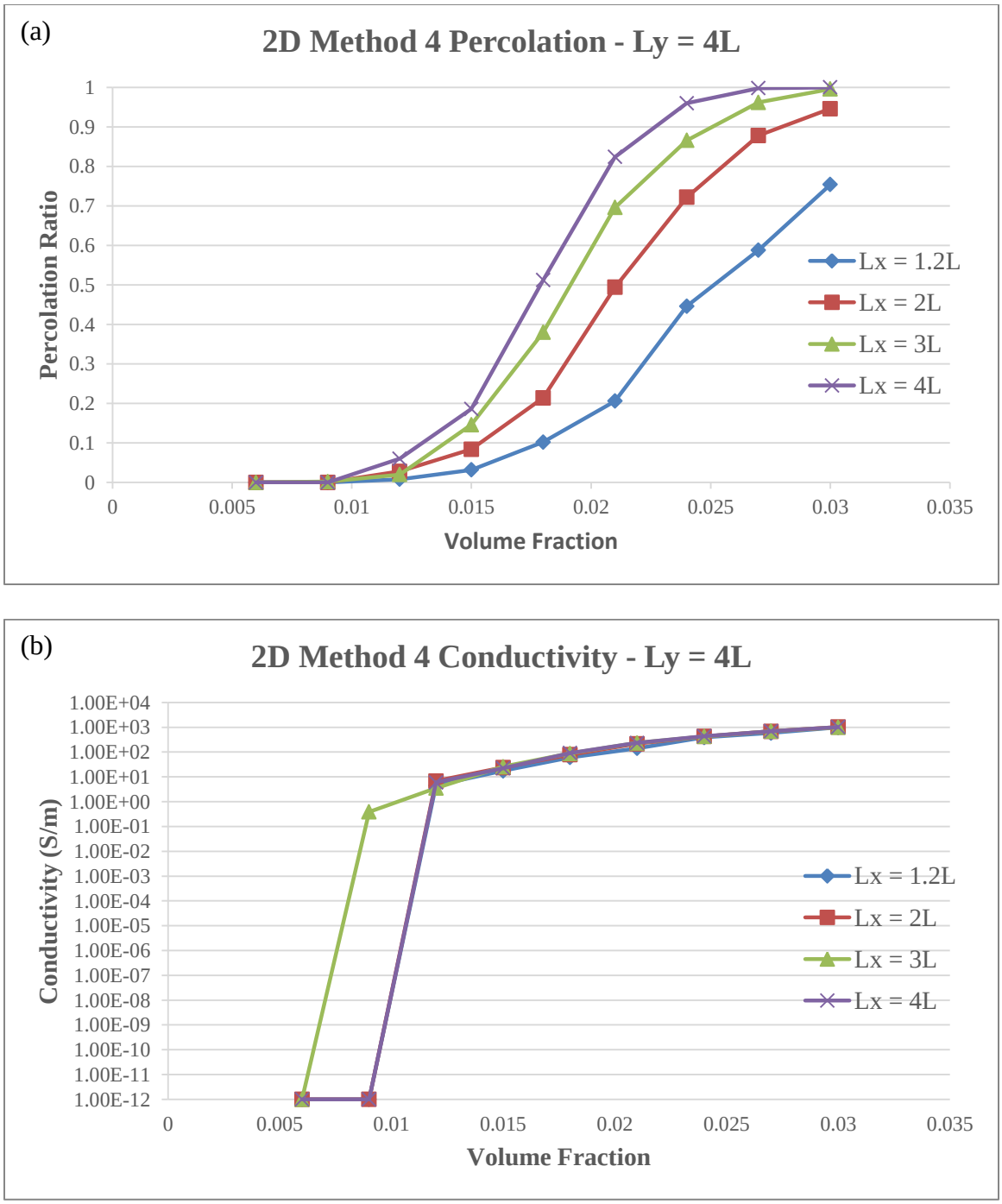

Figure 42. 2D-Method 4 with constant $L_y = 4L$. (a) Percolation ratio (for the large RVE). (b) Effective conductivity. It can be seen that even though the percolation ratio is quite different for each value of X, the conductivity remains relatively unchanged.

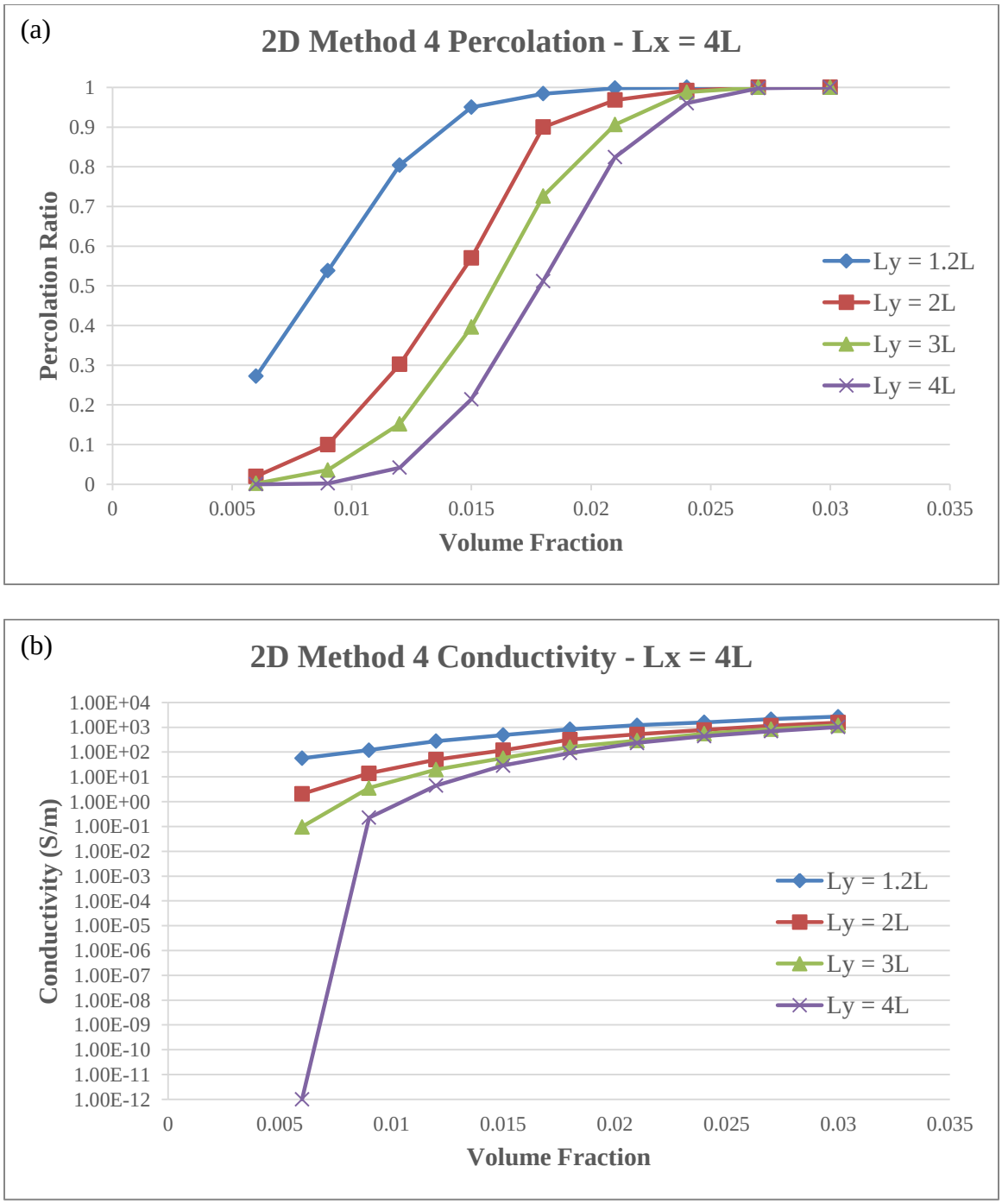

Figure 43. 2D-Method 4 with constant $L_x = 4L$. (a) Percolation ratio. (b) Effective conductivity. The conductivity is over-predicted at low Y-dimension values, showing that conductivity is dependent on the size of the conducting dimension.

Figure 42 shows that the effective conductivity is independent of the value of the non-conducting dimension, while Figure 43 shows that conductivity is dependent on the value of the conducting dimension. This verifies the postulate that for Method 4 the size of the non-conducting dimensions can be reduced and accurate results still obtained.

An interesting aspect of Figure 42 is that while the behavior of the percolation ratio of the large RVE is notably different for each value of L_x used, the effective conductivity remains relatively constant in each. This showcases the robustness of Method 4, and how it is capable of accurately accounting for additional conductance through the boundaries. Another item to note is the large jump in the conductivity in Figure 42 (b) for $L_x = 3L$ at 0.9% volume fraction. Though it appears there is a gross discrepancy here, it actually represents the freak occurrence of a single RVE out of 500 percolating. The result is an increase in the average conductivity by almost 12 orders of magnitude. This anomaly speaks to how drastically the formation of a CNT network increases the effective conductivity and forces consideration of both the percolation ratio and effective conductivity at each volume fraction to get the complete picture of what's happening at each volume fraction.

Finally, the convergence behavior of varying dimension size is examined for each of the methods described in Chapter 4. As stated previously, if RVE dimensions are too small then conductivity will be over-predicted. However, using too large of RVEs results in prohibitive computation times. Regardless of computation time the method must converge to accurate values to be of any use. The best overall method found here will be chosen for performing further simulations. The parameters from Table 2 are used so that variability due to stochastic parameters is limited.

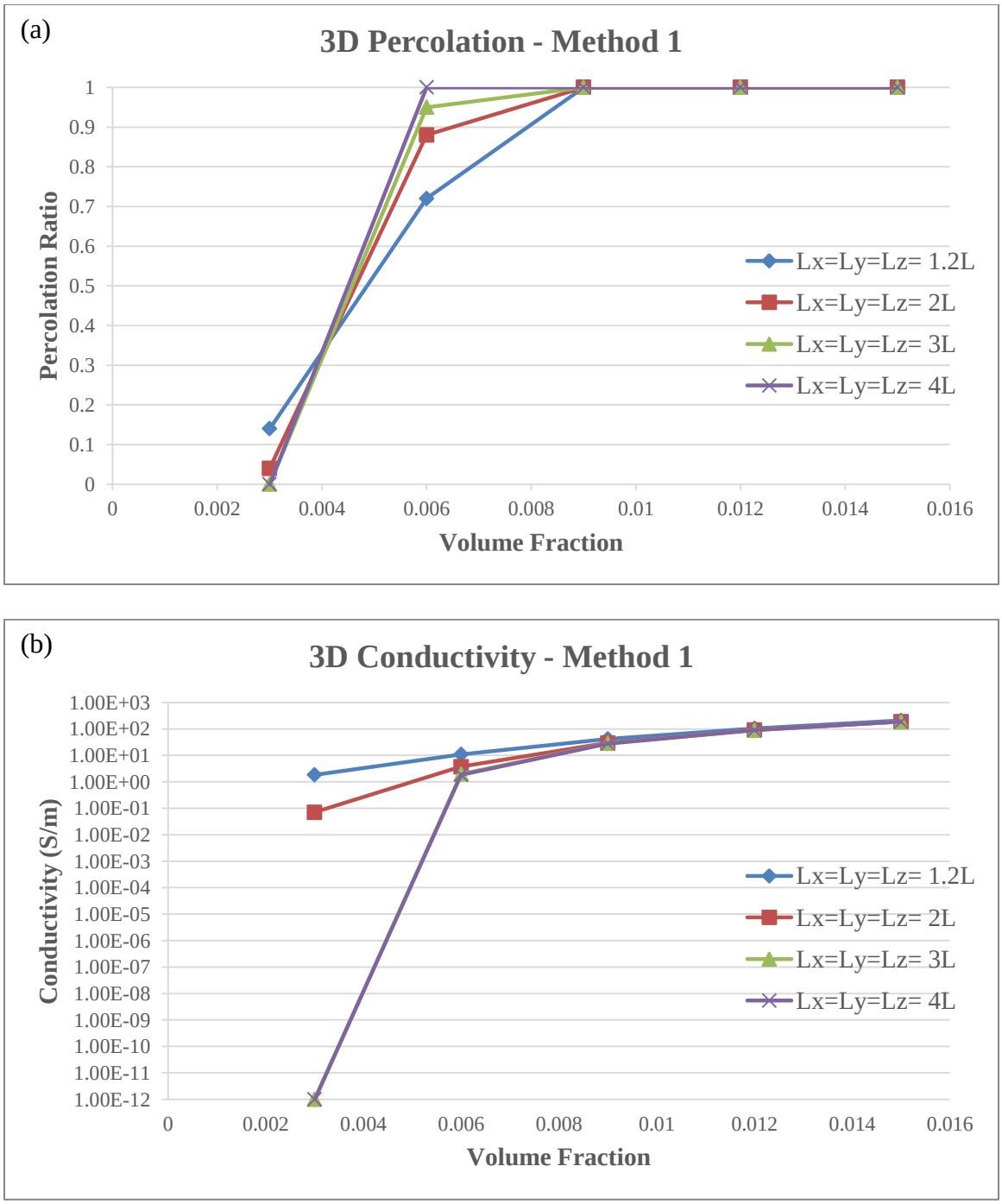

Figure 44. 3D-Method 1. (a) Percolation ratio. (b) Effective conductivity. Cubic RVEs with the dimensions all the same size are used.

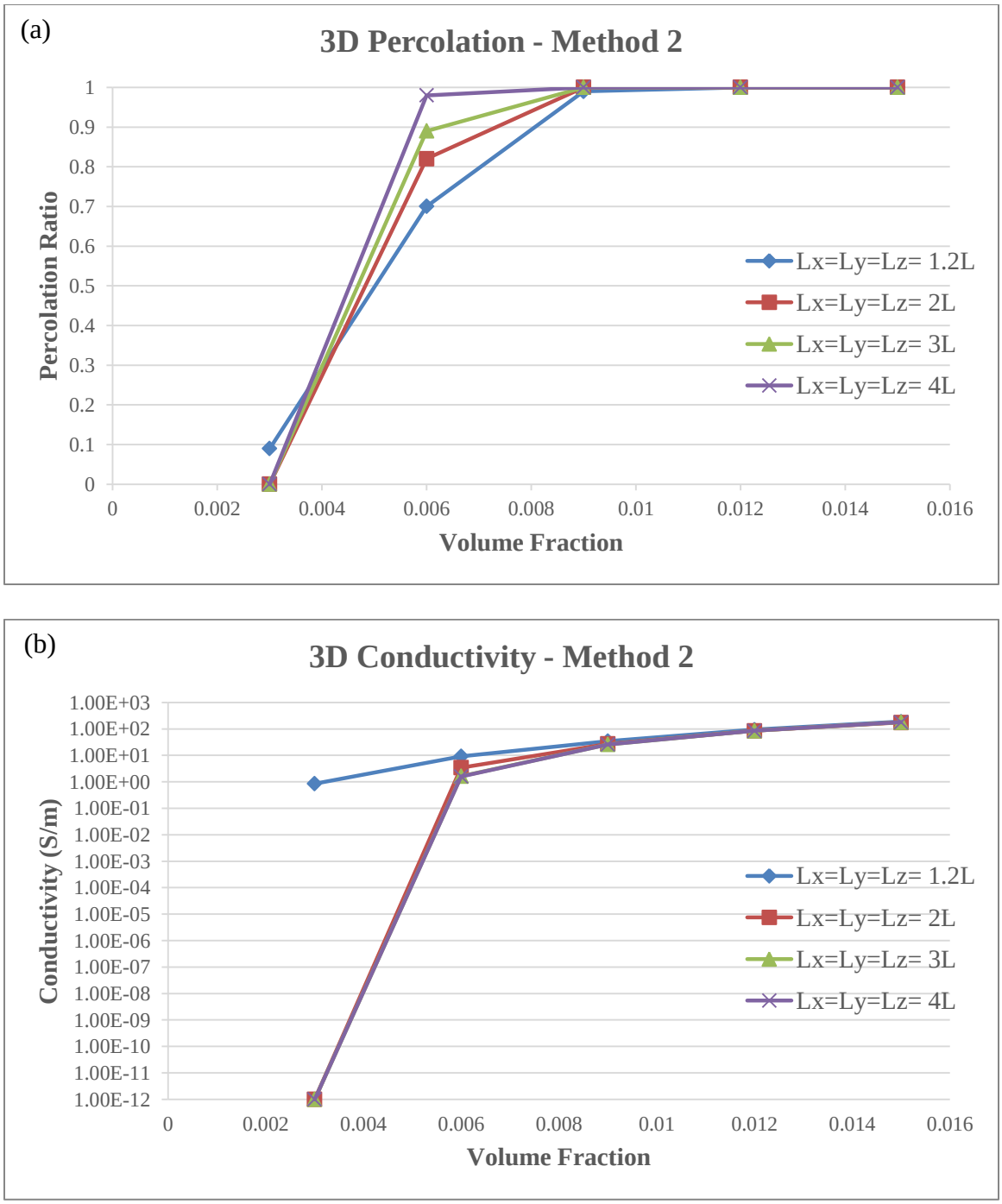

Figure 45. 3D-Method 2. (a) Percolation ratio. (b) Effective conductivity. Cubic RVEs with the dimensions all the same size are used.

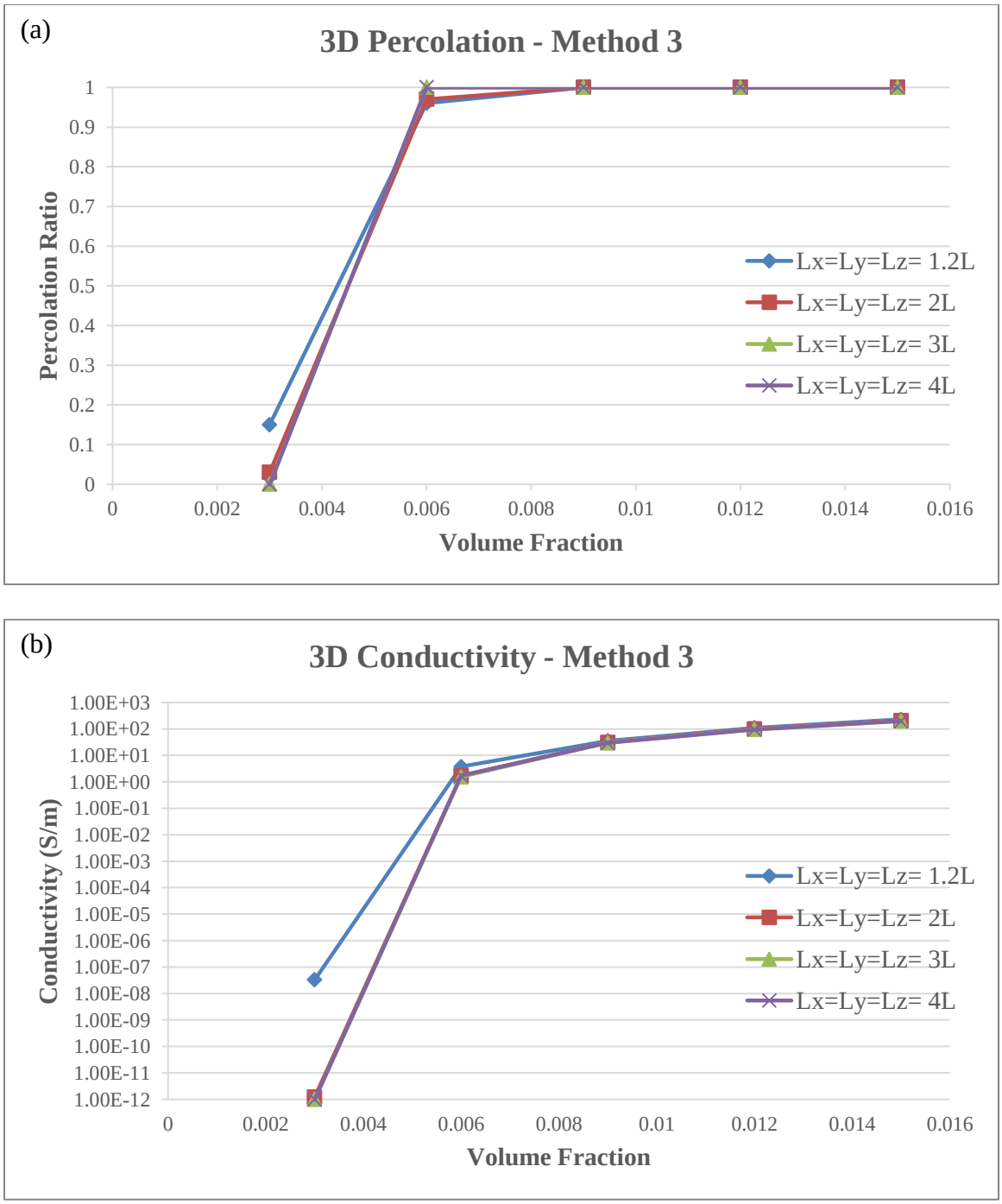

Figure 46. 3D-Method 3. (a) Percolation ratio. (b) Effective conductivity. Cubic RVEs with the dimensions all the same size are used.

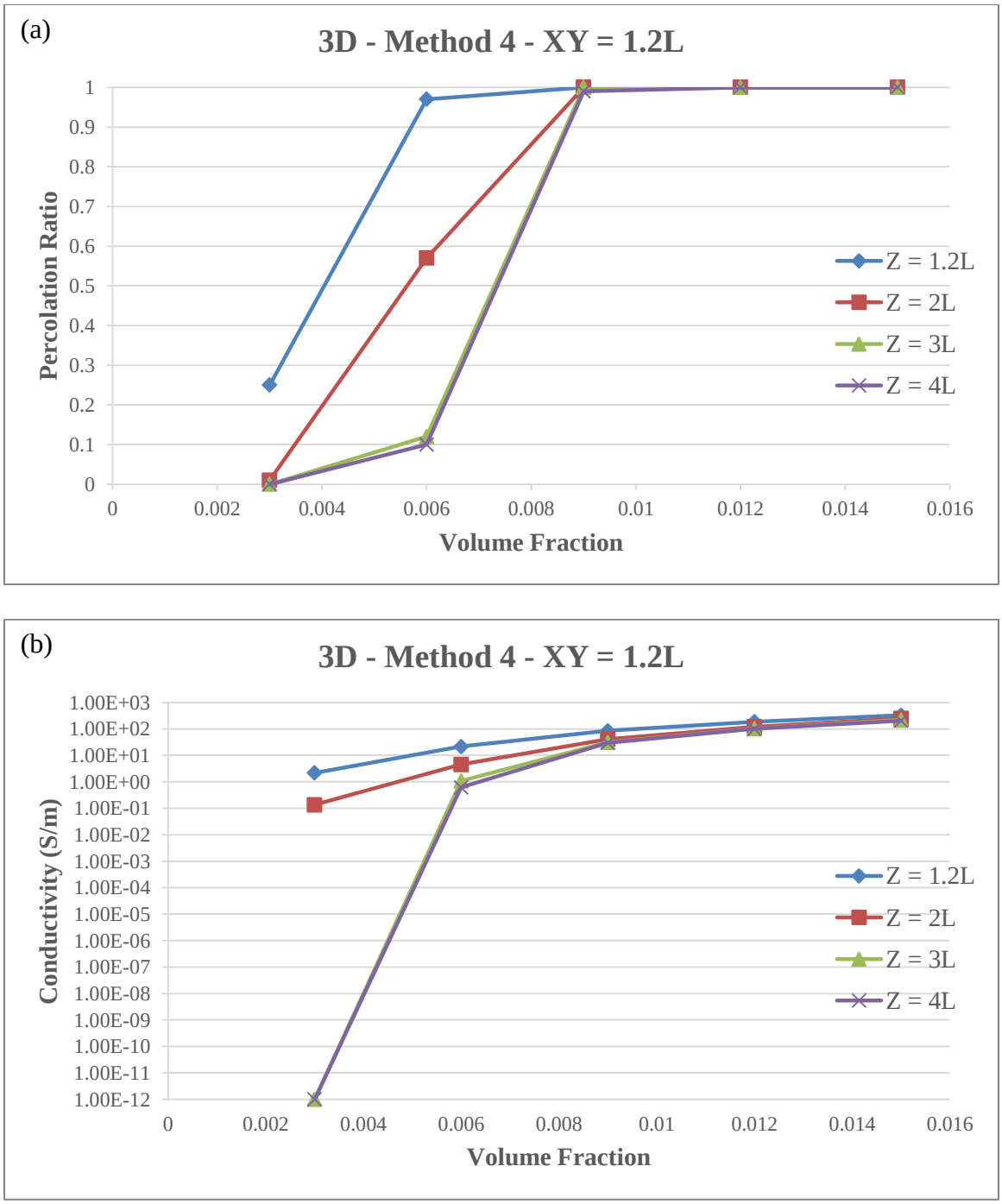

Figure 47. 3D-Method 4. (a) Percolation ratio (for the large RVE). (b) Effective conductivity. X and Y values are set at a constant 1.2L to reduce the overall volume since they have been shown to be independent of conductivity value.

Methods 1 and 2 show almost identical results. This is to be expected since it has been previously shown that periodic and non-periodic boundary conditions produce similar results. For these methods, conductivity is overestimated at lower RVE dimensions and percolation ratio is underestimated. Both seem to require the highest RVE dimension size, $L_x = L_y = L_z = 4L$, to produce accurate results for both percolation ratio and effective conductivity.

The conductivity predicted by Method 3 seems to be nearly independent of RVE dimension size. This holds true for the percolation ratio as well, something no other model is able to replicate. These results support the postulate that when using this method low RVE dimension sizes can be used and still generate accurate results. From these results it is determined that the dimensions of $L_x = L_y = L_z = 2L$ are sufficient to achieve good results for percolation ratio and effective conductivity.

The behavior of the effective conductivity from use of Method 4 matches those of the other methods, but there is vastly different behavior in the percolation ratio, especially around percolation threshold. Here the larger dimensions percolate less often, which is to be expected since there is a larger conducting distance for the network to traverse and shorter distances in the non-conducting dimensions for the network to maneuver. Yet the conductivity predicted for this data point is in the same vicinity as that predicted via the other three methods. Results are seen to have converged at the $L_z = 3L$ RVE dimension size with non-conducting dimensions of $L_x = L_y = 1.2L$. An overview of the effective conductivity and average simulation time for each of the methods at the selected RVE dimension sizes is shown in Figure 48.

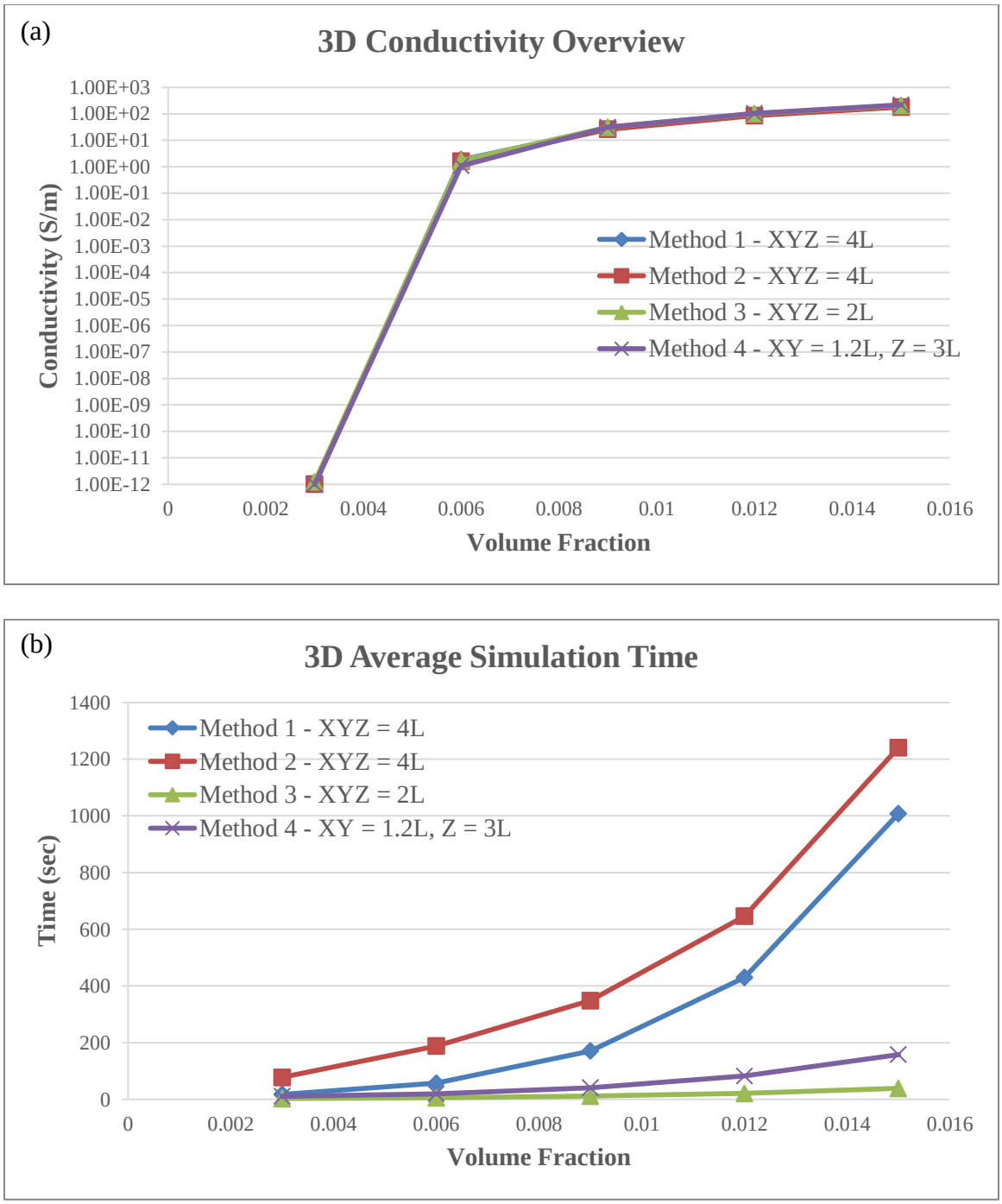

Figure 48. 3D Methods at chosen RVE sizes. (a) Effective conductivity. (b) Average simulation time per RVE. The effective conductivity predicted using each of the methods is nearly indistinguishable.

Figure 48 (a) shows that each of the four methods predicts nearly the same results for effective conductivity at each volume fraction. However, the computation time varies significantly. The large cubic RVEs employed in Method 1 has a large computation time of about 1,000 seconds for a single RVE at a volume fraction of 1.5% using an Intel Core i5 laptop. Method 2 is even worse because of the need to generate CNTS in a larger volume initially and then partition them to create the RVE. Methods 3 and 4 are able to reduce this computation time significantly by decreasing the RVE size necessary to obtain accurate results. Method 4 still takes slightly more time since three different networks must be solved during each simulation. Considering that the conductivity results are identical for each method, the choice for best method comes down to which has the lowest computation cost. That renders Method 3 with cubic dimensions $L_x = L_y = L_z = 2L$ as the most efficient method for simulating 3D nanocomposite transport properties. These parameters are used for the remainder of this thesis.

5.3 Electrical Modeling Results

Once an accurate and efficient modeling method has been selected it is logical to incorporate stochastic parameters into the model and compare to experimental results to verify that the proposed model is capable of simulating actual CNT/polymer nanocomposites. The electrical transport properties are studied first. The SWNT length Weibull distribution as described in Chapter 2 and temperature-dependent contact resistance distribution from Chapter 3 are next introduced into the model. A list of all parameters used in calculating electrical transport is given in Table 4.

INPUTS		
Average CNT length	500	nm
CNT diameter	5	nm
Average aspect ratio	100	
CNT conductivity	1E+06	S/m
Matrix conductivity	1E-12	S/m
Contact resistance	(stochastic)	Ω
Number of RVEs	100	
RVE dimension length	1,000	nm
Average max waviness	π/4	Radians
Applied potential (Top)	100	V
Applied potential (Bottom)	0	V

Table 4. SWNT nanocomposite electrical transport parameters.

An intrinsic conductivity of 10^6 S/m is chosen so that it is in the middle of the commonly reported range of conductivities for SWNTs [9], [10]. Section 3.2 described the temperature-dependent contact resistance distribution and gave parameters for metallic SWNT chiralities of (6,6), (8,8), (10,10), and (12,12) in Table 1. Nanotubes tend to vibrate more as the temperature increases, varying the atomic distance between connected CNTs. This in turn lowers the contact resistance since the electron density profiles intersect more, creating a higher overall conductivity. Smaller diameter nanotubes also tend to have a lower contact resistance because the electron density profile extends further out in them. The temperature dependency of nanocomposite conductivity using each type of filler is shown in Figure 49.

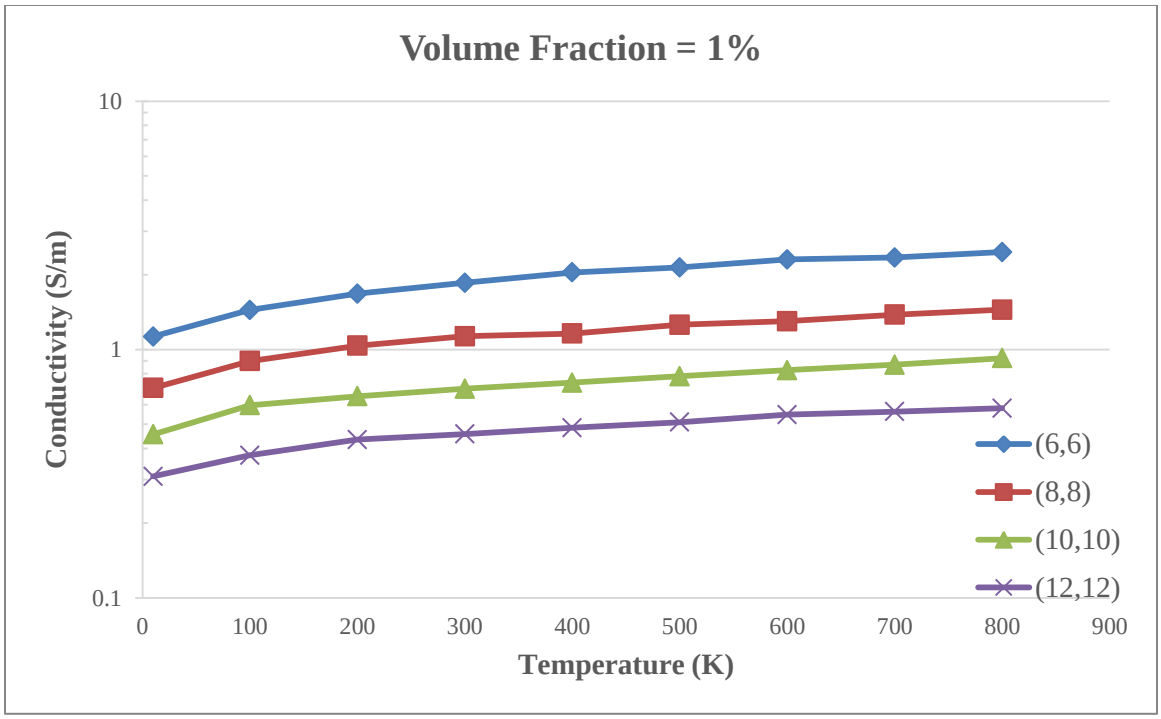

Figure 49. Temperature-dependent conductivity for different CNT chiralities. All simulations are ran at 1% volume fraction of CNT filler.

Figure 49 shows that an increase in temperature leads to an increase in effective conductivity. However, CNT chirality also is important when determining the nanocomposite conductivity. Note that the same value for diameter was used for each of these simulations for simplicity and to mitigate the variability due to using different aspect ratio CNTs. If different length or diameter values were desired, the model could easily accommodate these changes.

Percolated composite materials have been known to follow a power law [40] of the form

$$\sigma_{eff} = \sigma_0 (p - p_c)^t. \quad \textbf{(41)}$$

Here p is the CNT volume fraction, p_c is the percolation threshold, σ_0 is a coefficient that depends on nanotube conductivity, and t is the critical exponent. The percolation threshold is determined from observation of the model and σ_0 and t are found from fitting a sufficient number of simulated points to Equation (41). This allows for the calculation of effective conductivity at any desired volume fraction in the percolation region. A percolation threshold of 0.5% is selected here based on results from Figure 46. The process of calculating the coefficient and critical exponent is shown in Figure 50 for a (10,10) CNT nanocomposite at 300 K.

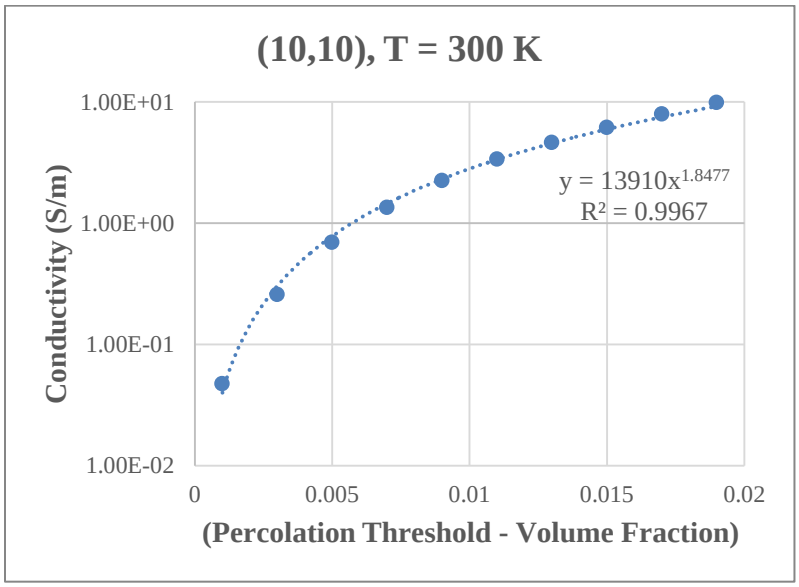

Figure 50. Power law fit to simulated data points for CNT chirality (10,10) at T = 300 K.

The critical exponent and coefficient are 1.85 and 1.39 x 10^4 respectively. This shows a quite good fit with an R^2 value of 0.9967. It is important to note that this power law can only be used at volume fractions above the percolation threshold. This process is repeated for the (6,6), (8,8), (10,10) and (12,12) CNT chiralities at temperatures of 50 K, 300 K,

600 K, and 1,000 K. For each case simulations were performed from 0.2% - 2.4% volume fraction at intervals of 0.2%. The resulting power law parameters are given in Table 5.

CNT Chirality – Temperature	σ_{Eff} (S/m) 2% VF	σ_0	t	R^2
(6,6) – T = 50 K	11.47	2.81E+04	1.87	0.9989
(6,6) – T = 300 K	16.68	4.76 E+04	1.90	0.9986
(6,6) – T = 600 K	20.54	7.71 E+04	1.96	0.9997
(6,6) – T = 1000 K	24.64	7.41 E+04	1.92	0.9985
(8,8) – T = 50 K	7.01	2.11 E+04	1.91	0.9994
(8,8) – T = 300 K	9.81	2.49 E+04	1.87	0.9976
(8,8) – T = 600 K	11.81	3.20 E+04	1.89	0.9981
(8,8) – T = 1000 K	14.11	4.05 E+04	1.90	0.9977
(10,10) – T = 50 K	4.60	1.09 E+04	1.86	0.9978
(10,10) – T = 300 K	6.17	1.39 E+04	1.85	0.9967
(10,10) – T = 600 K	7.40	2.05 E+04	1.89	0.9988
(10,10) – T = 1000 K	8.85	3.04 E+04	1.94	0.9993
(12,12) – T = 50 K	3.05	9.15 E+03	1.91	0.9992
(12,12) – T = 300 K	4.01	9.29 E+03	1.85	0.997
(12,12) – T = 600 K	4.76	1.58 E+03	1.93	0.9997
(12,12) – T = 1000 K	5.54	1.92 E+03	1.94	0.9997

Table 5. Parameters for power law fitting for electrical conductivity.

All the critical exponent values remain in the range of 1.8 – 2.0. This corresponds well to the accepted range of 1.6 – 2.0 predicted by other 3D percolation models [40], [55]–[59].

Finally, comparisons to experimental data are presented. A review of several different experimental studies on the electrical conductivity of CNT/polymer nanocomposites was conducted. The studies from Hu et al. [87], Ono et al. [88], Nano Carbon Technologies Co. [89], and Krause et al. [90] were chosen for comparison because of their numerous citations in other works. The results are shown in Figure 51.

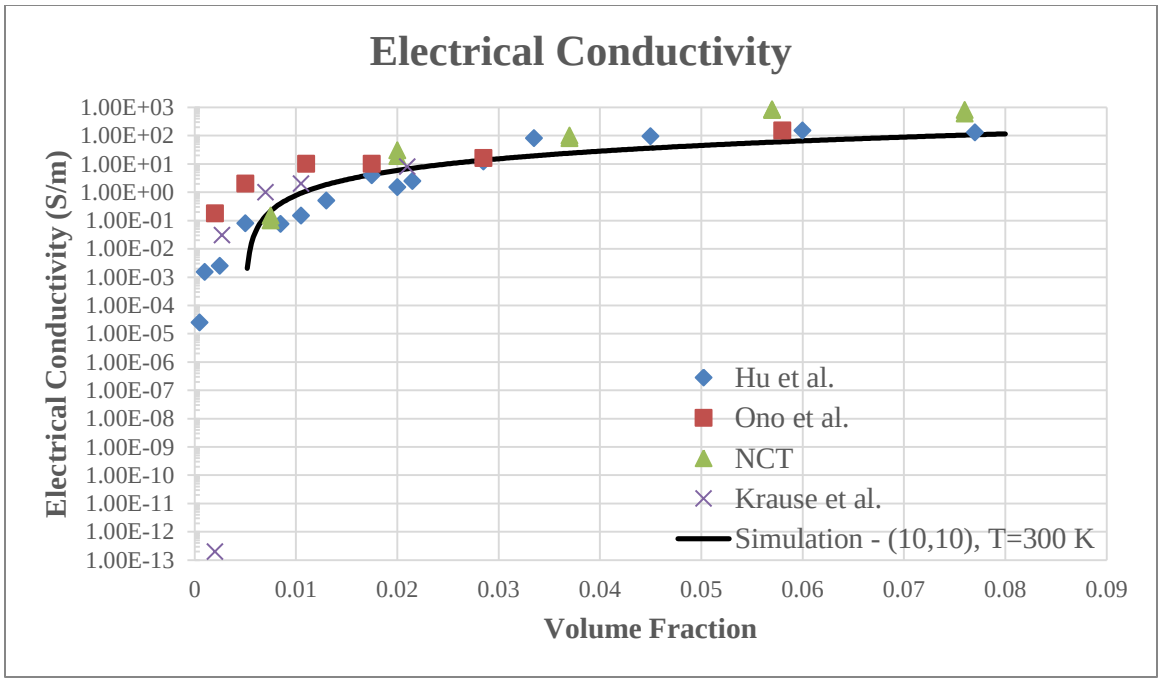

Figure 51. Comparison of experimental electical conductivity data to simulated data from the proposed model.

The simulated results for the (10,10) chirality case at 300 K are used since they lie somewhat in the middle of the conductivity range for all cases. The simulated results are for the most part in excellent agreement with the experimental data. The model is able to capture the sharp increase in conductivity once the percolation threshold is reached, followed by the more modest linear increase as the volume fraction is increased further beyond the threshold. The experimental data show that percolation may be occurring at lower volume fractions than what is predicted by the model, but this is most likely due to the type of CNTs used for each study. The use of a power law fit allows for easy calculation of the conductivity at higher volume fractions which would otherwise require significant computation time. Overall, the ability of the model to simulate the electrical conductivity of CNT/polymer nanocomposites has been verified.

5.4 Thermal Modeling Results

The ability of the model to simulate nanocomposite thermal conductivity will now be examined. Experimental studies have shown that the thermal properties of polymers are much less enhanced due to the addition of CNTs in comparison to the electrical properties [91]. This is due in large part to the high interfacial thermal resistance between CNTs and the polymer matrix. In this model it is assumed that this interfacial resistance is effectively insulating so that no heat transfer occurs between CNTs and the polymer. Therefore, the heat transfer of the CNT spanning network and polymer matrix will be considered separately and combined to determine the overall thermal conductivity, as detailed in Section 3.3. A list of model parameters used for the thermal study is given in Table 5. The Weibull distribution given in Section 2.1 is used to find the length and maximum waviness angle.

INPUTS		
Average CNT length	500	nm
CNT diameter	5	nm
Average aspect ratio	100	
CNT conductivity	6000	W/mK
Matrix conductivity	0.3	W/mK
Contact resistance	(variable)	K/W
Number of RVEs	100	
RVE dimension length	1,000	nm
Average max waviness	$\pi/4$	Radians
Applied temperature (Top)	100	K
Applied temperature (Bottom)	0	K

Table 6. SWNT nanocomposite heat transport parameters.

In comparison to the electrical transport properties in Table 3, the ratio between CNT conductivity and matrix conductivity is much lower. This means that when percolation occurs, there will be a much less significant jump in the thermal conductivity as compared to the electrical conductivity. The thermal conductance of the CNT network is highly dependent on the contact resistance of crossing nanotubes. Section 3.1 described some of the experimentally determined values for this contact resistance, ranging from 10^7 – 10^{10} K/W [36], [83]. The thermal conductivity of nanocomposites with contact resistances set within this range is shown in Figure 52 and the ratio of heat transfer due to the polymer matrix for each case is shown in Figure 53.

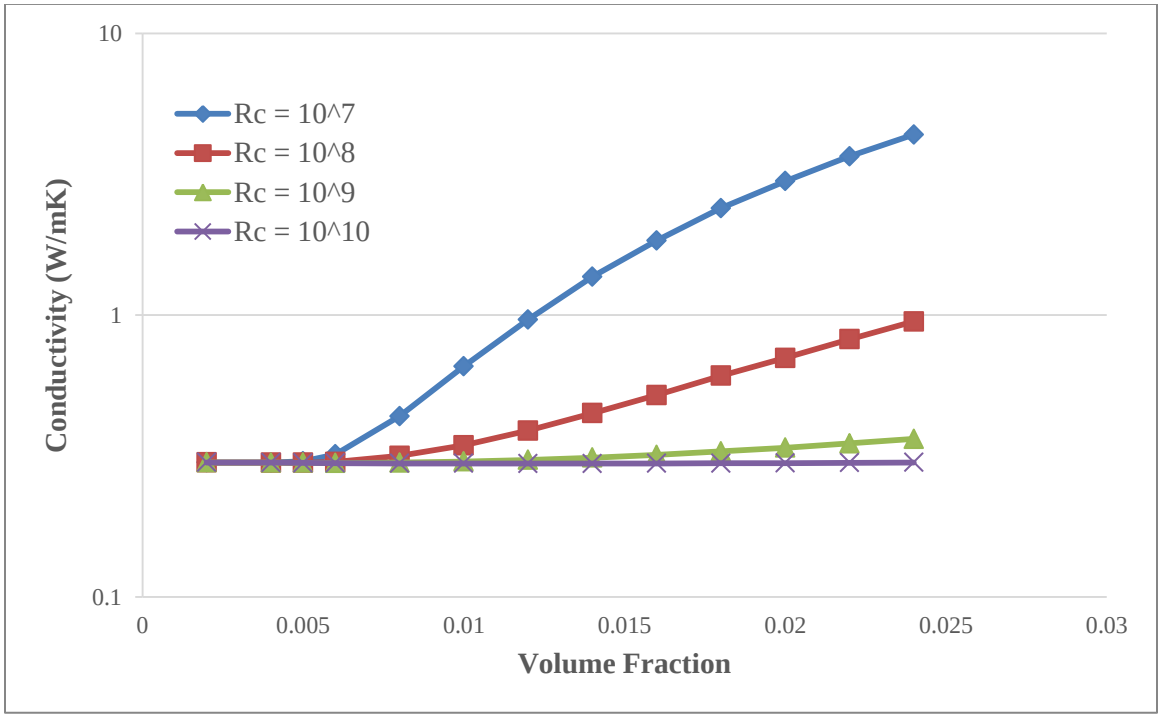

Figure 52. Thermal conductivity of nanocomposites with varying contact resistances and CNT filler volume fraction.

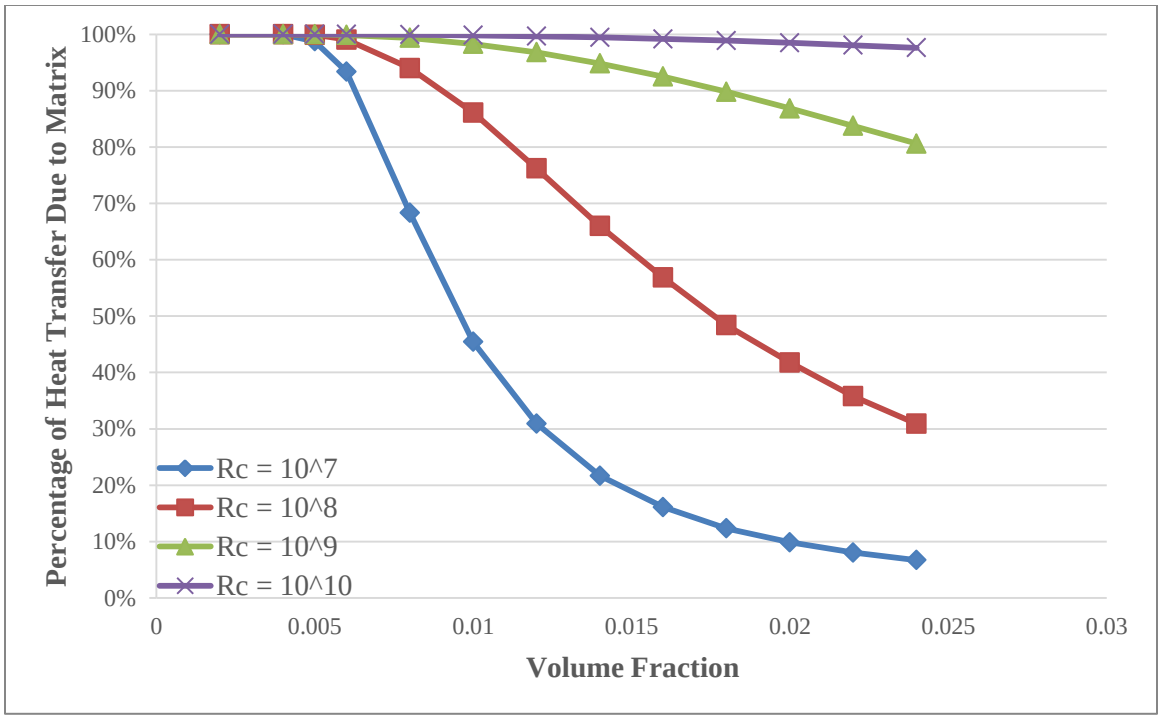

Figure 53. Percentage of heat transfer due to the polymer matrix for each case of CNT-CNT contact resistance.

These figures show that low CNT contact resistances result in a significant improvement in overall thermal conductivity. However, the high contact resistances show little to no improvement in thermal conductivity and essentially all heat transfer occurs through the polymer matrix. In fact, the $R_c = 10^{10}$ K/W data series actually has a drop in conductivity. This has been observed before in the results of Moisala et al. [22] on the thermal conductivity of CNT/polymer nanocomposites. It is due to high fiber thermal resistances, and the fact that there is less connected polymer material available to conduct heat as the volume fraction of filler increases. The percolation threshold remains at 0.5% volume fraction, the same as in the electrical case. This is to be expected because the RVE geometry generation and spanning network algorithm are the exact same for both.

Once this is reached, more and more heat transfer is taken through the CNT network as the volume fraction is increased.

A percolation power law in the form of Equation (41) can also be fit to the thermal conductivity data. However, the thermal conductivity of the matrix must be subtracted from the effective conductivity so that only the increase in conductivity due to the percolated network of CNTs is taken into account. The parameters for the first three sets of data are given in Table 7. Since the $R_c = 10^{10}$ experiences a decrease in conductivity, a power law was not fit to that data.

Contact Resistance	σ_{Eff} **(W/mK) 2% VF**	σ_0	**t**	$\mathbf{R^2}$
$R_c = 10^7$	2.9884	5.47 E+03	1.82	0.9998
$R_c = 10^8$	0.7046	3.34 E+03	2.14	0.997
$R_c = 10^9$	0.3385	1.32 E+03	2.49	0.9944

Table 7. Parameters for power law fitting for thermal conductivity.

The values of the critical exponent start to diverge from the range seen in Table 5 for the higher contact resistance nanocomposites. This is most likely due to the fact that percolation behavior becomes less evident due to the higher resistances encountered in these data sets. This issue aside, they are still able to predict the conductivity at any volume fraction within the percolation region using the created percolation power laws.

The thermal transport model must now be compared to experimental data to assess how effectively the model can represents real nanocomposite materials. Studies from Hong and Tai [23], King et al. [92], and Guthy et al. [93] were chosen to give a wide range of experimental data. Each of these uses a different polymer as the matrix material. Therefore, the non-dimensional ratio of nanocomposite conductivity over pure

polymer conductivity is used so that effective comparisons can be made. Three different sets of simulated data series have been included so that it can be determined which best matches the experimental data. The results are shown in Figure 54.

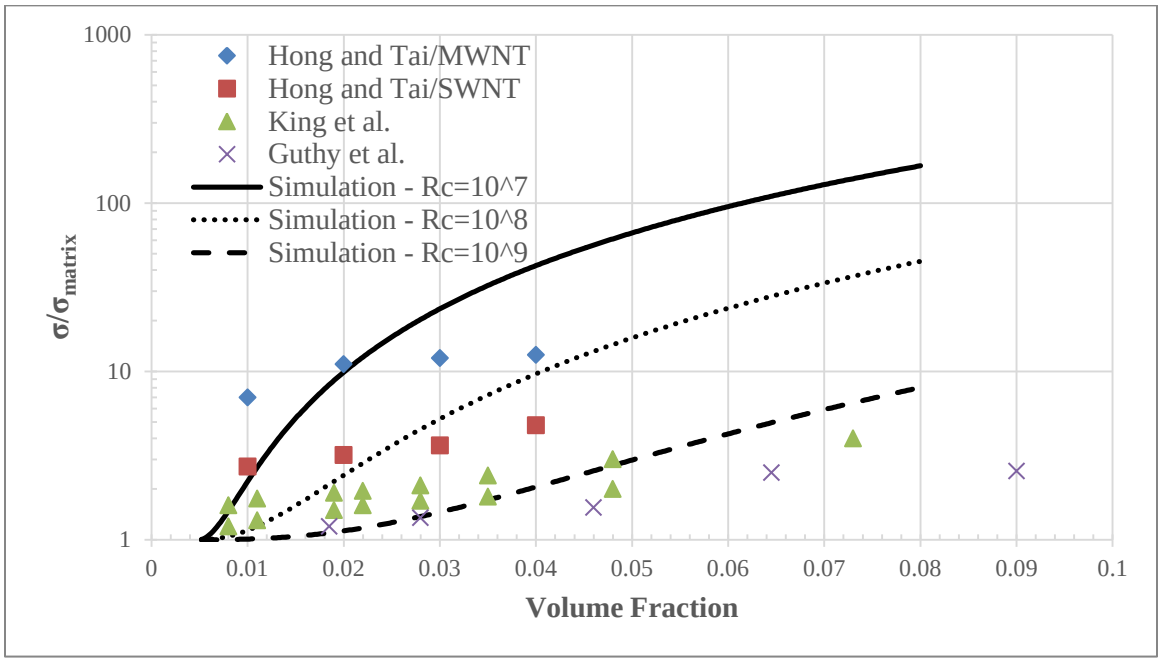

Figure 54. Comparison of experimental thermal conductivity data to simulated data from the proposed model.

Notably, the thermal transport model does not match the experimental data as well as the electrical case. The $R_c = 10^7$ data series fits the higher experimental values of Hong and Tai up to 2% volume fraction and then overshoots them. Nanocomposites created with $R_c = 10^8$ fare a little better in matching the Hong and Tai data points. Setting $R_c = 10^9$ matches the lower experimental values of King et al. and Guthy et al, though it seems that these systems tend to percolate sooner and increase less over time. Overall, the choices of $R_c = 10^8$ and $R_c = 10^9$ result in the best agreement with experimental data.

Chapter 6

Concluding Remarks

The exceptional properties of carbon nanotubes have led to widespread research efforts on how to characterize these materials and create useful devices from them. Experiments on carbon nanotube based polymer composites are time consuming and expensive. To alleviate these costs, there is a great need for numerical models that are adaptable enough to model various types of carbon nanotube and polymer combinations. While the electrical conductivity of nanocomposite materials has received significant attention, much less work has been done on predicting thermal transport properties. The model presented in this thesis has addressed this need with a reliable, versatile, and accurate method for predicting nanocomposite electrical and thermal properties.

The presented model uses Monte Carlo simulations, a spanning network algorithm, and a resistor network model to characterize both the electrical and thermal transport within a nanocomposite. The use of Monte Carlo simulations reduces the variability associated with the random generation of nanostructures. The spanning network algorithm starts at the top of the structure and systematically searches for connections and a percolating network that reaches the bottom of the representative

volume element. The resistor network method converts a spanning network into a series of linear resistors using Kirchoff's current law in the electrical case and Fourier's law in the thermal case. The entire system is then solved through finite element analysis and post-processing is done to find the backbone and effective conductivity of the material.

The proposed model builds upon previous work done at Rice University where the electrical conductivity of two-dimensional nanocomposite models was predicted. It was shown in this work that these two-dimensional models are inadequate for predicting the material properties. Three-dimensional models have been created that more accurately represent nanocomposite systems. Different methods of generating these systems were explored to find a method that was able to reduce the required computation time while still providing accurate results.

The main advantage of the presented model is its extreme versatility. There are several different parameters within the model that can be altered so that a potential analyst can simulate the exact nanocomposite desired. This is true for both the electrical and thermal case, where the latter has a much stronger dependency on the properties of the polymer matrix. Another advantage of the model is the excellent visualizations of the generated nanocomposites where the geometry, nodal temperatures and voltages, and element currents and heat fluxes can be observed. An additional advantage of the model is the ability to predict the backbone where the majority of the electric current or heat flux can occur through the percolated nanotube network.

In closure, the model presented in this thesis has provided valuable insight and accurate predictions of the electrical and thermal performance of nanocomposite materials. It has been shown that it is capable of modeling electrical and thermal transport

at both the microscale and macroscale. A method of solution has been incorporated that predicts accurate results in a timely manner. This model provides a tool to correlate with experimental results and predict the performance of new materials. The presented work expands the current boundaries on nanocomposite modeling capability developed by Rice University.

There are a number of options for future research related to this work. The first can involve a deeper look into the thermal parameters to be used in the model and possible incorporation of interfacial thermal resistance between CNTs and the polymer so that heat can transfer between the two. The effects of nanotube agglomeration and alignment could be incorporated within the model. A coupled analysis where a large deformation is applied to the system which changes the spanning network could also be developed to determine the effects on electrical and thermal conductivity. More efficient methods can be utilized for use in the spanning network algorithm in order to lower the computation cost. Finally, the model can be modified to include both metallic and semiconducting nanotubes.

References

[1] S. Iijima, "Helical microtubules of graphitic carbon," *Nature*, vol. 354, no. 6348, pp. 56–58, Nov. 1991.

[2] T. Natsuki, K. Tantrakarn, and M. Endo, "Prediction of elastic properties for single-walled carbon nanotubes," *Carbon*, vol. 42, no. 1, pp. 39–45, 2004.

[3] M. Meo and M. Rossi, "A molecular-mechanics based finite element model for strength prediction of single wall carbon nanotubes," *Materials Science and Engineering: A*, vol. 454–455, pp. 170–177, Apr. 2007.

[4] K. I. Tserpes, P. Papanikos, and S. A. Tsirkas, "A progressive fracture model for carbon nanotubes," *Composites Part B: Engineering*, vol. 37, no. 7–8, pp. 662–669, Oct. 2006.

[5] T. Belytschko, S. P. Xiao, G. C. Schatz, and R. S. Ruoff, "Atomistic simulations of nanotube fracture," *Phys. Rev. B*, vol. 65, no. 23, p. 235430, Jun. 2002.

[6] A. V. Desai and M. A. Haque, "Mechanics of the interface for carbon nanotube–polymer composites," *Thin-Walled Structures*, vol. 43, no. 11, pp. 1787–1803, Nov. 2005.

[7] S. Berber, Y.-K. Kwon, and D. Tománek, "Unusually High Thermal Conductivity of Carbon Nanotubes," *Phys. Rev. Lett.*, vol. 84, no. 20, pp. 4613–4616, May 2000.

[8] L. Lindsay, D. A. Broido, and N. Mingo, "Lattice thermal conductivity of single-walled carbon nanotubes: Beyond the relaxation time approximation and phonon-phonon scattering selection rules," *Phys. Rev. B*, vol. 80, no. 12, p. 125407, Sep. 2009.

[9] T. W. Ebbesen, H. J. Lezec, H. Hiura, J. W. Bennett, H. F. Ghaemi, and T. Thio, "Electrical conductivity of individual carbon nanotubes," *Nature*, vol. 382, no. 6586, pp. 54–56, Jul. 1996.

[10] J. E. Fischer *et al.*, "Metallic resistivity in crystalline ropes of single-wall carbon nanotubes," *Phys. Rev. B*, vol. 55, no. 8, pp. R4921–R4924, Feb. 1997.

[11] B. Q. Wei, R. Vajtai, and P. M. Ajayan, "Reliability and current carrying capacity of carbon nanotubes," *Applied Physics Letters*, vol. 79, no. 8, pp. 1172–1174, Aug. 2001.

[12] S. Frank, P. Poncharal, Z. L. Wang, and W. A. de Heer, "Carbon Nanotube Quantum Resistors," *Science*, vol. 280, no. 5370, pp. 1744–1746, Jun. 1998.

[13] H. Cebeci, R. G. de Villoria, A. J. Hart, and B. L. Wardle, "Multifunctional properties of high volume fraction aligned carbon nanotube polymer composites with controlled morphology," *Composites Science and Technology*, vol. 69, no. 15–16, pp. 2649–2656, Dec. 2009.

[14] P. M. Ajayan, O. Stephan, C. Colliex, and D. Trauth, "Aligned Carbon Nanotube Arrays Formed by Cutting a Polymer Resin—Nanotube Composite," *Science*, vol. 265, no. 5176, pp. 1212–1214, Aug. 1994.

[15] X. Li, J. Rong, and B. Wei, "Electrochemical Behavior of Single-Walled Carbon Nanotube Supercapacitors under Compressive Stress," *ACS Nano*, vol. 4, no. 10, pp. 6039–6049, Oct. 2010.

[16] C. Yu, C. Masarapu, J. Rong, B. Wei, and H. Jiang, “Stretchable Supercapacitors Based on Buckled Single-Walled Carbon-Nanotube Macrofilms,” *Adv. Mater.*, vol. 21, no. 47, pp. 4793–4797, Dec. 2009.
[17] V. Subramanian, H. Zhu, and B. Wei, “Synthesis and electrochemical characterizations of amorphous manganese oxide and single walled carbon nanotube composites as supercapacitor electrode materials,” *Electrochemistry Communications*, vol. 8, no. 5, pp. 827–832, May 2006.
[18] J. Gong and P. Yang, “Investigation on field emission properties of graphene–carbon nanotube composites,” *RSC Adv.*, vol. 4, no. 38, pp. 19622–19628, Apr. 2014.
[19] K. Takei *et al.*, “Nanowire active-matrix circuitry for low-voltage macroscale artificial skin,” *Nat Mater*, vol. 9, no. 10, pp. 821–826, Oct. 2010.
[20] J. Zhu, C.-M. Hsu, Z. Yu, S. Fan, and Y. Cui, “Nanodome Solar Cells with Efficient Light Management and Self-Cleaning,” *Nano Lett.*, vol. 10, no. 6, pp. 1979–1984, Jun. 2010.
[21] J. Gou, Y. Tang, F. Liang, Z. Zhao, D. Firsich, and J. Fielding, “Carbon nanofiber paper for lightning strike protection of composite materials,” *Composites Part B: Engineering*, vol. 41, no. 2, pp. 192–198, Mar. 2010.
[22] A. Moisala, Q. Li, I. A. Kinloch, and A. H. Windle, “Thermal and electrical conductivity of single- and multi-walled carbon nanotube-epoxy composites,” *Composites Science and Technology*, vol. 66, no. 10, pp. 1285–1288, Aug. 2006.
[23] W.-T. Hong and N.-H. Tai, “Investigations on the thermal conductivity of composites reinforced with carbon nanotubes,” *Diamond and Related Materials*, vol. 17, no. 7–10, pp. 1577–1581, Jul. 2008.
[24] Z. Spitalsky, D. Tasis, K. Papagelis, and C. Galiotis, “Carbon nanotube–polymer composites: Chemistry, processing, mechanical and electrical properties,” *Progress in Polymer Science*, vol. 35, no. 3, pp. 357–401, Mar. 2010.
[25] K. S. Novoselov *et al.*, “Electric Field Effect in Atomically Thin Carbon Films,” *Science*, vol. 306, no. 5696, pp. 666–669, Oct. 2004.
[26] R. Saito, M. Fujita, G. Dresselhaus, and M. S. Dresselhaus, “Electronic structure of chiral graphene tubules,” *Applied Physics Letters*, vol. 60, no. 18, pp. 2204–2206, May 1992.
[27] T. W. Odom, J.-L. Huang, P. Kim, and C. M. Lieber, “Structure and Electronic Properties of Carbon Nanotubes,” *J. Phys. Chem. B*, vol. 104, no. 13, pp. 2794–2809, Apr. 2000.
[28] “Single Walled-Double Walled Carbon Nanotubes,” *Cheap Tubes*. [Online]. Available: https://www.cheaptubes.com/product-category/single-walled-double-walled-carbon-nanotubes/. [Accessed: 20-Jan-2017].
[29] S. Shenogin, J. Lee, A. A. Voevodin, and A. K. Roy, “The effect of molecular mobility on electronic transport in carbon nanotube-polymer composites and networks,” *Journal of Applied Physics*, vol. 116, no. 23, p. 233704, Dec. 2014.
[30] Y. J. Kim, T. S. Shin, H. D. Choi, J. H. Kwon, Y.-C. Chung, and H. G. Yoon, “Electrical conductivity of chemically modified multiwalled carbon nanotube/epoxy composites,” *Carbon*, vol. 43, no. 1, pp. 23–30, 2005.

[31] J. Sandler, M. S. P. Shaffer, T. Prasse, W. Bauhofer, K. Schulte, and A. H. Windle, "Development of a dispersion process for carbon nanotubes in an epoxy matrix and the resulting electrical properties," *Polymer*, vol. 40, no. 21, pp. 5967–5971, Oct. 1999.
[32] C. Li and T.-W. Chou, "A direct electrifying algorithm for backbone identification," *J. Phys. A: Math. Theor.*, vol. 40, no. 49, p. 14679, 2007.
[33] F. Deng and Q.-S. Zheng, "An analytical model of effective electrical conductivity of carbon nanotube composites," *Applied Physics Letters*, vol. 92, no. 7, p. 071902, Feb. 2008.
[34] B.-W. Kim, S.-H. Park, R. S. Kapadia, and P. R. Bandaru, "Evidence of percolation related power law behavior in the thermal conductivity of nanotube/polymer composites," *Appl. Phys. Lett.*, vol. 102, no. 24, p. 243105, Jun. 2013.
[35] N. Shenogina, S. Shenogin, L. Xue, and P. Keblinski, "On the lack of thermal percolation in carbon nanotube composites," *Appl. Phys. Lett.*, vol. 87, no. 13, p. 133106, Sep. 2005.
[36] M. Foygel, R. D. Morris, D. Anez, S. French, and V. L. Sobolev, "Theoretical and computational studies of carbon nanotube composites and suspensions: Electrical and thermal conductivity," *Phys. Rev. B*, vol. 71, no. 10, p. 104201, Mar. 2005.
[37] C.-W. Nan, G. Liu, Y. Lin, and M. Li, "Interface effect on thermal conductivity of carbon nanotube composites," *Applied Physics Letters*, vol. 85, no. 16, pp. 3549–3551, Oct. 2004.
[38] B. J. Last and D. J. Thouless, "Percolation Theory and Electrical Conductivity," *Phys. Rev. Lett.*, vol. 27, no. 25, pp. 1719–1721, Dec. 1971.
[39] S. Kirkpatrick, "Classical Transport in Disordered Media: Scaling and Effective-Medium Theories," *Phys. Rev. Lett.*, vol. 27, no. 25, pp. 1722–1725, Dec. 1971.
[40] S. Kirkpatrick, "Percolation and Conduction," *Rev. Mod. Phys.*, vol. 45, no. 4, pp. 574–588, Oct. 1973.
[41] G. E. Pike and C. H. Seager, "Percolation and conductivity: A computer study. I," *Phys. Rev. B*, vol. 10, no. 4, pp. 1421–1434, Aug. 1974.
[42] I. Balberg, N. Binenbaum, and N. Wagner, "Percolation Thresholds in the Three-Dimensional Sticks System," *Phys. Rev. Lett.*, vol. 52, no. 17, pp. 1465–1468, Apr. 1984.
[43] A. Celzard, E. McRae, C. Deleuze, M. Dufort, G. Furdin, and J. F. Marêché, "Critical concentration in percolating systems containing a high-aspect-ratio filler," *Phys. Rev. B*, vol. 53, no. 10, pp. 6209–6214, Mar. 1996.
[44] D. S. McLachlan *et al.*, "AC and DC percolative conductivity of single wall carbon nanotube polymer composites," *J. Polym. Sci. B Polym. Phys.*, vol. 43, no. 22, pp. 3273–3287, Nov. 2005.
[45] G. D. Seidel and D. C. Lagoudas, "A Micromechanics Model for the Electrical Conductivity of Nanotube-Polymer Nanocomposites," *Journal of Composite Materials*, vol. 43, no. 9, pp. 917–941, May 2009.
[46] C. H. Seager and G. E. Pike, "Percolation and conductivity: A computer study. II," *Phys. Rev. B*, vol. 10, no. 4, pp. 1435–1446, Aug. 1974.

[47] W. S. Bao, S. A. Meguid, Z. H. Zhu, Y. Pan, and G. J. Weng, "Effect of carbon nanotube geometry upon tunneling assisted electrical network in nanocomposites," *Journal of Applied Physics*, vol. 113, no. 23, p. 234313, Jun. 2013.
[48] C. Li and T.-W. Chou, "Continuum percolation of nanocomposites with fillers of arbitrary shapes," *Applied Physics Letters*, vol. 90, no. 17, p. 174108, Apr. 2007.
[49] C. Li and T.-W. Chou, "Modeling of damage sensing in fiber composites using carbon nanotube networks," *Composites Science and Technology*, vol. 68, no. 15–16, pp. 3373–3379, Dec. 2008.
[50] C. Li and T.-W. Chou, "Electrical conductivities of composites with aligned carbon nanotubes," *J Nanosci Nanotechnol*, vol. 9, no. 4, pp. 2518–2524, Apr. 2009.
[51] C. Li, E. T. Thostenson, and T.-W. Chou, "Dominant role of tunneling resistance in the electrical conductivity of carbon nanotube–based composites," *Applied Physics Letters*, vol. 91, no. 22, p. 223114, Nov. 2007.
[52] C. Li, E. T. Thostenson, and T.-W. Chou, "Effect of nanotube waviness on the electrical conductivity of carbon nanotube-based composites," *Composites Science and Technology*, vol. 68, no. 6, pp. 1445–1452, May 2008.
[53] A. Behnam and A. Ural, "Computational study of geometry-dependent resistivity scaling in single-walled carbon nanotube films," *Phys. Rev. B*, vol. 75, no. 12, p. 125432, Mar. 2007.
[54] F. Dalmas, R. Dendievel, L. Chazeau, J.-Y. Cavaillé, and C. Gauthier, "Carbon nanotube-filled polymer composites. Numerical simulation of electrical conductivity in three-dimensional entangled fibrous networks," *Acta Materialia*, vol. 54, no. 11, pp. 2923–2931, Jun. 2006.
[55] H. M. Ma and X.-L. Gao, "A three-dimensional Monte Carlo model for electrically conductive polymer matrix composites filled with curved fibers," *Polymer*, vol. 49, no. 19, pp. 4230–4238, Sep. 2008.
[56] N. Hu, Z. Masuda, C. Yan, G. Yamamoto, H. Fukunaga, and T. Hashida, "The electrical properties of polymer nanocomposites with carbon nanotube fillers," *Nanotechnology*, vol. 19, no. 21, p. 215701, May 2008.
[57] D. A. Jack, C.-S. Yeh, Z. Liang, S. Li, J. G. Park, and J. C. Fielding, "Electrical conductivity modeling and experimental study of densely packed SWCNT networks," *Nanotechnology*, vol. 21, no. 19, p. 195703, 2010.
[58] W. S. Bao, S. A. Meguid, Z. H. Zhu, and M. J. Meguid, "Modeling electrical conductivities of nanocomposites with aligned carbon nanotubes," *Nanotechnology*, vol. 22, no. 48, p. 485704, 2011.
[59] W. Fang, H. W. Jang, and S. N. Leung, "Evaluation and modelling of electrically conductive polymer nanocomposites with carbon nanotube networks," *Composites Part B: Engineering*, vol. 83, pp. 184–193, Dec. 2015.
[60] E. S. Choi *et al.*, "Enhancement of thermal and electrical properties of carbon nanotube polymer composites by magnetic field processing," *Journal of Applied Physics*, vol. 94, no. 9, pp. 6034–6039, Oct. 2003.
[61] H.-S. Kim, Y. S. Chae, B. H. Park, J.-S. Yoon, M. Kang, and H.-J. Jin, "Thermal and electrical conductivity of poly(l-lactide)/multiwalled carbon nanotube nanocomposites," *Current Applied Physics*, vol. 8, no. 6, pp. 803–806, Oct. 2008.

[62] P. Bonnet, D. Sireude, B. Garnier, and O. Chauvet, “Thermal properties and percolation in carbon nanotube-polymer composites,” *Appl. Phys. Lett.*, vol. 91, no. 20, p. 201910, Nov. 2007.
[63] P. D. Spanos and A. Kontsos, “A multiscale Monte Carlo finite element method for determining mechanical properties of polymer nanocomposites,” *Probabilistic Engineering Mechanics*, vol. 23, no. 4, pp. 456–470, Oct. 2008.
[64] G. I. Evangelatos and P. D. Spanos, “A Collocation Approach for Spatial Discretization of Stochastic Peridynamic Modeling of Fracture,” *Journal of Mechanics of Materials and Structures*, vol. 6, pp. 1172–1195, 2011.
[65] P. Spanos, P. Elsbernd, B. Ward, and T. Koenck, “Estimation of the physical properties of nanocomposites by finite-element discretization and Monte Carlo simulation,” *Philosophical Transactions of the Royal Society of London A: Mathematical, Physical and Engineering Sciences*, vol. 371, no. 1993, p. 20120494, Jun. 2013.
[66] J. Decklever and P. Spanos, “Nanocomposite material properties estimation and fracture analysis via peridynamics and Monte Carlo simulation,” *Probabilistic Engineering Mechanics*, 2015.
[67] A. Tamer, “Probabilistic Determination of Thermal Conductivity and Cyclic Behavior of Nanocomposites via Multi-Phase Homogenization,” Thesis, Rice University, 2013.
[68] P. Spanos, J. Decklever, and A. Tamer, “Probabilistic Determination of Thermal Conductivity of Nanocomposites via Multi-Phase Homogenization,” in *7th International Conference*, Santorini Greece, 2014.
[69] M. Esteva and P. Spanos, “Effective elastic properties of nanotube reinforced composites with slightly weakened interfaces,” *Journal of Mechanics of Materials and Structures*, vol. 4, no. 5, pp. 887–900, Sep. 2009.
[70] K. Toprak and Y. Bayazitoglu, “Numerical modeling of a CNT–Cu coaxial nanowire in a vacuum to determine the thermal conductivity,” *International Journal of Heat and Mass Transfer*, vol. 61, pp. 172–175, Jun. 2013.
[71] R. A. Shelly, K. Toprak, and Y. Bayazitoglu, “Nose–Hoover thermostat length effect on thermal conductivity of single wall carbon nanotubes,” *International Journal of Heat and Mass Transfer*, vol. 53, no. 25–26, pp. 5884–5887, Dec. 2010.
[72] K. Toprak and Y. Bayazitoglu, “Interfacial thermal resistance of Cu–SWCNT nanowire in water,” *International Journal of Heat and Mass Transfer*, vol. 79, pp. 584–588, Dec. 2014.
[73] M. Esteva, “Hybrid Finite Elements Nanocomposite Characterization by Stochastic Microstructuring,” Rice University, 2008.
[74] P. D. Spanos and M. Esteva, “Effect of Stochastic Nanotube Waviness on the Elastic and Thermal Properties of Nanocomposites by Fiber Embedment in Finite Elements,” *Journal of Computational and Theoretical Nanoscience*, vol. 6, no. 10, pp. 2317–2333, Oct. 2009.
[75] P. Elsbernd, “A non-linear finite element model for the determination of elastic and thermal properties of nanocomposites,” Thesis, Rice University, 2009.
[76] T. Koenck, “Piezoelectric Nanocomposites Properties Estimation by Finite-Element Discretization and Monte Carlo Simulation,” Thesis, Rice University, 2013.

[77] B. Ward, “A Numerical Resistor Network Model for the Determination of Electrical Properties of Nanocomposites,” Thesis, Rice University, 2011.
[78] S. Wang, Z. Liang, B. Wang, and C. Zhang, “Statistical characterization of single-wall carbon nanotube length distribution,” *Nanotechnology*, vol. 17, no. 3, p. 634, 2006.
[79] K. J. Ziegler *et al.*, “Statistically accurate length measurements of single-walled carbon nanotubes,” *J Nanosci Nanotechnol*, vol. 7, no. 8, pp. 2917–2921, Aug. 2007.
[80] A. Cao and J. Qu, “Size dependent thermal conductivity of single-walled carbon nanotubes,” *Journal of Applied Physics*, vol. 112, no. 1, p. 013503, Jul. 2012.
[81] M. R. Falvo *et al.*, “Nanometre-scale rolling and sliding of carbon nanotubes,” *Nature*, vol. 397, no. 6716, pp. 236–238, Jan. 1999.
[82] F. H. Gojny, M. H. G. Wichmann, B. Fiedler, and K. Schulte, “Influence of different carbon nanotubes on the mechanical properties of epoxy matrix composites – A comparative study,” *Composites Science and Technology*, vol. 65, no. 15–16, pp. 2300–2313, Dec. 2005.
[83] G.-J. Hu and B.-Y. Cao, “Thermal resistance between crossed carbon nanotubes: Molecular dynamics simulations and analytical modeling,” *Journal of Applied Physics*, vol. 114, no. 22, p. 224308, Dec. 2013.
[84] M. Büttiker, Y. Imry, R. Landauer, and S. Pinhas, “Generalized many-channel conductance formula with application to small rings,” *Phys. Rev. B*, vol. 31, no. 10, pp. 6207–6215, May 1985.
[85] S. U. S. Choi, Z. G. Zhang, W. Yu, F. E. Lockwood, and E. A. Grulke, “Anomalous thermal conductivity enhancement in nanotube suspensions,” *Applied Physics Letters*, vol. 79, no. 14, pp. 2252–2254, Oct. 2001.
[86] J. E. Akin, “Chapter 3 - Element interpolation and local coordinates,” in *Finite Element Analysis with Error Estimators*, Oxford: Butterworth-Heinemann, 2005, pp. 92–115.
[87] N. Hu, Y. Karube, C. Yan, Z. Masuda, and H. Fukunaga, “Tunneling effect in a polymer/carbon nanotube nanocomposite strain sensor,” *Acta Materialia*, vol. 56, no. 13, pp. 2929–2936, Aug. 2008.
[88] Y. Ono, T. Aoki, and T. Ogasawara, “Mechanical and electrical properties of carbon-nanotube composites,” presented at the 48th Conf. Structures Strength, Japan, 2006, pp. 141–143.
[89] “Research Report.” Nano Carbon Technologies Co., Ltd., 2004.
[90] B. Krause, T. Villmow, R. Boldt, M. Mende, G. Petzold, and P. Pötschke, “Influence of dry grinding in a ball mill on the length of multiwalled carbon nanotubes and their dispersion and percolation behaviour in melt mixed polycarbonate composites,” *Composites Science and Technology*, vol. 71, no. 8, pp. 1145–1153, May 2011.
[91] Z. Han and A. Fina, “Thermal conductivity of carbon nanotubes and their polymer nanocomposites: A review,” *Progress in Polymer Science*, vol. 36, no. 7, pp. 914–944, Jul. 2011.

[92] J. A. King, D. Lopez Gaxiola, B. A. Johnson, and J. M. Keith, “Thermal Conductivity of Carbon-filled Polypropylene-based Resins,” *Journal of Composite Materials*, vol. 44, no. 7, pp. 839–855, Apr. 2010.
[93] C. Guthy, F. Du, S. Brand, K. I. Winey, and J. E. Fischer, “Thermal Conductivity of Single-Walled Carbon Nanotube/PMMA Nanocomposites,” *J. Heat Transfer*, vol. 129, no. 8, pp. 1096–1099, Mar. 2007.